Fall 2016

Thermo-Mechanical System Identification of a Shape Memory Alloy Actuated Mechanism

Cody Alexander Wright
Old Dominion University

THERMO-MECHANICAL SYSTEM IDENTIFICATION OF A SHAPE MEMORY ALLOY ACTUATED MECHANISM

by

Cody Alexander Wright
B.S. August 2011, Old Dominion University

A Thesis Submitted to the Faculty of
Old Dominion University in Partial Fulfillment of the
Requirements for the Degree of

MASTER OF SCIENCE

MECHANICAL ENGINEERING

OLD DOMINION UNIVERSITY
December 2016

Approved by:

Onur Bilgen (Director)

Sebastian Y. Bawab (Member)

Sushil Chaturvedi (Member)

ABSTRACT

THERMO-MECHANICAL SYSTEM IDENTIFICATION OF A SHAPE MEMORY ALLOY ACTUATED MECHANISM

Cody Alexander Wright
Old Dominion University, 2016
Director: Dr. Onur Bilgen

Shape memory alloy (SMA) actuators paired in an antagonistic arrangement can be used to produce mechanisms that replicate human biomechanics. To investigate this proposal, the biomechanical articulation of the elbow by means of the biceps brachii muscle is compared with that of a SMA actuated arm. This is accomplished by parametric analysis of a crank-slider kinematic mechanism actuated, first, with an experimentally characterized SMA wire and then an idealized musculotendon actuator based on actuation properties of muscles published in the literature. Next, equations of motion for the system dynamics of the SMA actuated mechanism are derived and phase portrait analysis is conducted varying system parameters around different operating points. The eigenvalues of the differential equation are examined around equilibrium points and a stiffness ratio metric is proposed to characterize dynamic stability based on system parameters. Next, a heat transfer model is proposed and energy analysis is conducted on each stage of phase transformation for the SMA wire. The unknown parameters in the heat transfer model are theoretically derived and an experimental system identification is conducted. A proof of concept antagonistic SMA actuated mechanism is designed and kinematic analysis is conducted on an experimental prototype.

I dedicate this work to my mother Vicki Russo and my grandmother Anne Wright.

ACKNOWLEDGMENTS

First, I would like to thank Dr. Onur Bilgen for his support and expertise; without his guidance and insight no parts of this thesis would be possible. Also, I would like to thank Dr. Bilgen for the introduction into the world of smart materials. It has provided me innumerable hours of fascination and discovery.

Special thanks to my mother, Vicki Russo, who provides an unending source of inspiration and equally matched conviction in my ability to do great things.

Sincere thanks to the staff of the College of Engineering machine shop for their contribution and assistance with modifications to the wire test bed and fabrication of the kinematic test bed. Thanks to Michael Polanco in the Mechanical Engineering Design Lab for always accurate and expedited 3D printing of each iteration of the antagonistic proof of concept.

Thanks to the Department of Mechanical and Aerospace Engineering at Old Dominion University, especially to Dr. Sebastian Y. Bawab, for financial and logistical support.

This work was conducted in the Smart Systems Laboratory at Old Dominion University.

TABLE OF CONTENTS

Chapter Page

LIST OF TABLES

LIST OF FIGURES

Figure Page

Figure Page

Figure Page

Figure Page

CHAPTER 1

INTRODUCTION AND LITERATURE REVIEW

1.1. Introduction

An effective prosthetic device limits weight, eases ergonomic discomfort, while excelling at biomechanical replication. Shape memory alloy (SMA) wires show promise as a substitution for conventional actuators in prosthetic devices by synthesizing each of the aforementioned characteristics. Similar to muscles, SMA wires have a coupled mechanical interaction. In muscles, an electrical impulse from the nervous system stimulates a bio-chemical transport reaction of sodium, potassium, and chloride ions causing muscle contraction. In contrast, an electric current is driven through SMA wire, inducing Joule heating throughout, causing length contraction in the wire by up to nine-percent of total length. Using these similar properties, it is proposed, that using SMA wire as a synthetic muscle, it is possible to design a prosthetic device with equivalent biomechanical properties as the human arm. In order to draw these parallels several systems must be investigated comprehensively. These systems include the biomechanical properties of the human arm, the dynamic properties of a mechanically equivalent system and the heat transfer of Joule heating within the SMA wire. This thesis examines the methods of system identification necessary to achieve such system.

1.2. Literature Review

1.2.1. History of Shape Memory Alloys

Shape memory alloy is a thermo-mechanically coupled smart material. A smart material is a material classification such that material properties can be controllable by an external stimulus. In the case of shape memory alloy, a temperature change effects material properties such as Young's modulus and coefficient of thermal expansion [1]. This is due to crystalline structure reorientation on heating. The first documented observation of a shape memory alloy and the shape memory effect was in 1932 by Arne Olander [2]. It was observed that a gold-cadmium (Au-Cd) alloy could be plastically deformed and on re-heat the plastic deformation could be recovered. There was little known about the mechanism behind this effect until 1951 when Chang and Read [3] published a description of the rubber-like martensitic reorientation of the atomic lattice in gold-cadmium. These two investigations were major landmarks in the understanding of shape memory alloys as a smart material but due to material cost it was not accepted as a practical material for use in engineering applications. This changed in 1962 when Buehler et al. [4] at the Naval Ordnance Laboratory showed the shape memory effect was significant enough in a nickel-titanium alloy. This allowed shape memory alloys to be commercially feasible due to cheaper production cost, ease of work, and improved mechanical properties [5]. The nickel-titanium alloy became commonly referred to as the portmanteau Nitinol, for ***NI***ckel ***TI***tanium ***N***aval ***O***rdnance ***L***aboratory.

1.2.2. The Shape Memory Effect

The complete cycle of the thermo-mechanical transformation of shape memory alloys are illustrated in Figure 1.1. Let's assume that the bulk material begins arbitrarily in the detwinned martensite phase (1). This is a phase that is characterized by low modulus of elasticity, yield strength and strain rate. In this orientation the alloy is at its most lengthened state. Upon heating of the material the alloy goes through a phase transformation beginning at an activation temperature, referred to as the austenite start temperature (T_{A_s}). During this transformation the alloy, ideally, transforms continuously throughout the structure from zero to

one hundred percent austenite (2) causing an overall length contraction of up to 10%. The completion of the phase transformation finishes at the austenite final temperature $\left(T_{A_f}\right)$. Also associated with the austenite phase is an increase in the Young's modulus. If the material is cooled, the reverse transformation process occurs. The transformation from austenite to martensite begins at the martensite start temperature $\left(T_{M_s}\right)$ and ends at the martensite final temperature $\left(T_{M_f}\right)$. Unlike the martensite to austenite transformation, the reverse transformation is characterized by very little change in the overall length. At return to its original temperature, the material is in the martensite twinned state (3). The martensite twinned phase can be returned to the detwinned martensite phase (4) with an application of stress; which stresses the material.

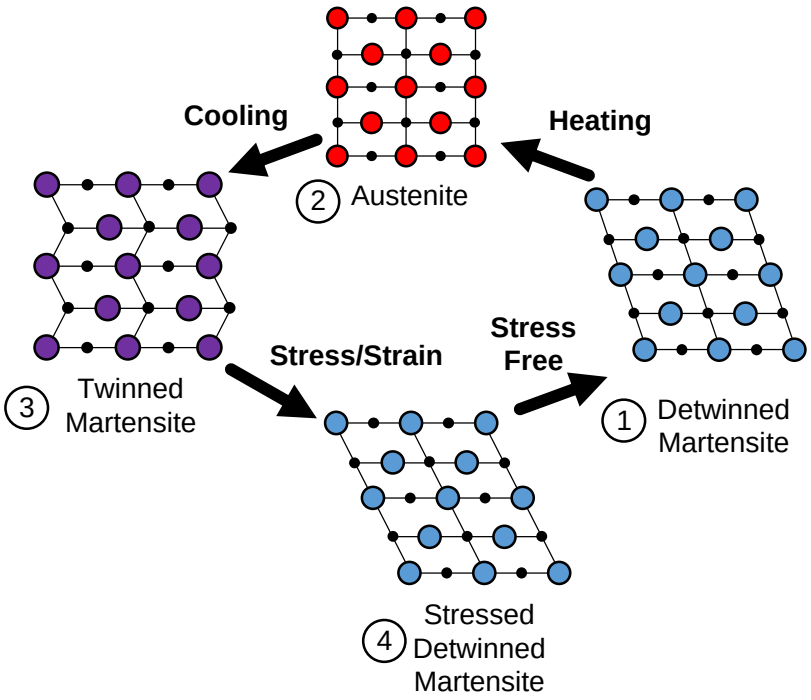

Figure 1.1. Phase transformation cycle for shape memory alloy.

Not only are there material properties at the temperature extrema for martensite and austenite, there is a continuous set of material properties in between at different fractions of the martensite-austenite composition. Compiling the stress-strain characteristics during phase

transformation and plotting across the range of temperatures, the stress-strain-temperature curve is produced as shown in Figure 1.2.

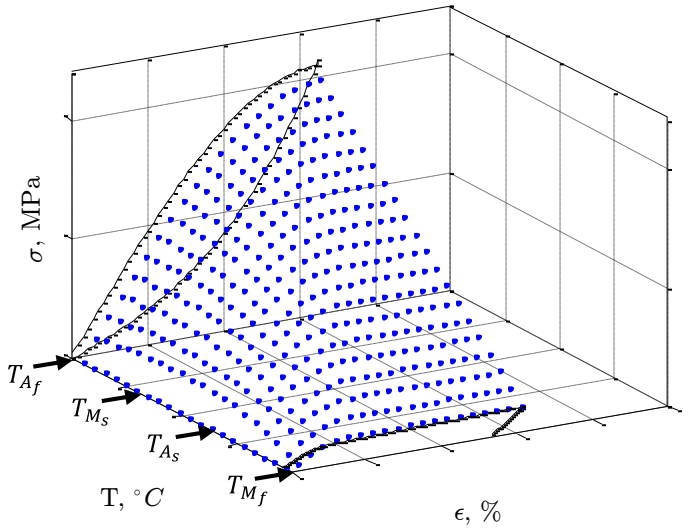

Figure 1.2. Stress Strain Temperature relationship of an SMA.

There are two significant effects that can be deduced from the stress-strain-temperature diagram. The first being the super-elastic effect and the second being the shape memory effect. The super-elastic effect occurs entirely at the austenite final temperature (T_{A_f}). In this super-heated austenite phase, when stress is applied, the material follows a common stress-strain curve up to a plateau region. In this region the material can experience up to 9% strain with very small additional stress. When stress is removed, the material returns to its original length. The super-elastic effect will not be of interest in this thesis. The primary focus of this thesis is the shape memory effect and its application to actuation and biomechanics.

The shape memory effect is a phenomena that begins at the martensite detwinned state at martensite final temperature. On temperature increase the material undergoes contraction strain due to the crystallographic reorientation. This continues until austenite final temperature. At this temperature, the crystallographic structure is completely in the austenite phase and no more contraction can occur. In practice, if a load is applied to one end of a shape memory alloy

wire, it is possible to move the load during the martensite to austenite phase transition; thus, performing useful mechanical work. This ability to perform work, in a so-called solid-state manner, is the focus of this thesis. Once actuation is complete, the wire must be returned to the martensite detwinned state before actuation can occur again. This is done by cooling to martensite final temperature and applying external stress to the wire, returning the material to the detwinned state.

In recent literature there has been a large increase in the number and breadth of publications on the topic of SMA actuation. For aerospace applications, Kudva et al. [6] showed SMA actuators could be used to morph aircraft wing to improve aerodynamic performance. In the medical field, an SMA manipulated endoscope was designed for inspection and intervention by Reynaerts and Brussel [7]. Some of the most promising research comes from microelectromechanical systems (MEMs) where diverse applications like a thin film micro-pump was developed by Ho et al. [8].

1.2.3. Shape Memory Alloys Used in Biomechanical Actuation

A review by Bidiss and Chau [9] examined the most critical design factors for upper extremity prosthetics and reasons for prosthetic abandonment over a 25 year period. In 2007, the reasons for abandonment of prosthesis were due to:

1. Prosthesis discomfort,
2. Lack of functionality gained,
3. Weight of prosthesis,
4. Durability,
5. Unattractive appearance.

A shape memory alloy as an actuator may help solve some of the abandonment issues by providing a more light-weight and powerful alternative to conventional actuation techniques. With the correct design parameters, a prosthetic device powered by SMAs may alleviate weight and discomfort of the prosthesis while increasing functionality.

The high work per volume, high strain rates, and large forces make SMAs a good candidate for an artificial muscle. SMA actuation for biomechanical applications have been a

subject of research as early as 1986, when Kuribayashi [10] proposed a nickel-titanium actuator for a joint mechanism to replicate motion of a robotic hand, artificial arm, or artificial leg. In 1989, Bergamasco et al. [11] investigated the use of SMA actuators in a push-pull mode to drive a dexterous artificial hand. In 1995, Gharaybeh and Burdea [12] used SMA actuators as force-feedback control for use in a multi-fingered robot. More recently in, 2007, Price et al. [13] designed and controlled SMA actuated fingers concluding that SMAs are a feasible actuation technology for prosthetics. Shortly thereafter, in 2008, Bundhoo et al. [14] showed a biomimetic hand for flexion/extension of finger muscles using SMA wires.

A large percentage of SMA prosthetic applications have been centered around the manipulation of the hand specifically. There is a gap in academic research in the study of mechanics of prosthetic devices. SMAs have been identified as a viable substitute for muscles; however, design parameters for SMA-based prosthetic devices have not been fully investigated to mimic the musculoskeletal system [14-16].

1.3. Objectives

The overall objective of this research is to study the fundamental systems required to develop a so called solid-state prosthetic arm actuated by shape memory alloy wire. The first step, and the objective of this thesis, is to theoretically and experimentally determine the kinematics and energy characteristics of a crank-slider mechanism actuated by an experimentally characterized SMA wire. This is done by the following objectives:

1. Develop performance metrics for an SMA actuated kinematic mechanism and compare the SMA actuated performance metrics with that of a mechanism actuated by a simplified muscle model.
2. Fundamental understanding of external force effects on said SMA actuated mechanism.
3. Understanding of the energy contributions of heat transfer in the SMA wire actuator and the method for system identification.
4. Demonstration of mechanically equivalent SMA actuated human arm system.

Through these objectives this work will grant the ability to develop a thermo-mechanically coupled model. In which further analysis can be focused to minimize actuation energy for an SMA system and to develop groundwork for so called solid-state prosthetic arm.

1.4. Outline of the Thesis

The thesis is organized as follows. Chapter 2 investigates the kinematics of a crank-slider mechanism proposed to replicate the flexion motion of the biceps-brachii actuation of the forearm. A shape memory alloy wire is characterized and replaced as the actuator for said mechanism. A parametric analysis is conducted for performance metrics of rocking angle, work, and torque on the crank-slider mechanism. These results are compared with a mechanism actuated by a human muscle and design parameters to replicate human arm movement is recommended for the SMA wire actuated mechanism.

Chapter 3 begins with the energy and force-balance derivation for the equations of motion of the crank-slider mechanism. Following the derivation, phase portrait analysis is introduced and a linearized system of ordinary differential equations are proposed for eigenvalue analysis. Phase portrait analysis is performed on an undamped system with varying system parameters. A nondimensional stiffness ratio is proposed for the system and is compared to eigenvalue response at different operating points. Following the undamped response, a damped response is examined by analyzing the energy around equilibrium positions.

Chapter 4 investigates the energy generation and heat transfer in an unstressed SMA wire. A transient heat transfer model is proposed and analyzed; examining the energy contribution of the model terms during each stage of phase transformation in the shape memory effect. The unknown parameters in the heat transfer equation are theoretically derived based on the heat transfer model. Experiments are conducted on a wire test bed to determine the unknown coefficients.

Chapter 5 experimentally demonstrates the antagonistic actuation of an SMA wire pair. Actuation angle of the antagonistic mechanism is measured as a function of pre-stress in the wire.

Chapter 6 is a summary of the conclusions derived in this thesis. Publications stemming from this research are also listed.

CHAPTER 2

STATIC & STEADY-STATE STRUCTURAL BEHAVIOR

2.1. Introduction

It is the intent of this chapter to investigate the steady-state structural behavior of a shape memory alloy actuated kinematic mechanism using parametric analysis. The results are compared with a human musculoskeletal actuated mechanism to define design parameters for biomechanical replication of a shape memory alloy actuated arm.

In this chapter a brief overview of kinematics will be presented. Following the overview, a mechanically equivalent system is proposed for the actuation of biceps brachii–triceps muscle pair of the human arm. Performance metrics for steady-state structural behavior are then presented with calculations. Next, the actuator characteristic curve for an SMA wire is determined based on experimentally obtained stress-strain curves at martensite phase and austenite phase. A parametric analysis is performed over a gamut of geometries for the kinematic mechanism first assuming a linearized actuator curve then a non-linear actuator curve. This is followed by a discussion of the results. Next, a kinematic test bed is proposed for measuring kinematic motion using machine vision software. This is validated using theoretical calculations of a rigid body mechanism. To conclude the chapter, a brief overview of bio-mechanic link-lengths and actuator curves are introduced. Parametric analysis is used on these anatomical values and based on the results an SMA actuated mechanism design is recommended.

2.2. Kinematics Model

The crank-slider linkage is the quintessential mechanical mechanism. It can describe mechanisms as common as the internal combustion engine or a water pump-jack to something as remarkable as - and in the case of this thesis - the musculoskeletal motion of the human arm.

The primary motivation for this research is to understand the influences of a shape memory alloy actuated arm at a fundamental level and using this fundamental research, apply it to the design of a prosthetic arm.

To represent the actuation of the biceps brachii and triceps muscles, an agonistic-antagonistic pair SMA wire mechanism is assumed. The idealized kinematic mechanism is shown in Figure 2.1. Using a mechanical equivalent model for a bio-mechanical system will allow kinematic analysis to be performed easily for a variety of parameters. The design is modeled after the human arm in the subsequent ways. The elbow joint is modeled as a simple revolute joint (A) while the humerus and radius are modeled as rigid bodies, L_1 and L_2 respectively. The contraction of the biceps muscle is modeled as a slider (C). For return actuation, which is accomplished by the triceps muscle, a duplicate mechanism is assumed to work in the opposing direction. Together, the proposed model for the human arm can be described as a double crank-slider.

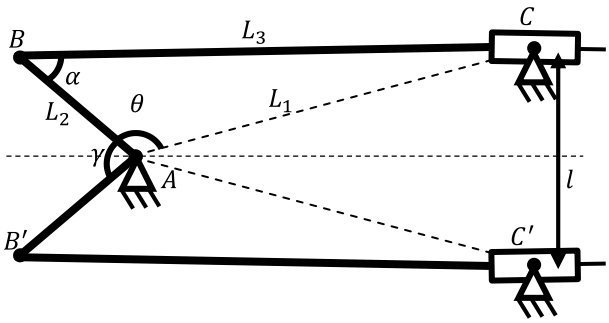

Figure 2.1. Full kinematic mechanism.

Before two-way actuation is studied the model is simplified further into one-way actuation representing flexion of the elbow solely by the biceps muscle. By reducing the length between the two slider joints, C and C', to zero and removing linkages AB' and $B'C'$, the mechanism is reduced to a single crank-slider. This reduced mechanically equivalent model is shown in Figure 2.2.

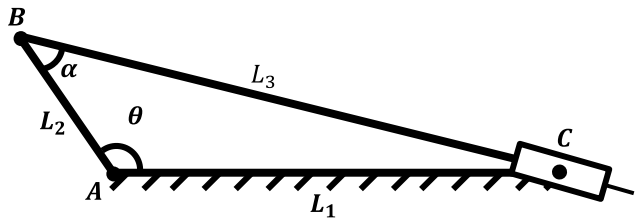

Figure 2.2. Reduced kinematic mechanism.

All further analysis in this chapter will be conducted on the reduced crank-slider mechanism. This mechanism is, as described previously, simply the actuation of the elbow flexion by way of the biceps brachii muscle. Figure 5 displays this mechanism linkages superimposed on an illustration of the human arm.

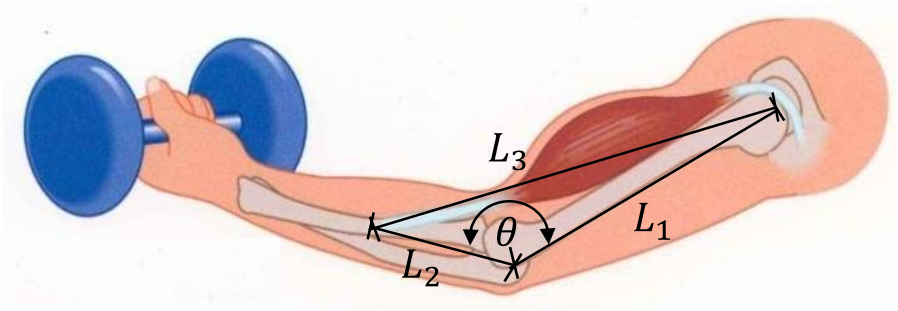

Figure 2.3. Illustration of the human arm mechanism.

2.2.1. Kinematic Equations

A crank-slider mechanism is a single degree of freedom system. To determine the position of every point on the mechanism, only the internal angle θ is required. Of interest, in the kinematic analysis, is the position of an applied load at point B. Performing position analysis on B with an inertial reference attached to link 1, the loop equation is:

$$\vec{r}_B = \vec{r}_A + \vec{r}_{B/A}. \tag{2.1}$$

Taking the derivative with respect to time produces the velocity equations:

$$\vec{V} = \vec{\omega}_2 \times \vec{r}_{B/A} \tag{2.2}$$

$$\vec{V}_B = \vec{V}_{C3/C4} + \vec{\omega}_3 \times \vec{r}_{B/C3} \tag{2.3}$$

Taking the derivative a second time, the acceleration equations are obtained:

$$\vec{A}_B = \vec{\alpha}_2 \times \vec{r}_{B/A} + \vec{\omega}_2 \times (\vec{\omega}_2 \times \vec{r}_{B/A}) \tag{2.4}$$

$$\vec{A}_B = \vec{A}_{C3/C4} + 2(\vec{\omega}_3 \times \vec{V}_{B/C3}) + \vec{\alpha}_3 \times \vec{r}_{B/C3} + \vec{\omega}_3 \times (\vec{\omega}_3 \times \vec{r}_{B/C3}) \tag{2.5}$$

2.2.2. Parametric Analysis

From a purely kinematics perspective, the rocking angle is the most interesting parametric response. To simulate contraction of the SMA wire the slider length (L_3) is initially assumed to reduce by 5%. This contraction level is a realistic value for the SMA wire considered in this thesis. A preliminary parametric analysis is conducted, varying the length of the base link from 0.5 to 40 times that of L_2, and the starting angle (θ) from 45 to 175 degrees.

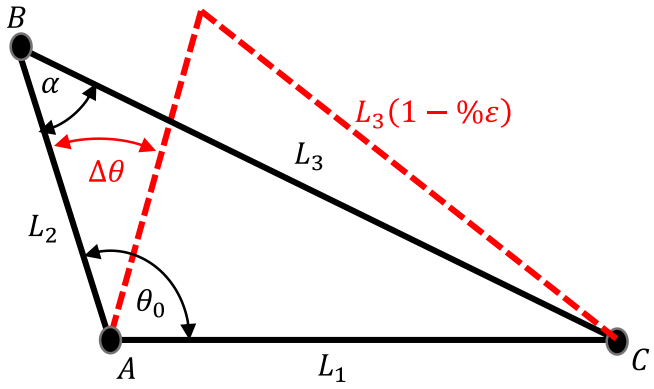

Figure 2.4. Rocking angle illustration.

The results of the parametric kinematic study are compiled and displayed in a contour plot shown in Figure 2.5. This kinematic study uses a normalized rocker length of one unit, increasing the frame length from fractions of the unit length to magnitudes higher. The results of this study creates a contour plot with clear boundary conditions that require a brief explanation.

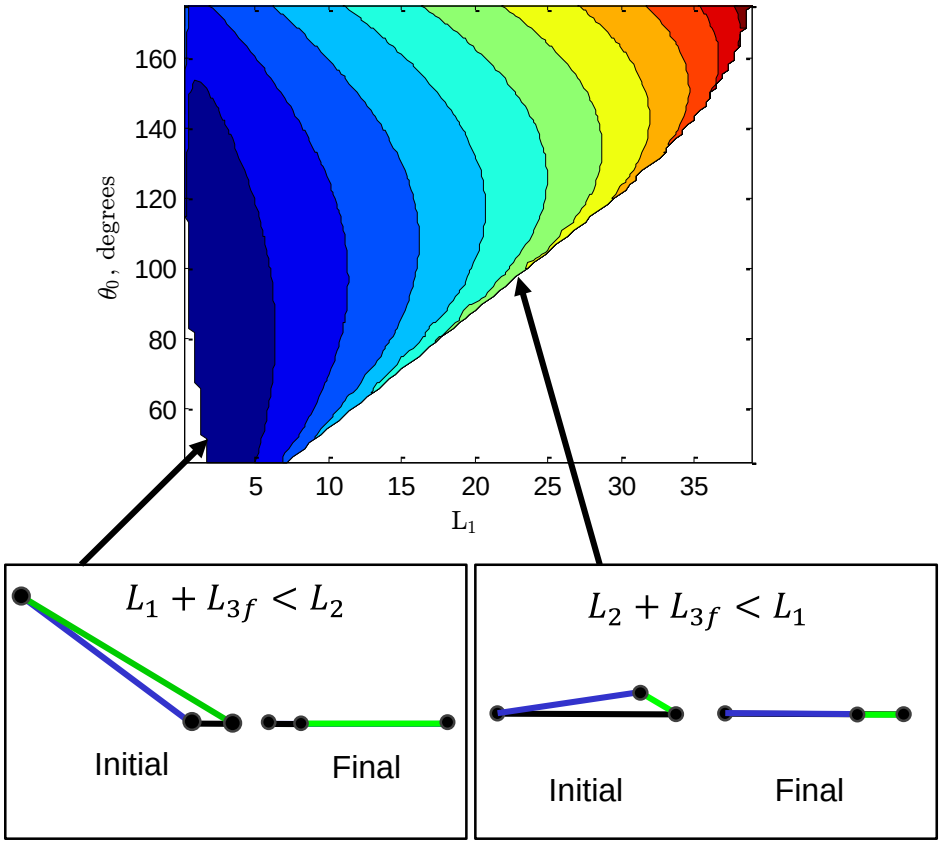

Figure 2.5. Contour plot diagram showing the difference between two boundaries for two kinematic incompatibilities.

The contour plot result displays the metric of interest as a function of starting angle, on the y-axis, and frame length, on the x-axis. The starting angle (θ_0), is the angle at which actuation begins and is the resulting angle when the slider is free of displacement. The frame length is simply the frame length multiplied by the rocker unit length of one. At each data point on the contour plot the response is the combination of initial conditions given a 5% contraction of the slider.

There are evident boundaries on the contour plot. These boundaries are initial conditions that produce kinematic mechanisms that cannot complete actuation due to two different kinematic incompatibilities. The first incompatibility is the bottom left boundary, where the length of the frame summed with the final length of the actuator produces a mechanism that is shorter than the overall length of the rocker. The second incompatibility is a

mechanism where the length of the rocker summed with the final length of the actuator is shorter than the length of the frame. These are in fact the same incompatibility, producing a symmetric mechanism, where the frame and the rocker are mirrors of one another.

Displayed in Figure 2.6 are the results of the parametric analysis of rocking angle with respect to varying starting angle and frame length. The features worth noting are the boundary conditions and the linear gradient from low rocking angles to high rocking angles following frame length.

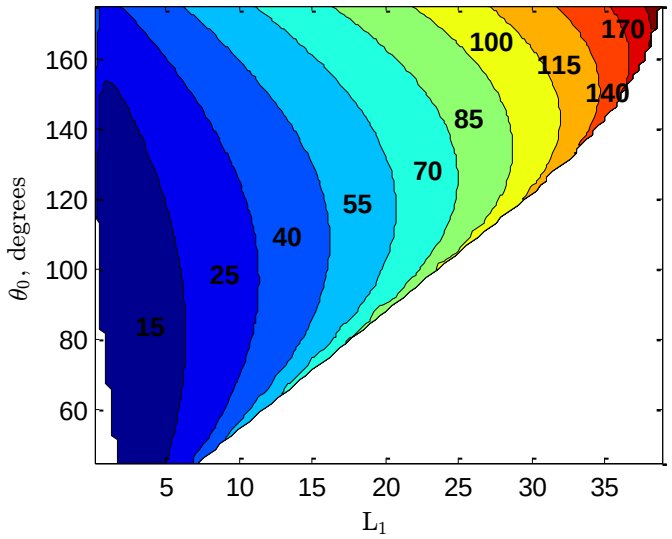

Figure 2.6. Maximum rocking angle (degrees) of a crank-slider mechanism with a 5% reduction in the slider link as a function of L_1 and θ_0.

The maximum rocking angle occurs at high frame lengths and high starting angles. This area corresponds to the top right of Figure 2.6 and are asymptotically close to 180 degrees. Conversely, the lowest rocking angles are in the bottom left region and are produced by low frame lengths and low initial angles. These mechanisms produce infinitesimally small rocking angles.

2.3. SMA Wire Stress-Strain Curves

2.3.1. Force / Torque Analysis

To understand force effects on the crank-slider mechanism, a linear spring is used to replace the rigid body of the slider (L_3). The spring is assumed to have a zero-stress condition at the starting angle (θ_0). A 5% spring displacement is assumed and the actuator characteristic curve for a linear spring is used to determine the energy and torque applied at the tip of the rocker.

Torque is calculated as the product of the length of the moment arm (L_{ma}) and the projection of the force in the same direction of the stroke ($F_s \sin\alpha$). Looking at Figure 2.7. , the moment arm is the imaginary line running from point A to L_3 where L_{ma} and L_3 are perpendicular.

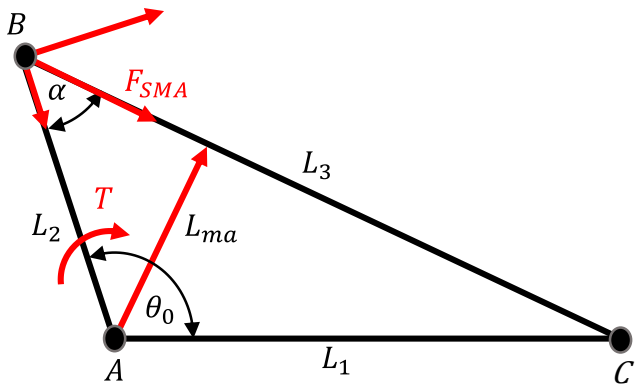

Figure 2.7. Kinematic mechanism showing torque effect due to moment arm and force of SMA wire.

An actuator characteristic curve is a theoretical curve that displays the stroke of an actuator as a function of the load applied to the actuator. The y-axis intercept of the actuator characteristic curve is known as the blocking force (F_b) – where the actuator produces no displacement when the blocking force is applied. The x-axis intercept is the free strain condition (u_i), providing how much the actuator can move when no load is applied. For a linear

actuator characteristic curve, all points between the blocking force and free strain condition can be described by the equation $F_a = k_a(u - u_i)$, where u is stroke of the actuator and F_a is the force at that stroke. The linear actuator characteristic curve for a linear spring load is shown in Figure 2.8.

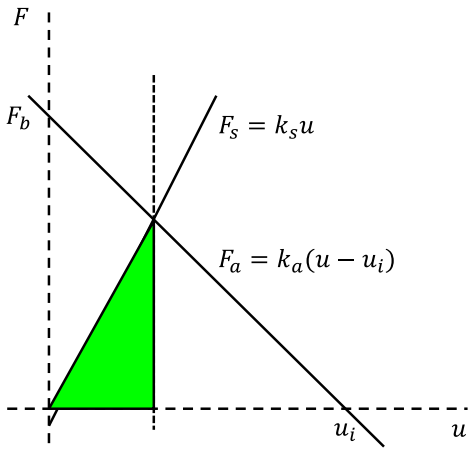

Figure 2.8. The characteristic and operational curves for a linear actuator.

To determine useful mechanical energy the opposing force is assumed to be a linear spring. As the actuator contracts, the opposing spring extends. The area under the curve is the useful mechanical work for which the actuator performed. This is illustrated by the green triangle in Figure 2.8. Maximum useful mechanical work occurs for a linear system when the spring constant of the opposing spring matches that of the actuator. This is also known as impedance matching and the work is calculated as $1/2\,Fu$ where F and u are the force and displacement values at the cross-section of the two spring curves.

To understand the kinematic response of an SMA actuated arm, the SMA actuator must be subjected to a simple characterization to understand the capabilities of limitations of the actuator itself. As described in the introduction, there are two absolute material states of a traditional SMA actuator; these are the austenite and the martensite phases. The crystallographic state is characterized by the structural orientation of the material crystalline phase. In a complete martensite state, the entire crystalline structure is oriented in the

martensite phase and can be described by being in 100% martensite with a martensite fraction (ξ) of one. The austenite phase, adversely, is oriented completely in the austenite phase and has a martensite fraction of zero.

These two states influence the engineering properties of the material and are responsible for actuation. These effects must properly be understood before kinetic analysis can be performed. This is characterization is completed by determining, experimentally, the stress-strain curves of the complete martensite and austenite states.

2.3.2. Experimental Test Setup

The SMA wire test bed, Figure 2.9 (a), is used to characterize the stress-strain curves for the shape memory alloy at austenite and martensite phases. The SMA wire is a 250 μm diameter nickel titanium wire manufactured by Dynalloy, Inc. The test is controlled using a National Instruments 9178 cDAQ data acquisition system (DAQ). The DAQ sends a voltage control signal to a KEPCO BOP 36-6D bi-operational amplifier which drives current through the SMA wire. The SMA wire is fixated with micro-drill chucks on the top and bottom frame where isolated electrical contacts are located. Resistive heating increases the temperature of the SMA wire and temperature is sensed using Omega K-type thermocouples. Strain in the wire is measured by a Banner LG10A65NIQ laser displacement sensor. The top frame of the test bed is designed to act as a first class lever. The force is applied on the loading spindle located on the far end of the top frame resulting in normal stress about the length of the wire. This is illustrated by a free body diagram shown in Figure 2.9 (b).

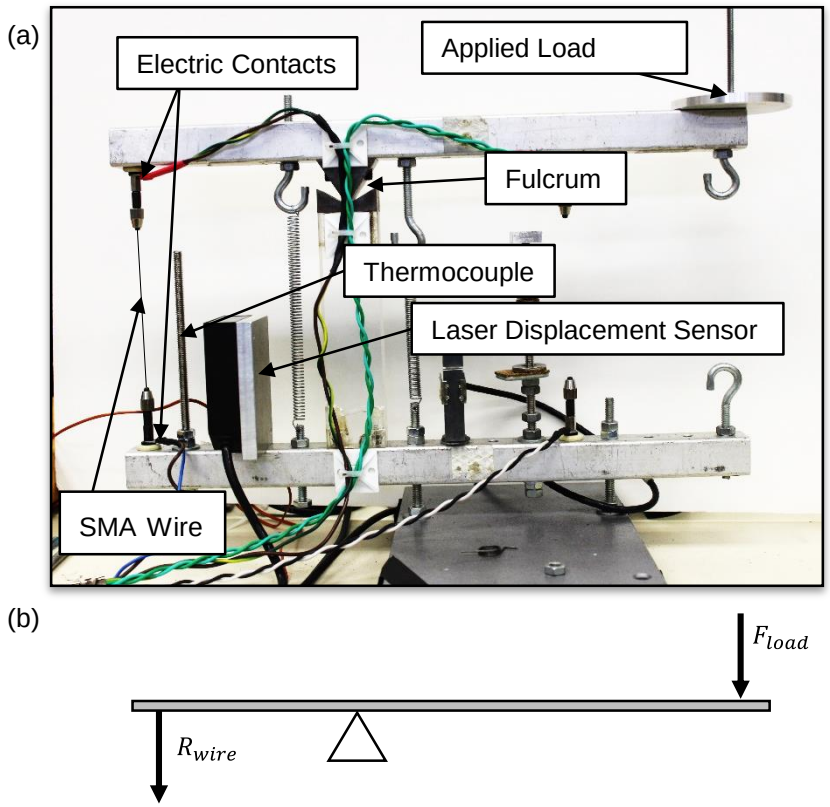

Figure 2.9. (a) Kinematic test bed for measuring stress-strain curves. (b) Free body diagram of top frame acting as a first class lever.

Prior to testing, the top and bottom frames are made parallel to one another and locked into place. At this point, the SMA wire is placed first into the top micro-drill-chuck and fastened. Next, the wire is drawn, with slight tension, and placed in the bottom micro-drill chuck. Once each end of the wire is secured, the locking mechanism is removed and any remaining slack in the wire is eliminated by placing a small experimental weight on the loading spindle. This procedure minimizes the stress and strain initialized in the wire. After the wire has been secured and initialized the thermocouple is placed near the wire. A dab of AOS Heat Sink Compound is placed between the wire and thermocouple to maximize heat transfer surface area. This concludes pre-test preparation.

The martensite phase test procedure begins by driving a 1.0 A current through the wire. This heats the SMA wire above the austenite final temperature to 65 °C. Steady state is achieved

for 15 seconds then all current is removed allowing the SMA wire to transform to the twinned martensite phase. At this state, a semi-automated process is followed.

The semi-automated process consists of adding experimental weights to the loading spindle then recording the total load through the wire and resulting displacement due to strain. The weights are gently placed on the spindle to minimize dynamic forces through the wire. The process is repeated until additional load exhibits a second set of linear behavior. This indicates that detwinned martensite phase has been reached. Next, the semi-automated process is reversed. Load is removed from the spindle with total load and resulting displacement recorded. Once all load has been removed, the wire is reheated and recovered strain is measured.

A nearly identical semi-automated process is followed for measuring the austenite stress-strain curve. The austenite phase test procedure begins by driving a 1.0 A current through the wire; heating the wire to above the austenite final temperature to 65 °C. At this moment, the semi-automated test begins. The experimental weights are added while load and displacement are recorded. Once yield stress has been reached, the process is reversed until all weight is removed.

2.3.3. Experimental Characterization Results

The experimental stress-strain diagrams, seen in Figure 2.10, comply with shape memory alloy stress-strain diagrams found in literature.

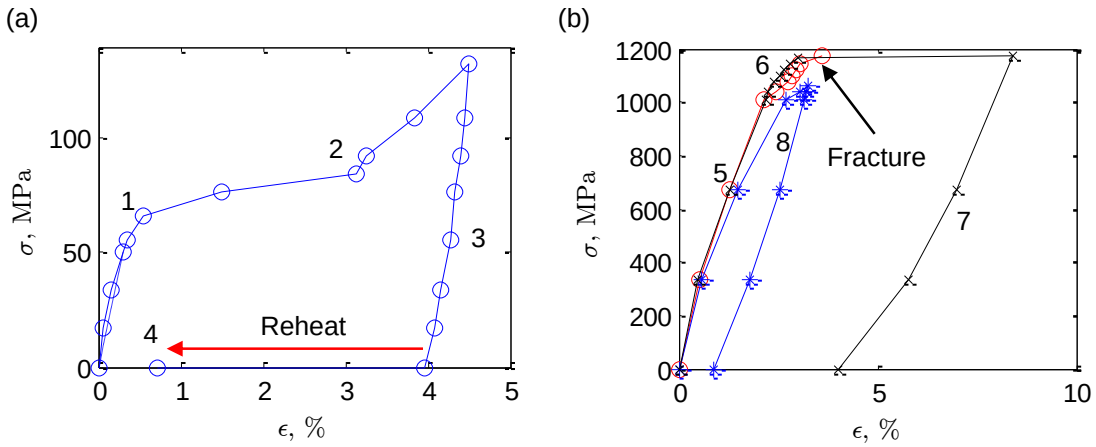

Figure 2.10. (a) Martensite stress-strain diagram from twinned martensite to detwinned martensite phase. (b) Austenite stress-strain diagram for three wire samples.

For the martensite stress-strain curve, the modulus of elasticity is low and labeled as (1). A small incremental increase in stress produces a large strain with the beginning of a second modulus at (2). Relaxation of the wire, shown at (3), is the detwinned martensite modulus of elasticity. On reheat (4), nearly all but 0.75% of total strain is recovered, suggesting from (2) to (3) some plastic deformation may have been experienced.

Figure 2.10 (b) displays three stress-strain curves for the austenite phase. All three curves are important as each shows a different characteristic behavior of the austenite phase. At (5), all three stress-strain curves show a high modulus of elasticity with high yield stress. Yielding occurs abruptly at 1100 MPa with one sample fracturing and the other experiencing super-elastic behavior to (7). The final sample (8), was loaded below the yield stress where a majority of the strain is recovered through unloading.

Using the theoretical paradigms combined with the experimental results, several simplifications can be made to the martensite stress-strain diagram. It can be assumed the second increase in stress-strain at (2) is due to complete martensite detwinning. If unloading occurred at this strain level it would follow a similar unloading curve as (3); leaving the maximum strain experienced during martensite detwinning at a strain level of 3.25% at the stress level of 100 MPa. Without the plastic deformation from (2) to (3), it can be assumed that during the re-heat cycle, 100% of the strain can be recovered. Similar to the idealization of the

martensite phase, the austenite stress-strain curve of (8) can be assumed to recover completely during unloading.

Both the austenite and martensite stress-strain curves were fitted using polynomial functions for each portion of the stress-strain curve. For the martensite phase, loading stages of (1) and (2), and the unloading stage (3) were fitted. The austenite loading and unloading stages were fitted separately. These stress-strain curves are considered the idealized behavior for martensite and austenite phases and are shown in Figure 2.11.

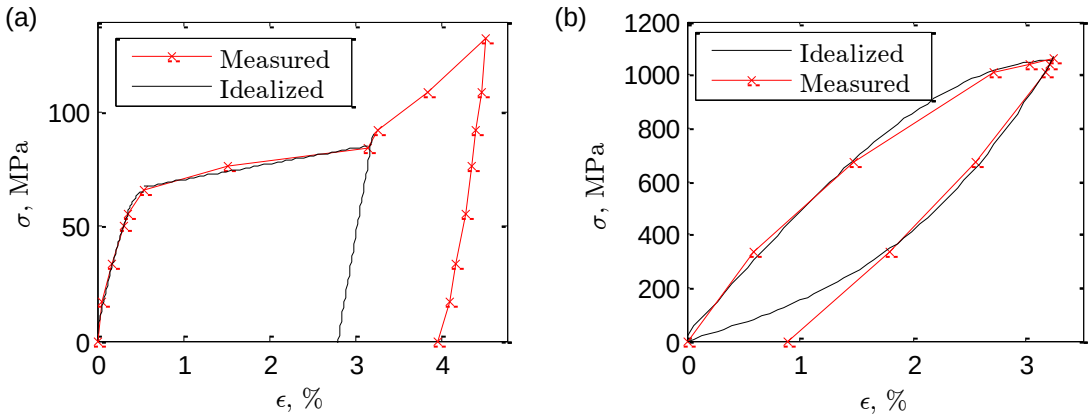

Figure 2.11. Fitted idealized (a) martensite and (b) austenite stress-strain curves.

It is assumed that the maximum loading envelope of the large hysteresis loop could be modeled by a third order polynomial with a temperature offset. The nonlinear region of the hysteresis loop was determined to be

$$\sigma = -15.4\varepsilon^3 + 480\varepsilon + 21 - 12.5(100 - T) \tag{2.6}$$

with a strain offset of

$$\varepsilon = -0.03 * (100 - T). \tag{2.7}$$

A linear slope of 0.1 was added to the stress-strain curve on each isotherm, to complete strains up to 3.25%. The resulting stress-strain-temperature diagram with nonlinear and linear regions labeled is presented in Figure 2.12.

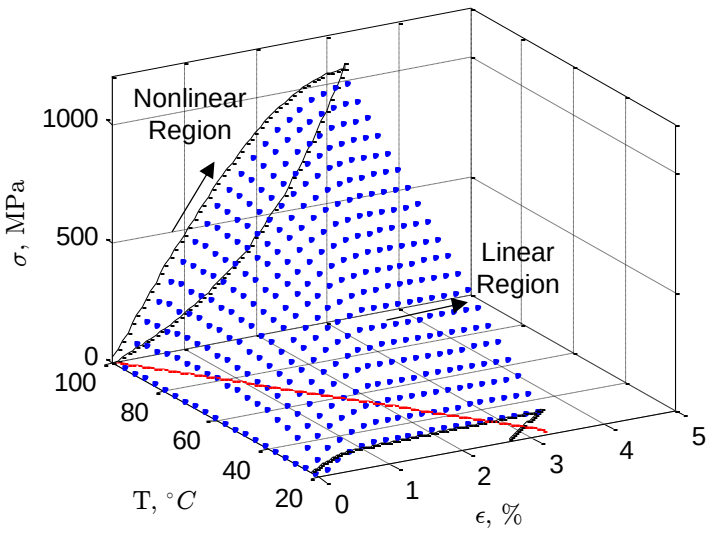

Figure 2.12. Stress-strain-temperature curve showing large hysteresis loop envelope.

The curve proposed represents the experimental data with sufficient accuracy at both the high temperature and low temperature portions of the stress-strain diagram. The observed behavior exhibits expected results when compared to the SMA stress-strain-temperature curves published in the literature [17].

2.3.4. SMA Wire Actuator Curve

The actuation characteristic curve for the nickel-titanium wire is determined by calculating the blocking forces of an SMA actuator (k_{SMA}) against a range of linear springs (k_{eq}). Figure 11 is a representation of the equivalent model used for blocking force analysis. The actuator and spring are in series between two rigid bodies.

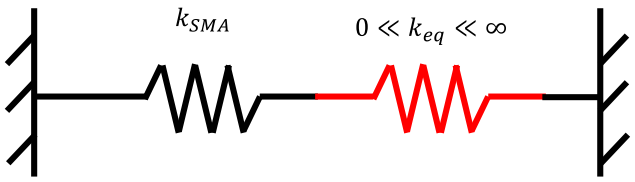

Figure 2.13. Theoretical actuator characteristic curve force balance and constant length assumption.

When k_{eq} approaches zero the SMA actuator can be considered to have zero impedance against it. Solving for the equilibrium condition, the free stroke condition would result. Conversely, if k_{eq} were to approach infinity, the SMA actuator would experience infinite impedance and blocked force would be found. In order to find the points between the free stroke and blocked force conditions the spring-constant of the linear spring is incrementally increased from zero to infinity. Experimental data is used for the non-linear spring rate of the SMA wire. Force balance and constant length equations are used to simultaneously solve for blocking stress and free strain length of the wire.

$$\sigma_{SMA} = k_{eq}(\Delta x_{eq}) \tag{2.8}$$

$$l_{spring}\varepsilon_{SMA} + \Delta x_{eq} = 1 - 2(l_{springs}) \tag{2.9}$$

The solution of the equilibrium equations produce the blocking force and stroke of the SMA actuator. Combining the results produces the actuator characteristic curve for a non-linear SMA wire as shown in Figure 2.14. In this thesis, the difference between a crank-slider mechanism actuated with an SMA wire with non-linear characteristics, and an idealized linear actuator with equivalent properties is of interest; hence the linearized actuator curve is also presented.

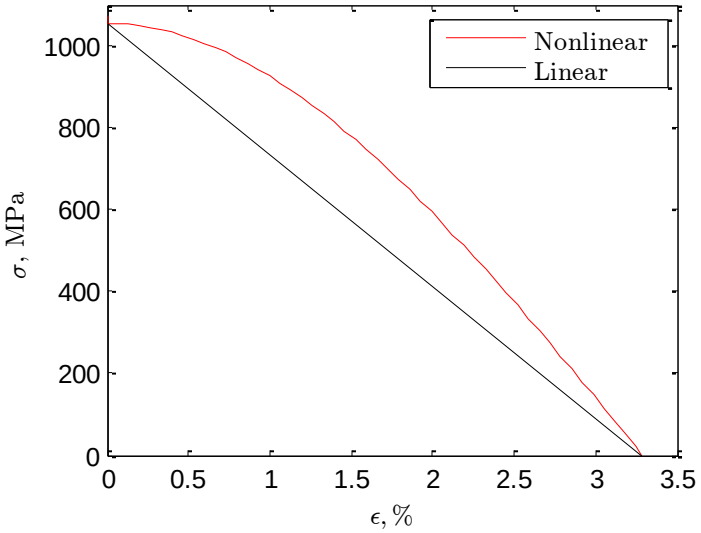

Figure 2.14. Actuator characteristic curve for linear and non-linear actuation spring used as actuator for crank-slider mechanism.

2.3.5. Experimental Verification of SMA Nonlinear Actuator Curve Shape

To verify the actuator curve the SMA wire test bed was used to measure force and displacement simultaneously. As can be seen in Figure 2.15 (a), the SMA wire was attached between two micro drill chucks and balanced to its free length with zero stress and zero strain. Between the load cell and top frame, springs of varying spring constants, see Table 2.1, are attached. A free body diagram of the load during testing is shown in Figure 2.15 (b).

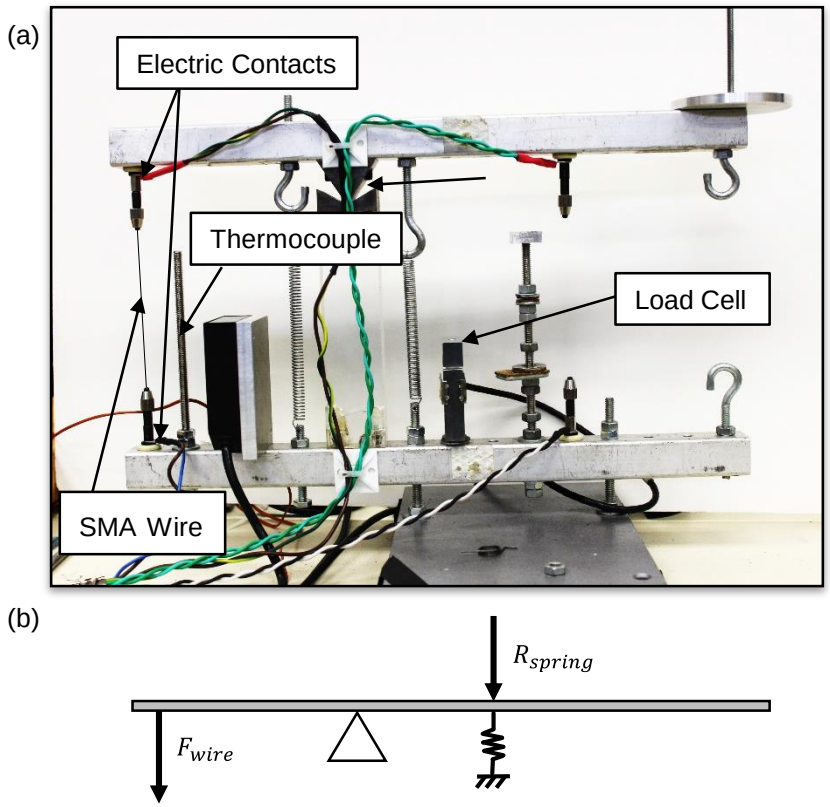

Figure 2.15. (a) Experimental test setup for actuator characteristic curve testing. (b) Free body diagram with proportional load acting as reaction force to wire stress.

The SMA wire is pre-conditioned to be at its free length in a completed martensite state and actuated to the austenite final temperature. The displacement and force is measured by the displacement sensor and the load cell.

Table 2.1. List of spring rates used for experimental actuator characteristic curve identification.

Spring	Spring Rate (N/mm)
1	17
2	21
3	60
4	618
5	974
6	1560

The results to the experimental verification of the actuator characteristic curve are shown in Figure 2.16. Data points F_b and u_i are the blocked force and free strain conditions where a solid steel bar and zero stress conditions were used respectively.

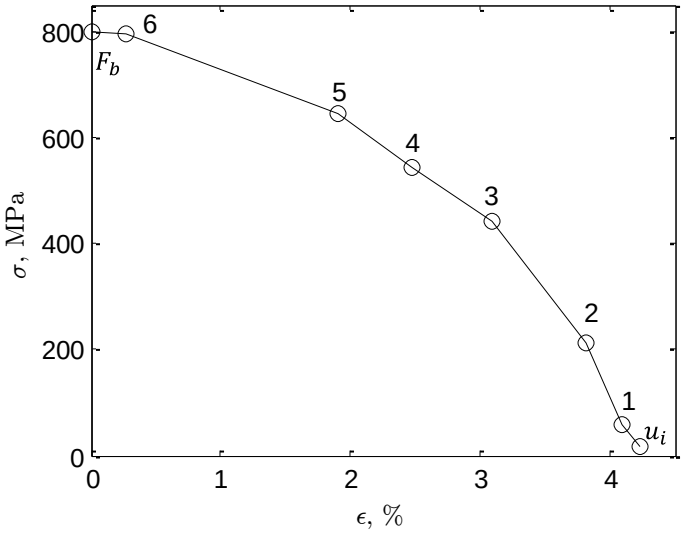

Figure 2.16. Experimental actuator characteristic curve.

The experimental characteristic curve confirms the shape of the theoretical characteristic curve. The discrepancy in the values for the blocked force and free strain conditions are due to the variations in SMA wire.

2.3.6. Maximum Work from Stress-Strain-Temperature Diagram

It is of interest to this thesis to look at the maximum work produced by full actuation at increasing temperatures on the stress-strain-temperature diagram. First, an energy conservative linear actuator will be considered. This is accomplished by linearizing the stress-strain curve at the martensite final temperature and austenite final temperature. Between the two systems, the temperature increase will be linearized. This is mathematically represented as

$$\sigma = \frac{1}{S}\varepsilon(\alpha\Delta T + 1) \tag{2.10}$$

where ε is the strain, ΔT is the change in temperature, α is 0.135 and is a thermal stress scalar, and S is a strain stress scalar and is equal to 0.035. At $T = T_{M_f}$ the thermal stress contribution is zero and the stress is equal to the slope of the strain scalar multiplied by the strain. With increasing temperature the thermal stress scalar acts as a multiplier to the strain scalar. The entire envelope can be seen in Figure 2.17.

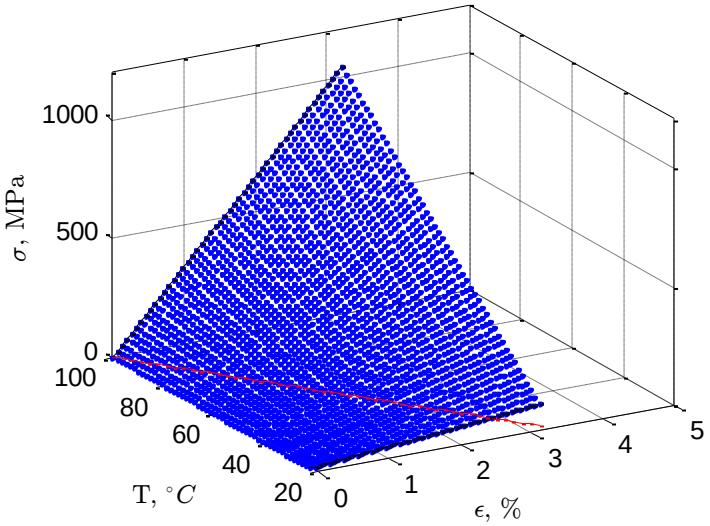

Figure 2.17. Linear stress-strain-temperature diagram with a linear conservative system.

For this analysis the starting temperature is equal to $T = T_{M_f}$ and steadily increases to $T = T_{A_f}$. The stress is always zero at this initial condition and is represented by the re-heating line running from $\varepsilon = 3.2\%$ at $T = T_{M_f}$ to $\varepsilon = 0\%$ at $T = T_{A_f}$. At each initial condition, the maximum actuation work is measured at each increasing final temperature; starting at small temperature increase to maximum temperature increase. The maximum work is calculated two different ways. First, an analytical approach is used where the maximum work is

$$W = \frac{1}{2}\sigma(\varepsilon - \varepsilon_0) \tag{2.11}$$

derived from maximum work from an actuator curve introduced in section 2.3.1. The second approach is a numerical approach where a trapezoidal method is used to integrate over the actuation curve

$$W = \sum_{k=1}^{N} \frac{\varepsilon_f - \varepsilon}{2N} [f(\varepsilon_1) + 2f(\varepsilon_2) + \cdots + 2f(\varepsilon_N) + f(\varepsilon_{N+1})] \tag{2.12}$$

where ε_f is the maximum strain at the isothermal location and $f(\varepsilon_k)$ is equation (2.6). Each incremental strain is calculated across an isotherm and the maximum value is recorded. These maximum work values are seen plotted as a function of the start and final temperatures in Figure 2.18. Being that both calculations for numerical and analytical methods are identical, only the analytical case is presented.

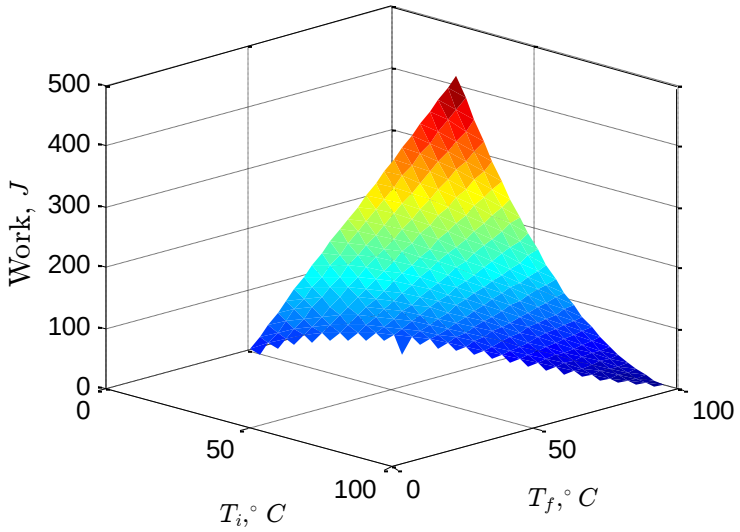

Figure 2.18. Maximum actuator work as a function of start and final temperature with linear stress-strain-temperature curve.

It can be seen that the maximum work is accomplished by the maximum change in temperature. This makes sense as the product of strain and stress are capable of being maximized at this location. More interesting, however, is the linear gradient as the temperature difference changes in both directions as T_i approaches T_f. This simply means that the higher the

increase in starting temperature the less work available to retrieve from the system. No advantages can be exploited by beginning at a higher temperature. Furthermore, it was of interest to look at this work as a function of the temperature change. This makes a general assumption that the heat transfer is conservative and linear for each increasing change in temperature of the wire, this is shown in Figure 2.19.

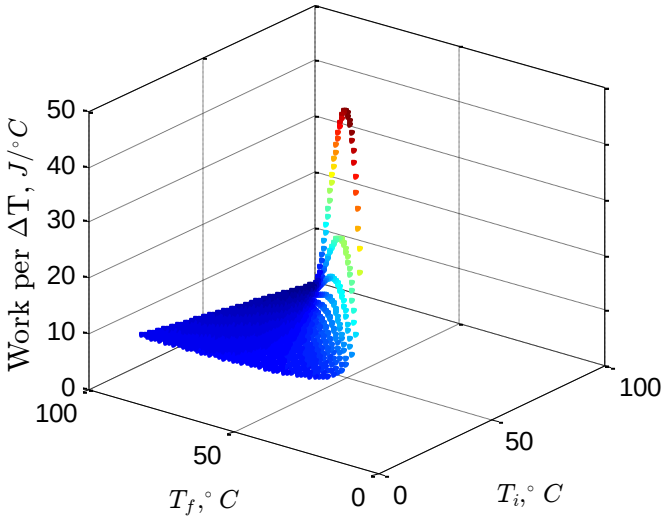

Figure 2.19. Work performed by a linearized shape memory alloy actuator normalized by change in temperature.

This graph shows maximum normalized energy steadily increasing when ΔT is minimum with it maximized at $T_i = 38.7$°C and $T_f = 40.3$°C. This would suggest that in a truly conservative system that maximum efficiency can be accomplished from very small changes in displacement with large changes in stress.

Next, the work and work per temperature are calculated for the nonlinear stress-strain-temperature envelope presented in Figure 2.12. Calculations are performed identically to the linearized case, however, the nonlinear equations are used for the stress-strain-temperature envelope. The results are shown in Figure 2.20. Similar to the linearized case, the maximum energy occurs at maximum temperature change. However, the gradient as final temperature approaches initial temperature at $T = T_{M_f}$ is nonlinear. This suggests, for efficiency purposes,

that even though maximum strain occurs when $T = T_{A_f}$ decremented changes from this value can still produce as much useful work to the system.

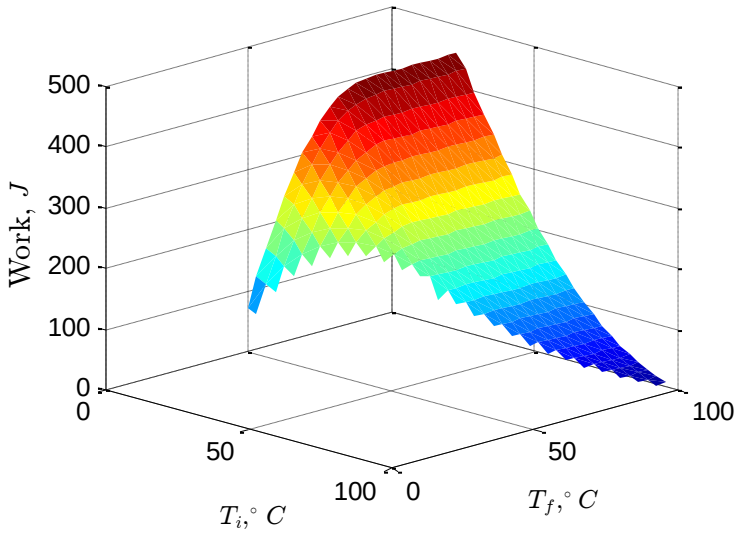

Figure 2.20. Work as a function of starting and completion temperature for a nonlinear SMA actuator.

Examination of the work per change in temperature graph gives similar, yet scaled results for efficiency.

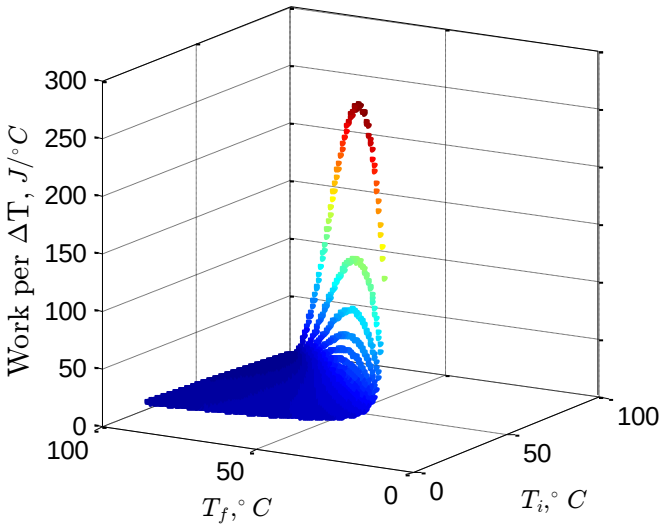

Figure 2.21. Work normalized by temperature change as a function of starting and completion temperature for a nonlinear SMA actuator.

2.4. Theoretical Parametric Analysis

2.4.1. Linear SMA Wire

Using a linear spring actuating the crank-slider mechanism, the kinematic and force analysis, as described in section 2.3. , is performed on a range of crank-slider geometries. Figure 13 presents the rocking angle of the crank-slider.

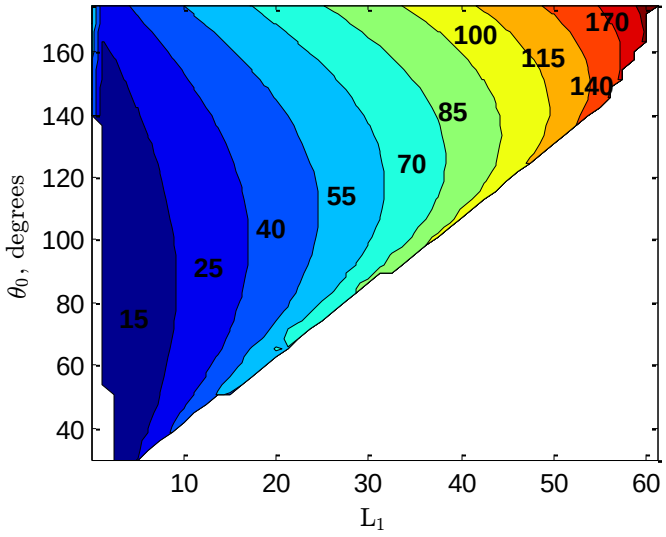

Figure 2.22. Rocking angle (degrees) for a linear spring actuated mechanism.

Similar to the rigid-body analysis of the crank-slider, moving from low frame lengths to high frame lengths, rocking angle steadily increases from very low rocking angle to 170 degrees. In contrast to the rigid-body analysis, to accomplish the 170 degree rocking angle the frame length needs to be 50% longer; 60 times as opposed to 40 times the rocker length. The five percent compliance of the spring is responsible for the increase in necessary frame length. Figure 2.23 and Figure 2.24 show the energy and torque outputs for the linear actuator.

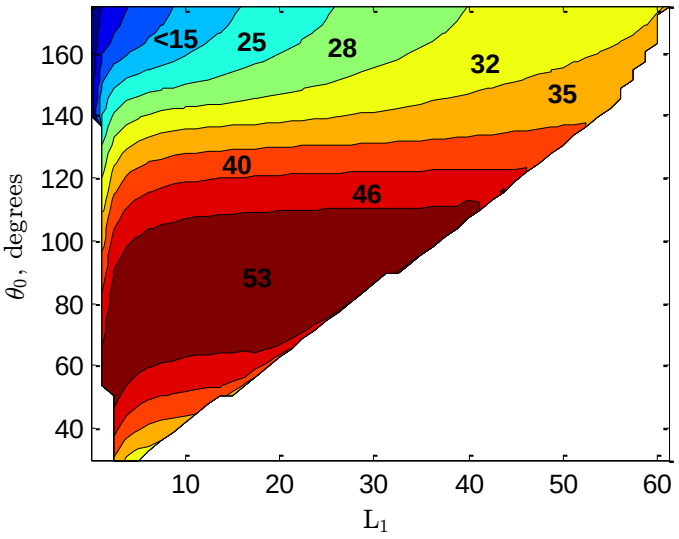

Figure 2.23. Maximum torque $(\mathrm{N} \times \mathrm{m})$ for a linear spring actuated mechanism.

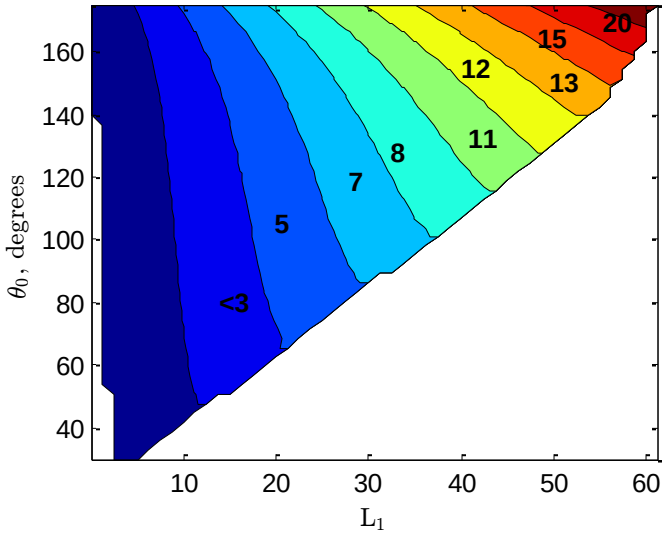

Figure 2.24. Maximum energy (Joules) for a linear spring actuated mechanism.

At low transmission angles, low torques are produced by the actuator because a majority of the force output is acting along the direction of the crank link. Figure 2.25 is a comparison between the actuator curve for the nonlinear isolated wire and the linear isolated wire curve applied to the crank-slider mechanism at starting angle of $\theta_0 = 175°$ and frame length of $L_1 = 38$.

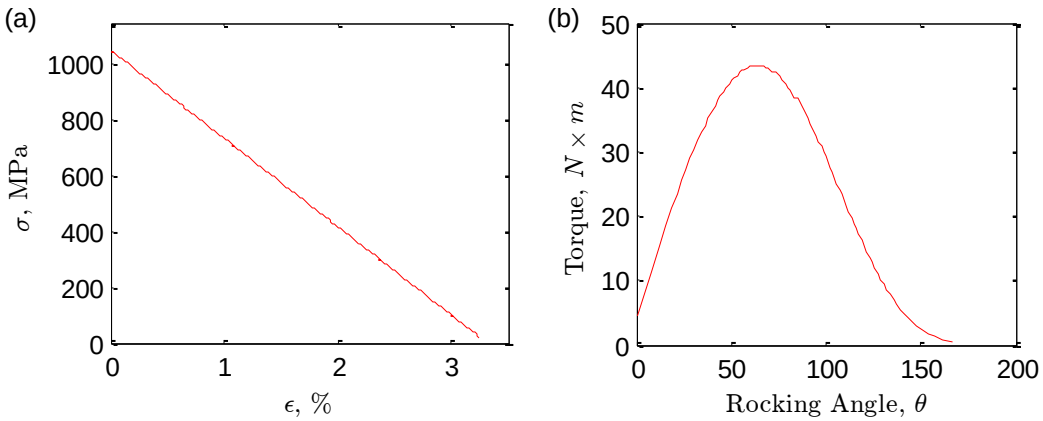

Figure 2.25. (a) Linear spring actuator curve and (b) crank-slider mechanism with linear wire actuation for initial conditions of $\theta_0 = 175°$ and $L_1 = 38$.

Lowering of the blocking force at short strokes can be seen in the crank-slider actuator curve. At high starting angles this is distinctly characteristic behavior. Due to the blocking force reduction at high start angles, the largest torque values are not seen at high initial angles. Peak torques are found at initial angles close to 45 degrees. Lower initial angles produce transmission angles close to 90 degrees where blocking force can be used entirely to generate torque.

Maximum work for the crank-slider is seen at high starting angles and high frame lengths. Stroke of the actuator has the largest effect on energy. High strokes produce high values of useful work.

2.4.2. Nonlinear SMA Wire

A parametric study of the SMA nonlinear actuator curve for differing crank-slider mechanisms is presented in Figure 2.26 and Figure 2.27.

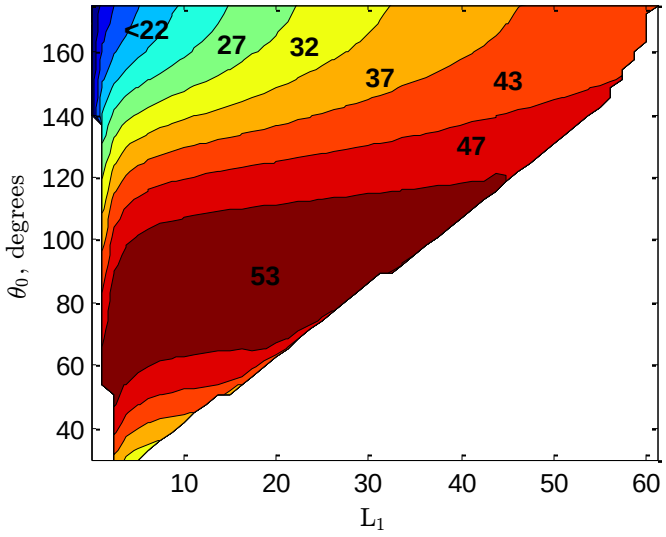

Figure 2.26. Peak torque $(\mathrm{N} \times \mathrm{m})$ for a non-linear spring actuated mechanism.

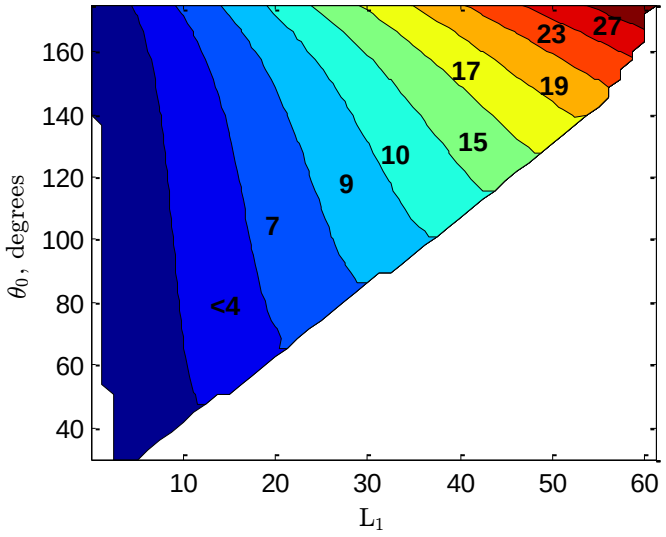

Figure 2.27. Maximum work (Joules) for non-linear spring actuated mechanism.

Trends in results for nonlinear actuator curves are similar to those of linear curves. Due to the definition of the free-stroke condition, and the linear actuator curve being derived from the nonlinear curve, rocking angles for each actuator are identical and thus are not displayed. Maximum energy is higher in the nonlinear case, steadily increasing to larger values at high

frame lengths and large starting angles. Higher torque values are also seen across the analysis with smaller differences in the peak torque ranges.

2.4.3. Comparison of Idealized Linear and Nonlinear Wires

A simple inspection shows little discernable difference in the values of peak energy and peak torque. Performing a point by point comparison reveals the differences between torque and energy. The difference is defined as:

$$\Delta x = x_{NL} - x_L, \tag{2.13}$$

where x_{NL} and x_L are the nonlinear and linear values respectively. The results are shown in Figure 2.28

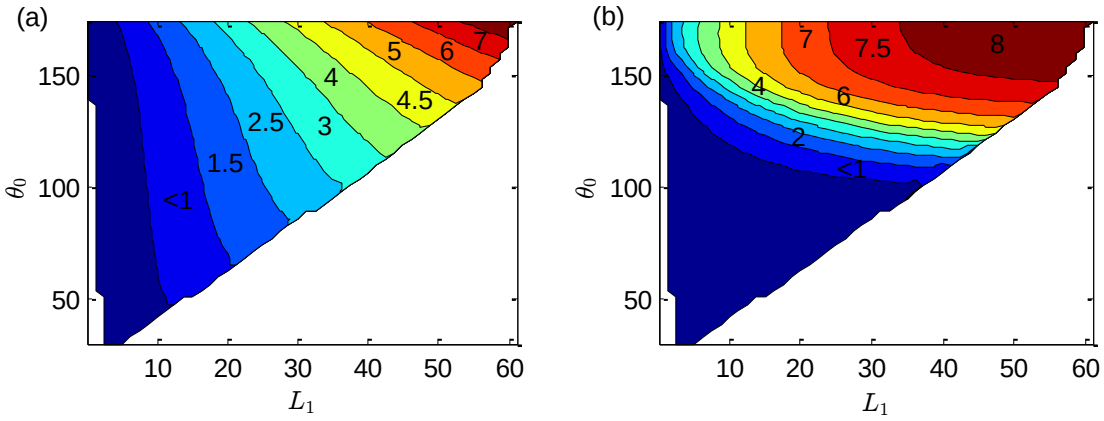

Figure 2.28. Magnitude difference in (a) peak work (J) and (b) peak torque $(\mathrm{N} \times \mathrm{m})$ by geometry.

This behavior is explained by examining the difference between the actuator curves. Energy is a function of the blocking force at a particular stroke. Through the entire nonlinear wire actuator curve, blocking force is always greater in the nonlinear case, seen in Figure 2.14. This leads to larger torque values and more useful work over the stroke of the crank-slider mechanism. An example is shown in Figure 2.29.

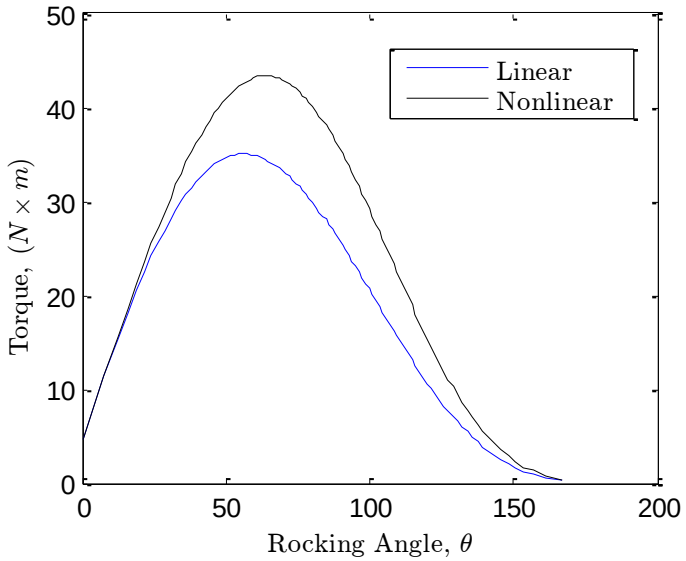

Figure 2.29. Linear and nonlinear actuator curves for 175 (degree) starting angle and 38 frame length.

A point-by-point comparison of percent difference between the nonlinear and linear curves is important to see the overall effects of linearizing the wire actuator curve. The percent difference is defined by the equation:

$$\%diff = \frac{x_{NL} - x_L}{x_{NL}} * 100\%. \tag{2.14}$$

Figure 2.30 presents the percent difference of energy and torque between linear and non-linear crank-slider mechanisms.

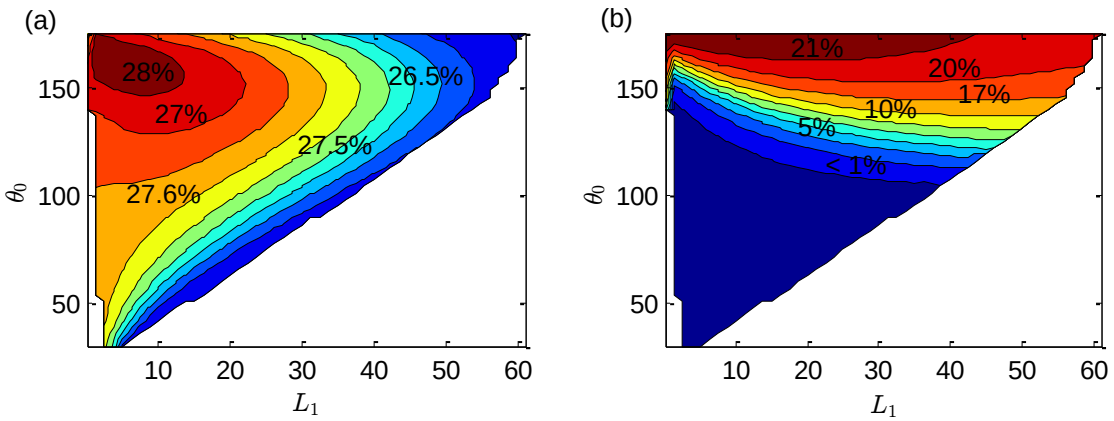

Figure 2.30. Percent difference of (a) work (J) and (b) torque $(\mathrm{N} \times \mathrm{m})$ between linear and nonlinear crank-slider actuators.

An error in maximum energy is evenly present across the entire domain with higher error values for shorter frame lengths and high starting angles. This is attributed to the low strokes and low transmission angles for these parameters. Torque values have a larger gradient with little to no difference in the high torque ranges. The high torque range, which is present across the 45 degree band, have high transmission angles which the full blocking force can be applied in each case. As the geometry deviates to lower initial transmission angles, the error in maximum torque increases. These are areas where the linear and nonlinear actuator maximum torque is located in the middle of the stroke and where the nonlinear wire actuator has higher forces. This deviation is important to note for choosing design parameters for an actuator. With the nonlinear model, it is possible to observe higher stroke lengths, higher energy efficiency, and moderately higher torques with the same design parameters.

2.5. Experimental Parametric Analysis

A kinematic test bed is designed to verify the kinematic motion equations examined in this chapter for rigid body and SMA actuated curves. A secondary objective for this experiment is to validate a machine vision method for measuring rigid-body mechanism motion to use for future experiments with SMA actuated bodies.

2.5.1. Experimental Setup

The kinematic experimental setup is shown in Figure 2.31. The frame of the mechanism is composed of rigid mounting blocks at points A and C; these blocks are used to mount a return actuation torsional spring and a servo motor respectively. A crank is fitted at mounting point A by a shaft with a torsional spring connecting the crank to the mounting block for return stroke of the actuator. Point B is the tip of the crank. The slider is accomplished by connecting a nylon wire from the crank tip to a spool attached to a servo motor at point C. Rotating the servo motor at a constant angular velocity will mimic the slider moving at a constant linear velocity.

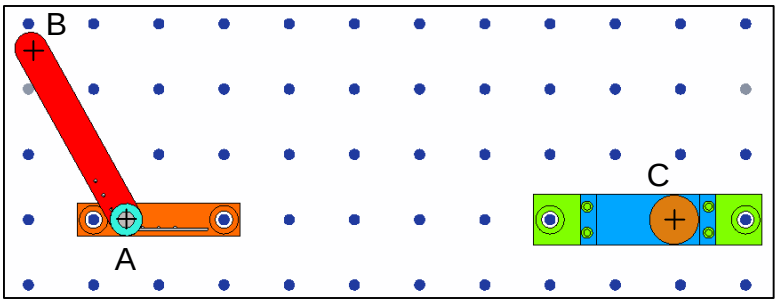

Figure 2.31. Overhead view of the baseline kinematic mechanism.

The motion of the mechanism during actuation is recorded using a Point Grey Black Fly 3 camera where points A, B, and C are tracked using the pattern recognition function of OpenCV, an open source camera vision software. Figure 2.32 shows an isometric view of the kinematic test bed setup.

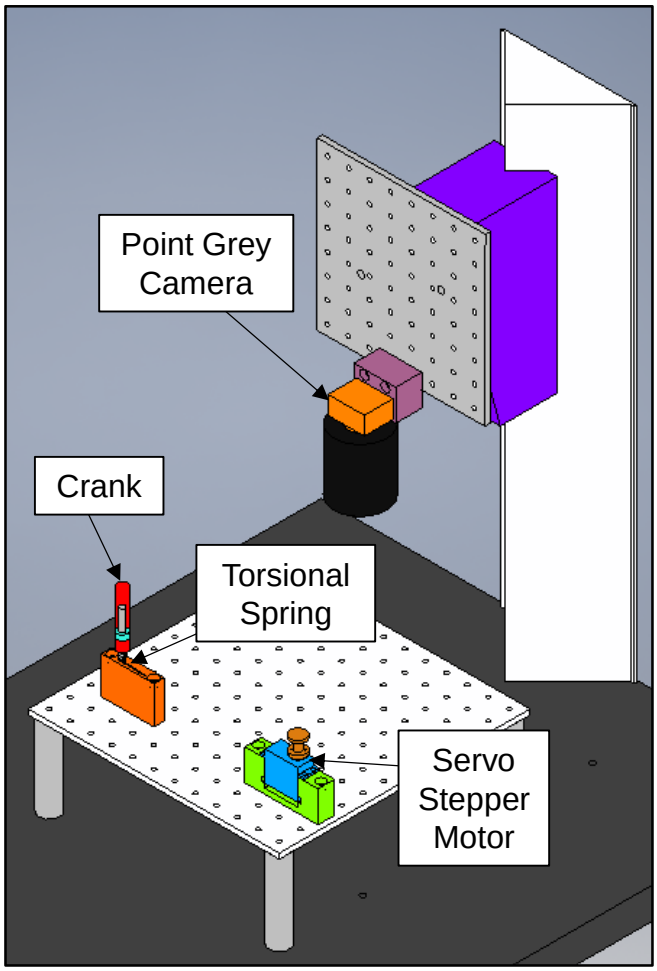

Figure 2.32. Isometric view of kinematic test bed.

Figure 2.33 is an example image captured by the camera. The points A, B, and C are tracked based on color detections of green, red, and blue circles. Post processing of mechanism motion is performed in MATLAB. The motion of the crank-slider mechanism is achieved by calibrating pixel width and height to real units. Based on the position of the three patterns over the duration of the recording, the motion of the crank-slider mechanism can be determined.

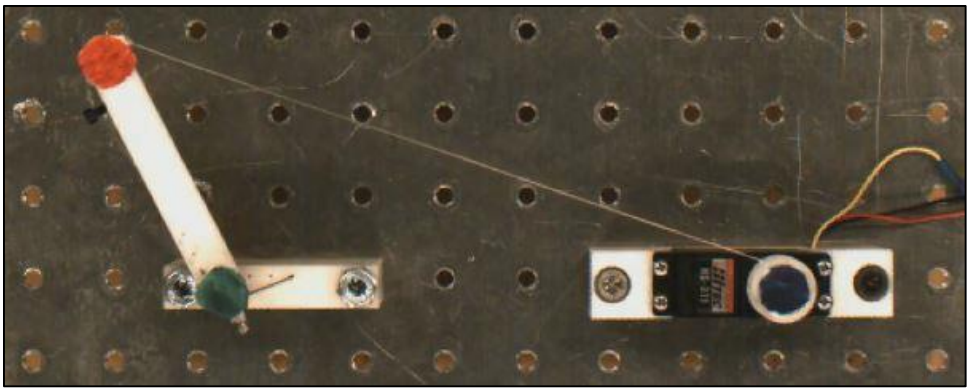

Figure 2.33. Image from motion capture of kinematic bed test setup.

2.5.2. Torsion Spring and Spring/Pulley Rigid Body

The values used for the theoretical calculations are shown in Table 2.2. Kinematic equations (2.1), (2.2), and (2.3) are used. Results for crank rectilinear and angular velocities are displayed in Figure 2.34 -

Figure 2.36.

Table 2.2. Link-lengths and slider velocity used for theoretical results.

Variable	Value
L_1	160.8 mm
L_2	72.4 mm
L_{3_0}	105.4 mm
$\vec{V}_{C'/C}$	14.0 mm/s

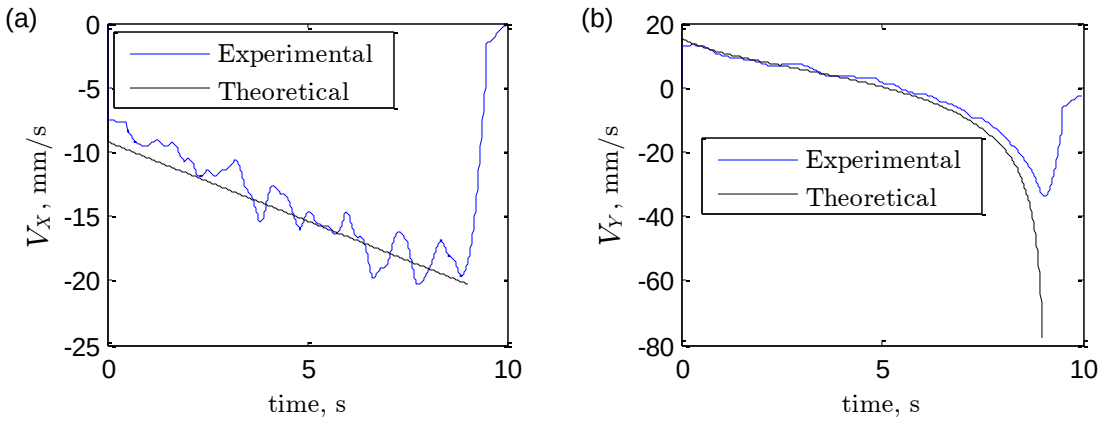

Figure 2.34. (a) Velocity of point B in the x-direction and (b) velocity in the y-direction.

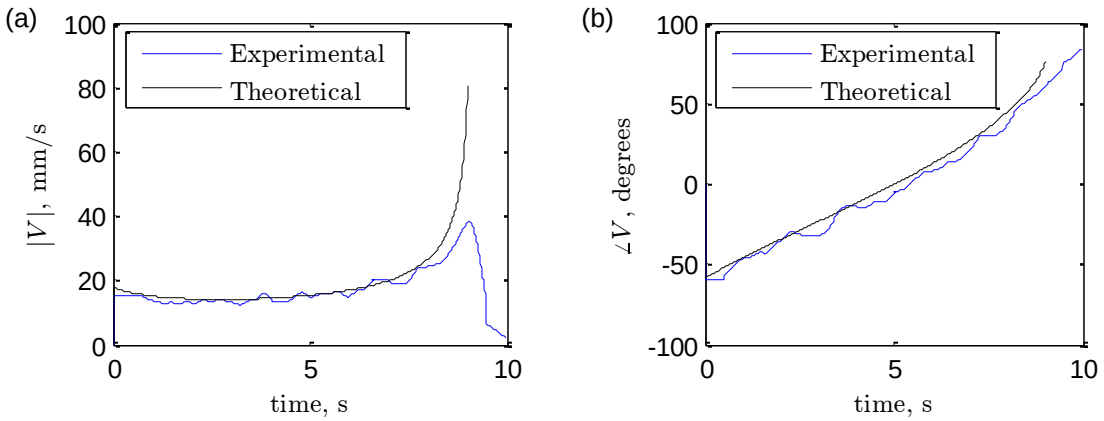

Figure 2.35. (a) Magnitude of velocity of point B and (b) direction of velocity of point B.

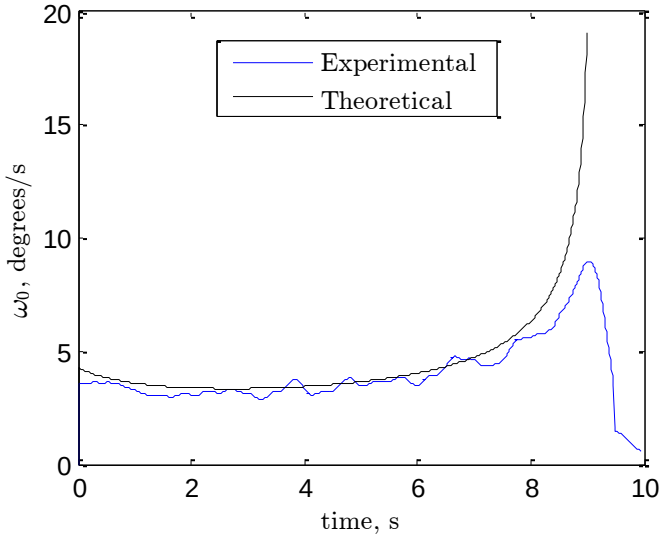

Figure 2.36. Angular velocity of Link 2.

The theoretical and experimental values closely match for all plots. Theoretical deviation from experimental results near the end of actuation is explained by the dynamics of the experimental system. The experimental test setup uses a torsional spring and nylon wire for return actuation, force effects that are not accounted for in the theoretical kinematic equations. The dynamics of the system dominate the experimental results when the wire spool is completely drawn out – which only leave the torsional spring dynamics to generate motion.

Based on the theoretical and kinematic correlation, both the machine vision solution for measuring kinematic motion is validated and the kinematic equations are verified.

2.5.3. SMA Actuated Kinematic Device

An SMA actuated kinematic mechanism was 3D printed and mounted to the kinematic test bed in order to validate a test point on the SMA nonlinear actuator parametric analysis contour plot. Since SMA wire actuation is a non-linear process, rocking angle is the only validation point to be investigated on the parametric analysis. The kinematic mechanism with labeled points can be seen in Figure 2.37

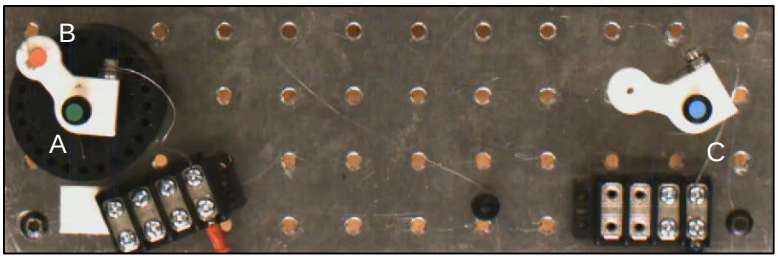

Figure 2.37. Overhead view of SMA actuated kinematic mechanism captured with OpenCV software.

The initial conditions and results of the SMA wire test mechanism are presented in Table 2.3. Initializing the SMA wire in detwinned martensite state the wire is heated to the austenite final temperature where the starting and final angle are analyzed in MATLAB.

Table 2.3. Experimental conditions for experimental SMA wire actuated mechanism.

Feature	Length
L_1	305 mm
L_2	24.1 mm
θ_0	125°
θ_f	98°
$\Delta\theta_{theoretical}$	25°
$\Delta\theta_{experimental}$	27°

The experimental results correlate closely, as visualized in Figure 2.38, with the theoretically calculated nonlinear SMA actuated parametric analysis. Future experimental results are desired for the most interesting areas of the contour plot but this validation point grants confidence in the general results of the parametric analysis.

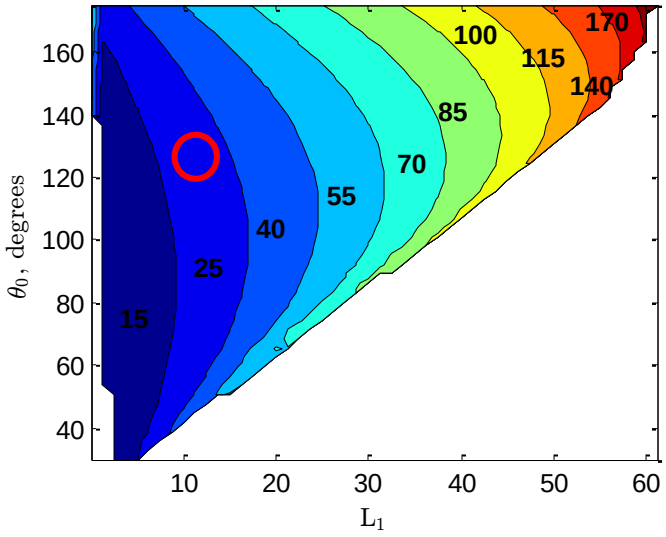

Figure 2.38. Nonlinear SMA actuated mechanism. Experimental initial condition is shown by the red circle.

2.6. Comparison to Biological Muscle Actuation

Empirical inspiration for design parameters can be found by examination of the human musculoskeletal system. In order to compare the musculoskeletal performance metrics to that of the shape memory alloy actuated mechanism, the actuation curve for human muscle must be obtained. Chang [18], in 2007, measured the normalized muscle force compared to muscle strain and found a similar actuator curve to that of SMA wire as can be seen in Figure 14. The muscle alone contracts up to 40% of its total length.

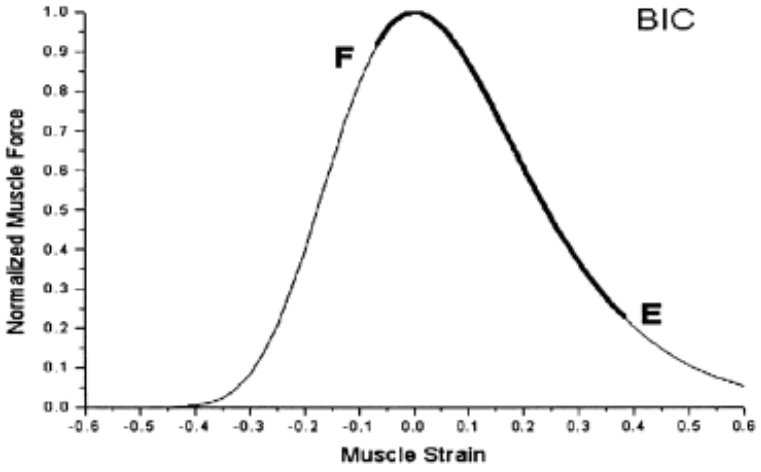

Figure 2.39. Normalized muscle force vs muscle strain for Biceps Brachii muscle as measured by Chang et al [18].

The skeletal system of the human arm is composed of the humerus and radius. The musculotendon system is composed of the proximal and distal biceps tendons and the biceps brachii itself. The distal biceps tendon is attached to the radius at the radial tuberosity. When the biceps brachii is actuated, and contracts, it generates a force at the radial tuberosity producing rotation. In terms of the crank-slider mechanism, Figure 1, the humerus is equivalent to the frame, link L_1. The distance from the elbow joint, moving along the radius, up to the radial tuberosity is link L_2. The slider, on link L_3, represents the contraction of the muscle.

Surveying the literature for biceps brachii, proximal and distal biceps tendons lengths – the measurements are found to be 22.9 cm, 11.16 cm, and 6.3 cm respectively (Table 2.4) [19-22].

Table 2.4. Reported lengths, in cm, of human anatomy.

Specification	Murray [19]	Kovack [20]	Garner [21]	Walton [22]
Biceps Brachii Muscle	22.9		14.22	
Proximal Biceps Tendon		11.16		
Distal Biceps Tendon				6.3

Conducting similar literature survey for skeletal lengths result in 33.48 cm for the humerus and 24.8 cm for the radius with the radial tuberosity located at 3.25 cm from the elbow joint [23, 24]. The musculoskeletal arm along with lengths are illustrated in Figure 2.40.

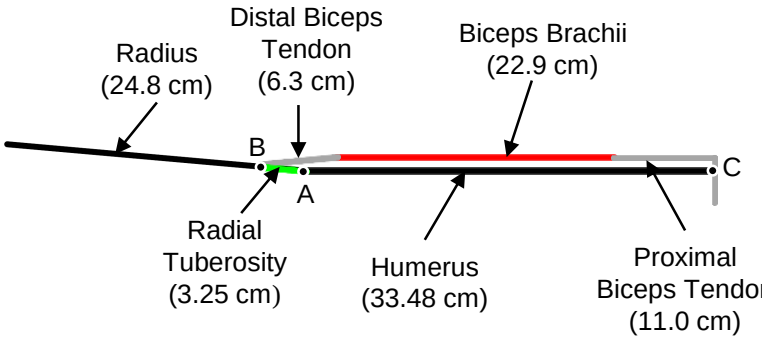

Figure 2.40. Anatomical lengths of musculoskeletal system of human arm.

In this study, composition of muscle from the musculotendon length, from Zuylen et al. [25], is assumed to be 55%. Also, the contractile muscle part changes by roughly 25% of the optimum length from maximum flexion to maximum extension.

Using the actuation properties of 25% length contraction for the biceps brachii muscle in the crank-slider mechanism model produces similar results to that of the SMA wire. Figure 2.41-Figure 2.43 display response of a muscle-actuated crank-slider mechanism.

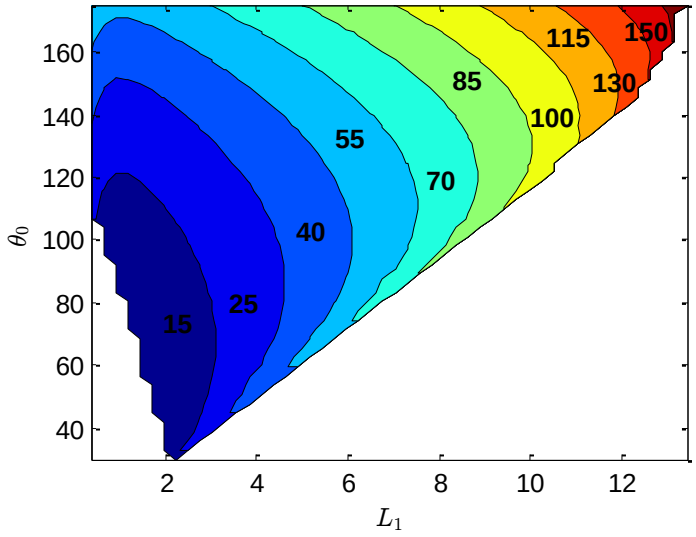

Figure 2.41. Rocking angle (degrees) results for a muscle actuated mechanism with normalized link-lengths to length of the radial tuberosity.

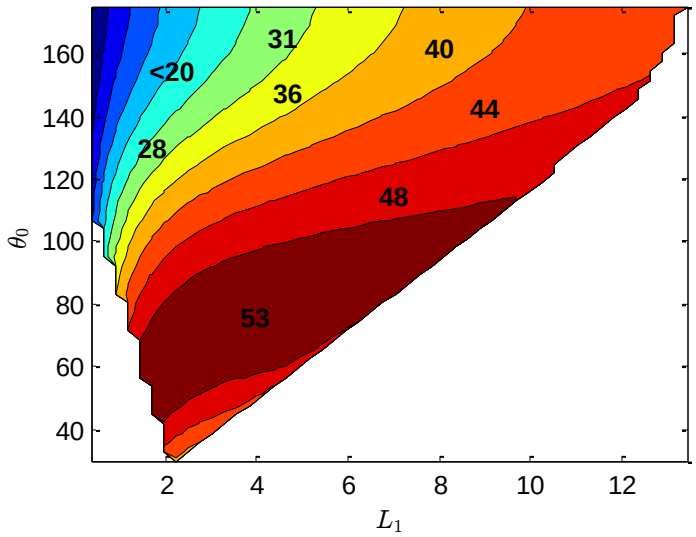

Figure 2.42. Torque $(\mathrm{N} \times \mathrm{m})$ results for a muscle actuated mechanism with normalized link-lengths to length of the radial tuberosity.

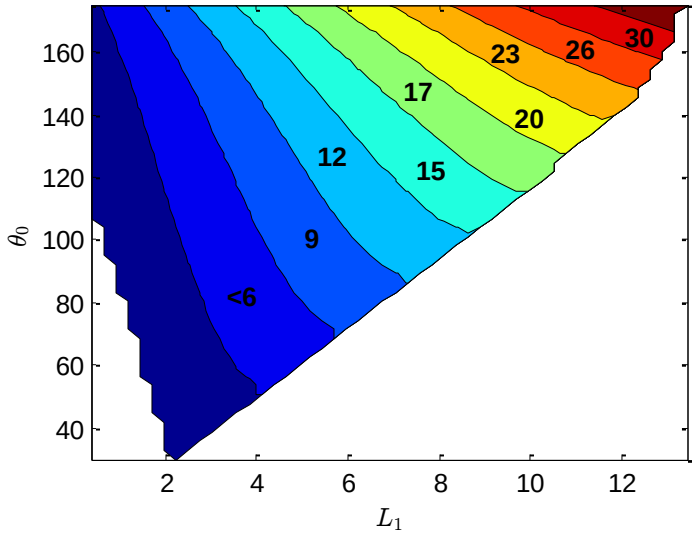

Figure 2.43. Work (Joules) results for a muscle actuated mechanism.

All results from the parametric analysis are normalized to the length of the rocker link. Therefore, in order to determine how the human arm is designed based on kinematic properties, the links of the humerus and muscle must be normalized to the link of the radial tuberosity. Doing so, results in the normalized link lengths presented in Table 2.5.

Table 2.5. Lengths of musculoskeletal arm normalized to the radial tuberosity.

Section	Normalized Length
Radial Tuberosity	1.00
Distal Biceps Tendon	1.94
Proximal Biceps Tendon	2.46
Biceps Brachii	7.02
Humerus	10.30

The starting angle of the human arm is close to 175° at full extension. Projecting the starting angle with the normalized link-length of the humerus (Table 2.5) onto Figure 2.41 the rocking angle is found to be 140°. This indicates that the actuation assumptions for the muscle actuator are correct as this rocking angle is anatomically correct. Furthermore, it suggests that

the human arm is designed to perform maximum work, with high torque capabilities, over large ranges. A comparison of SMA and human muscle actuation peak results are summarized in Table 2.6.

Table 2.6. Optimal design parameters of crank-slider mechanism for maximum rocking angle ($\Delta\theta$), torque (T), and work (W).

	Max $\Delta\theta$ (degrees)			**Max T ($\mathbf{N \times m}$)**			**Max W ($\mathbf{J}$)**		
Actuator Model	Value	L_1	θ_0	Value	L_1	θ_0	Value	L_1	θ_0
Linear SMA	167	60	175	53	20	86	20	60	175
Nonlinear SMA	167	60	175	53	20	86	28	60	175
Human Arm	166	13	175	53	6.7	86	34	13	175

In designing a prosthetic device to perform the same types of work and replicate the human arm as closely as possible the biomechanical analysis suggests that staying in the large rocking angle and work range is necessary. One difficulty with doing so in the shape memory alloy actuated curve is the frame lengths tend to become very large, unreasonably large for an arm. To counteract this increase in frame lengths, the position where the SMA wire connects to the radius must be much closer to the elbow joint for the prosthetic device. This will increase stress in the joints and requires stress analysis.

2.7. Conclusions

In this chapter, the kinematics and energy characteristics of a crank-slider mechanism actuated by an experimentally characterized SMA wire is presented. The theoretical stress-strain-temperature curve for the shape memory alloy wire is reviewed and the experimental response of the wire is simplified to an idealized behavior. The actuator characteristic curve for the SMA wire is calculated by placing the wire in series with a variable-stiffness spring and calculating force and displacement over a range of spring constants. The actuator characteristic curve shape is verified with experimental results by actuating the SMA wire in series with springs of variable stiffness. Using idealized linear and nonlinear forms of the SMA actuator

curve, metrics such as rocking angle, energy, and torque are calculated for a range of crank-slider geometries. Rocking angles of up to 170° are calculated with a starting angle of 175°, and frame length of approximately 60 times that of the rocker. Force analysis of both forms of the actuator curve showed highest torques occur when the blocking force is applied at transmission angles of 90°; these transmission angles are present at low frame lengths and low starting angles. The SMA actuated crank-slider mechanism performs the most useful-work at high starting angles and high frame lengths due to moderate torques generated over a long actuation stroke. The nonlinear actuator curve performs better across all performance metrics with large deviations from the linear curve at areas of interest.

A kinematic test bed using machine vision for motion analysis is proposed and verified using theoretical calculations for kinematics. To verify the SMA actuated mechanism a test point was introduced and kinematics recorded with the OpenCV software. The rocking angle of the contour plot for the SMA actuated mechanism is correlated to experimental results.

A literature review is performed on musculoskeletal lengths in order to determine link-lengths for the human arm and actuator characteristics for the human muscle. The muscle actuator characteristics are entered into the crank-slider simulation and compared to that of the SMA actuated mechanism. The literature review link-lengths are normalized to the radial tuberosity leading to suggestions on how to design an SMA actuated prosthetic device to perform similarly to the human arm.

CHAPTER 3

DYNAMIC STRUCTURAL BEHAVIOR

3.1. Introduction

This chapter seeks to understand the forces, work, and motion of the crank-slider mechanism in different configurations. This is done by developing a kinetics model for the dynamic motion of the crank-slider mechanism. Using the model, phase portrait analysis is completed for damped and undamped systems. Specific configurations are further explored where energy analysis is deployed for additional understanding. The study of these effects improve fundamental understanding of prosthetic arm behavior under external stresses.

3.2. Kinetics Model

The kinematics model of the crank-slider mechanism in the previous chapter has forces not yet described. These are now covered in the kinetics model. The forces acting on the crank-slider mechanism are as shown in Figure 3.1. The spring force of the SMA wire is considered to be a linear spring with a constant contracted length. At point B a constant proportional load is acting normally to the crank at all times; effectively producing a torsional spring. Finally, the resistance to acceleration is the moment of inertia of the crank (I). The wire mass is assumed to have negligible inertia. A free body diagram is presented in Figure 3.1.

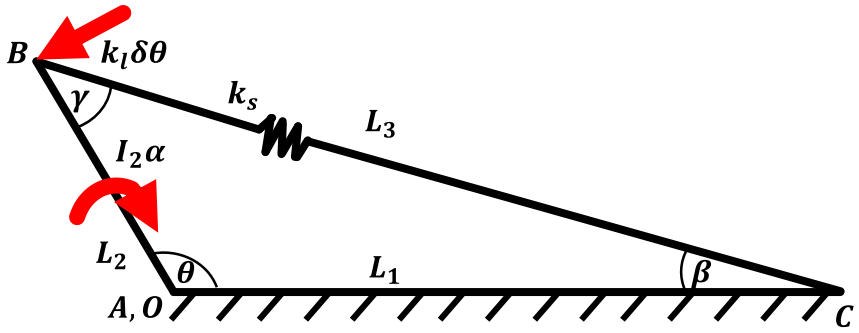

Figure 3.1. Crank-slider mechanism with proportional load acting normal to tip of crank.

In the figure L_1, L_2 and L_3 are the frame, crank, and contractile spring element respectively. The spring elements k_s and k_l are the linear spring constant for the contractile spring element and torsional spring constant for the mechanism loading. A Lagrangian and a Newtonian formulation of the equation of motions are presented next.

3.2.1. Energy Method

To begin the Lagrangian formulation the kinetic energy, T, and potential energy, U, equations are produced.

$$T = \frac{1}{2} I_2 \dot{\theta}^2 \tag{3.1}$$

$$U = \frac{1}{2} k_l (\theta_0 - \theta)^2 + \frac{1}{2} k_s \left(L_3(\theta) - L_{3_0}\right)^2 \tag{3.2}$$

where $\dot{\theta}$ is the angular velocity of the crank. The Euler-Lagrange equation is

$$\frac{d}{dt}\left(\frac{\partial L}{\partial \dot{\theta}}\right) - \frac{\partial L}{\partial \theta} = 0 \tag{3.3}$$

where the Lagrangian operator is defined as,

$$L = T - U. \tag{3.4}$$

Substituting T and U,

$$L = \frac{1}{2} I_2 \dot{\theta}^2 - \frac{1}{2} k_l (\theta_0 - \theta)^2 + \frac{1}{2} k_s \left(L_3(\theta) - L_{3_0} \right)^2. \tag{3.5}$$

The first term of Eq. ((3.3) can be derived as,

$$\frac{\partial L}{\partial \dot{\theta}} = I\dot{\theta} \tag{3.6}$$

$$\frac{d}{dt}\left(\frac{\partial L}{\partial \dot{\theta}}\right) = I\ddot{\theta}. \tag{3.7}$$

The second term becomes,

$$\frac{\partial L}{\partial \theta} = -k_l(\theta_0 - \theta) - k_s\left[L_3(\theta) - L_{3_0}\right] L_3'(\theta) \tag{3.8}$$

where

$$L_3(\theta) = (L_1^2 + L_2^2 - 2L_1 L_2 \cos\theta)^{\frac{1}{2}} \tag{3.9}$$

$$L_3'(\theta) = -L_1 L_2 \sin\theta / L_3(\theta). \tag{3.10}$$

Combining Eq. (3.7) and (3.8) leads to,

$$\tfrac{d}{dt}\left(\tfrac{\partial L}{\partial \dot{\theta}}\right) - \tfrac{\partial L}{\partial \theta} = -k_l(\theta_0 - \theta) - k_s\left[L_3(\theta) - L_{3_0}\right] L_3'(\theta). \tag{3.11}$$

Simplifying (3.11) produces,

$$I\ddot{\theta} + k_l(\theta_0 - \theta) - k_s L_1 L_2 \sin\theta \left(1 - L_{3_0}/L_3\right) = 0. \tag{3.12}$$

3.2.2. Force-Balance Method

The Newtonian formulation equates the inertia of the crank to the summed moment of the torsional spring and the moment arm due to the contraction of the wire. This force-balance is illustrated in Figure 3.2.

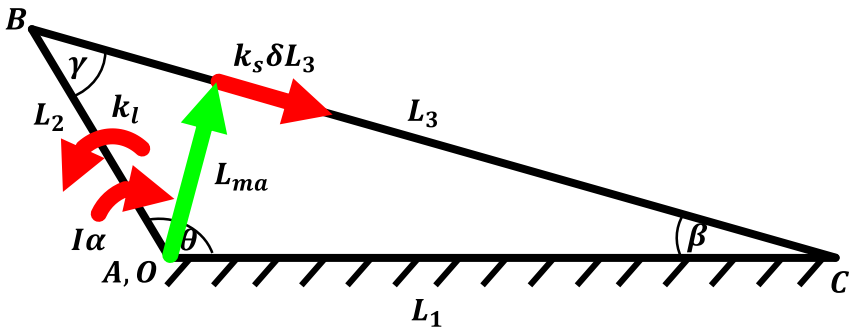

Figure 3.2. Free body diagram used for deriving the crank-slider mechanism with Newton's method.

Using Figure 3.2, Newton's method leads to

$$\sum M_O = I_0\alpha \tag{3.13}$$

$$I_0\alpha = k_l(\theta_0 - \theta) - L_{ma}k_s\left(L_3 - L_{3_0}\right) \tag{3.14}$$

where,

$$L_{ma} = L_2 \sin\gamma = L_1L_2 \sin\theta/L_3. \tag{3.15}$$

Eq. (3.14) simplifies to

$$I\ddot{\theta} + k_l(\theta_0 - \theta) - k_sL_1L_2 \sin\theta \left(1 - L_{3_0}/L_3\right) = 0. \tag{3.16}$$

The solutions to the Lagrangian and Newtonian methods are equivalent as expected.

3.3. Phase Portraits

The equation of motion for the dynamics of the simplified crank-slider mechanism is a second order system. A common quantitative tool for analyzing the dynamics of a second order system is the phase portrait diagram. The phase portrait consists of an x-y axis with the first-order state-space variables located on each of the axes. The differential equation (3.16) can be reduced to the following first order systems:

$$\dot{\theta}_1 = \theta_2 = \omega \tag{3.17}$$

$$\dot{\theta}_2 = \frac{k_I}{I}(\theta_0 - \theta_1) - \frac{k_S}{I} L_1 L_2 \sin\theta_1 \left[1 - L_{3_0}/L_3\right] \tag{3.18}$$

A vector field is commonly plotted on the phase portrait diagram. The vector field is a set of instantaneous solutions of the differential equation given the initial conditions at each point on the phase portrait. As an example, an inverted pendulum is shown in Figure 3.3.

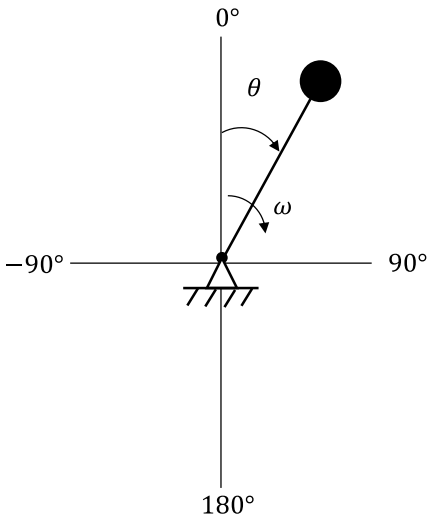

Figure 3.3. Free body diagram for an undamped inverted pendulum.

Figure 3.4 shows the phase portrait for an undamped inverted pendulum with initial conditions of $\theta_0 = \frac{\pi}{4}$ radians and $\omega_0 = 0$ radians/s. The path of the example solution of the differential equation is shown by the blue path. This path creates a closed loop oscillation due to no damping term present in the differential equation. The vector field is shown by red arrows.

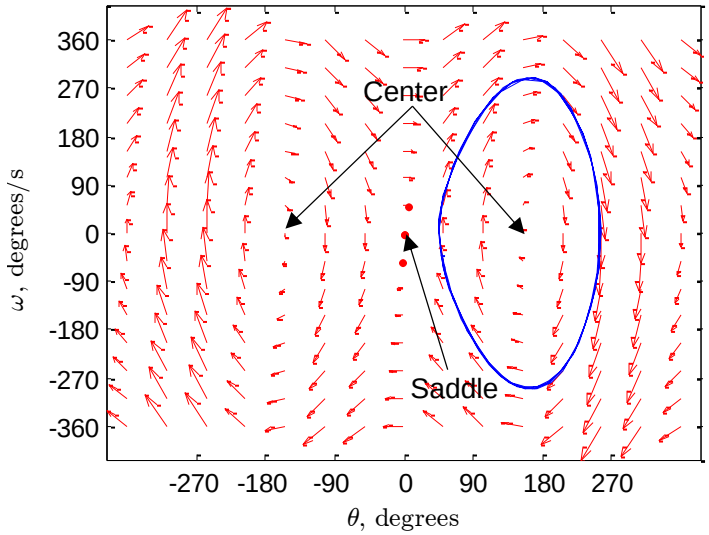

Figure 3.4. Phase portrait diagram for an inverted pendulum. Equilibrium points are highlighted by arrow indicators. Time independent path of the system is shown by the blue line.

By examining the vector field, several points of interest can be identified that characterize dynamic behavior. These features are the stable and the unstable equilibrium positions. Equilibrium are positions on the phase portrait that, by inspection, will determine the system dynamics around an initial condition. Equilibrium positions are categorized as stable and unstable nodes, stable and unstable foci, saddle point and center. These patterns emerge due to the eigenvalues of the solution of the differential equation about the point. Each equilibrium point is further characterized by stability. Stable equilibria exhibit dynamic phenomena that when a small perturbation is applied the system response will settle into the equilibrium position. When the system at unstable equilibria are subjected to small perturbations the response can result in nonlinear oscillations and/or divergent behavior. Two of these points have been identified in Figure 3.4. An equilibrium center is located at $\theta = \pi$ radians and $\theta = -\pi$ radians. The center is caused by complex conjugate imaginary eigenvalues about the equilibrium position and causes the system to oscillate about the center node. The saddle is caused by positive and negative eigenvalues and causes the system to move away from the unstable equilibrium position. Similar equilibrium positions will be investigated for the crank-slider mechanism.

The crank-slider mechanism with initial conditions of ω_0 and θ_0 is illustrated in Figure 3.5. The differential equation describing such system was given in Eq. (3.18). To reduce the number of potential parameter permutations in this analysis, L_2 is normalized to a value of one.

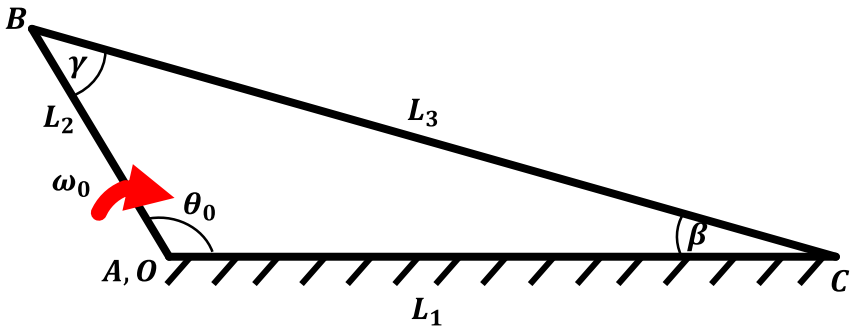

Figure 3.5. Crank-slider mechanism with initial conditions labeled.

First, the undamped system is considered. In each of the following phase portraits, the system variables $k_l, k_s, L_1,$ and I are assumed to be one unless otherwise noted. This condition will be referred to as the baseline configuration. The phase portrait for the crank-slider mechanism at initial conditions of $\theta_0 = 12\pi/13$ radians, $\omega_0 = 0$ radians/s with a frame length of $L_1 = 10$ is shown in Figure 3.6. It can be seen at these initial conditions the response indicated by the blue path is a continuous oscillation. As the response path diverts from of the y-axis the response is increasing in angular velocity. For the x-axis response, as the magnitude in difference of the angular position increases, there will be a larger oscillation in the response. There is a single equilibrium point located in the phase portrait, located at $\theta = 3$ radians, and $\omega = 0$ radians/s.

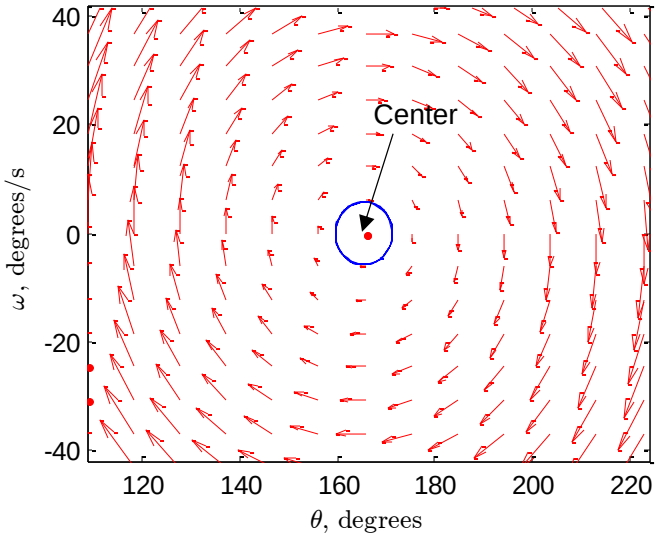

Figure 3.6. Phase portrait for a crank-slider mechanism with $L_1 = 10$.
Initial conditions: $\theta_0 = 12/13\,\pi$ radians $\omega_0 = 0$ radians/s.

The equilibrium type can be determined by linearizing the differential equation and inspecting the eigenvalues around the equilibrium position. This is done by first expanding the nonlinear differential equation, Eq. (3.18), to

$$\ddot{\theta} = \frac{k_l}{I}(\theta_0 - \theta) - \frac{k_s}{I} L_1 L_2 \sin\theta + \frac{k_s}{I} L_1 L_2 \sin\theta \frac{L_{3_0}}{\sqrt{L_1^2 + L_2^2 - 2L_1 L_2 \cos\theta}}. \tag{3.19}$$

The differential equation can be linearized by performing a Taylor series approximation about some equilibrium point, θ_E. The Taylor series definition is

$$f(\theta_E + \Delta\theta) \approx f(\theta_E) + f'(\theta_E)\Delta\theta + h.o.t. \tag{3.20}$$

Due to the objective of linearizing the nonlinear differential equation, all higher order terms $(h.o.t)$ are dropped in the expansion as they are nonlinear in nature.

By inspection of Eq. (3.19) the first term is a linear term, therefore, only the second and third terms require a Taylor series approximation; these are Eq. (3.21) and Eq. (3.22) respectively.

$$\frac{k_s}{I} L_1 L_2 \sin(\theta_E + \Delta\theta_E) = \frac{k_s}{I} L_1 L_2 \sin\theta_E + \frac{k_s}{I} L_1 L_2 \cos\theta_E\, \Delta\theta \tag{3.21}$$

$$\frac{k_s}{I}L_1L_2\sin(\theta_E+\Delta\theta)\frac{L_{3_0}}{\sqrt{L_1^2+L_2^2-2L_1L_2\cos(\theta_E+\Delta\theta)}}=\frac{k_s}{I}L_1L_2\sin\theta_E\frac{L_{3_0}}{\sqrt{L_1^2+L_2^2-2L_1L_2\cos\theta_E}}+$$
$$\left[\frac{k_s}{I}L_1L_2\cos\theta_E\frac{L_{3_0}}{\sqrt{L_1^2+L_2^2-2L_1L_2\cos\theta_E}}-\frac{1}{2}\frac{k_s}{I}L_1L_2\sin^2\theta_E\frac{L_{3_0}}{(L_1^2+L_2^2-2L_1L_2\cos\theta_E)^{\frac{3}{2}}}\right]\Delta\theta \quad (3.22)$$

Combining the linear portion of Eq. (3.19) with linearized Eq. (3.21) and Eq. (3.22) produces the full linear differential equation about an operating point. A small angle approximation method will also be used to compare to the Taylor Series and nonlinear differential equation solutions to determine the best linear approximation. Using the small angle approximations

$$\sin\theta\approx\theta;\cos\theta\approx1 \quad (3.23)$$

results in the following linearized differential equation:

$$\ddot{\theta}=\frac{k_l}{I}(\theta_0-\theta)-\frac{k_s}{I}L_1L_2(\theta_0-\theta)\left[1-\frac{L_{3_0}}{\sqrt{L_1^2+L_2^2-2L_1L_2}}\right]. \quad (3.24)$$

Numerical integration Runge-Kutta (Dormand-Prince) implemented by the MATLAB ode45 function was used to evaluate the linear and nonlinear differential equations at small angles at the saddle point and near the center as seen in Figure 3.7 and Figure 3.8.

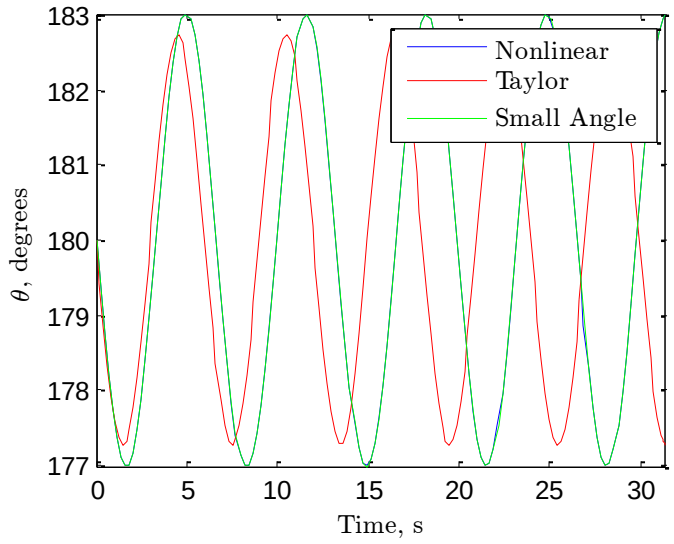

Figure 3.7. Nonlinear and linearized response of the crank-slider differential equation about $\theta_0 = \pi$ radians with all variables at the baseline configuration and $L_1 = 2$.

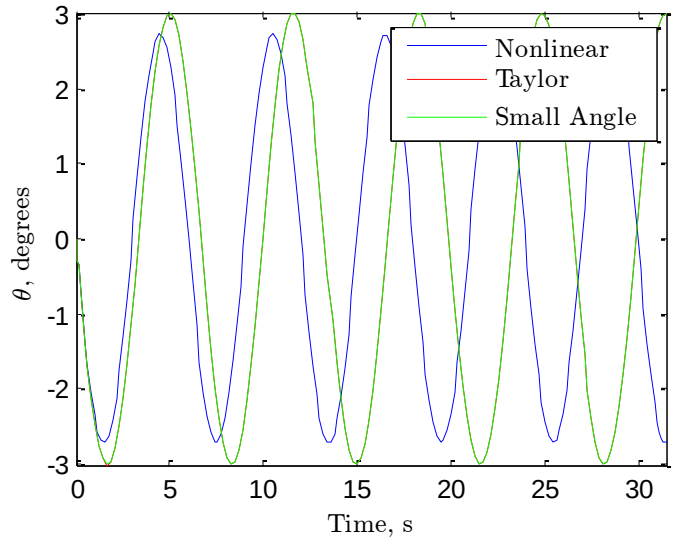

Figure 3.8. Nonlinear and linearized response of the crank-slider about $\theta_0 = 0$ with all variables at the baseline configuration and $L_1 = 2$.

In the case of $\theta_0 = \pi$ radians the nonlinear and small angle solutions overlap completely with the Taylor series solution approximating closely with a small phase lag and a small deviation in magnitude. At $\theta_0 = \pi$ radians the Taylor series and small angle solutions are

identical with similar deviations from the nonlinear response. This verifies that each solution can approximate the nonlinear solution, the eigenvalues of the linearized ODE will be investigated next.

The nonlinear differential equation can be converted to a linear system of differential equations of the form,

$$\begin{bmatrix}\dot{\theta}_1\\ \dot{\theta}_2\end{bmatrix} = [A]\begin{bmatrix}\theta_1\\ \theta_2\end{bmatrix} + [B] \tag{3.25}$$

where matrix A is the coefficients of the independent variables and $\dot{\theta}_1 = \dot{\theta}$ and $\dot{\theta}_2 = \ddot{\theta}$. Solving,

$$\det(A - \lambda I) \tag{3.26}$$

will determine the eigenvalues near the operating point. Calculating the eigenvalues for the system evaluated at $\theta_0 = \frac{12\pi}{13}$ radians, $\omega_0 = 0$ radians/s leads to $\lambda_{1,2} = 0 \pm 0.72j$. As expected, this is an imaginary complex conjugate pair suggesting the equilibrium position is a center node.

Next, examination of the phase portrait response with respect to variation of variables will be conducted. The reason for this investigation is to see the dynamic effects associated with each variable and examine responses and phase portraits for trends. Secondarily, this is done to examine trends in dynamics around equilibrium points. In this analysis, initial condition responses are examined at $\theta_0 = \left[0, \frac{\pi}{3}, \frac{2\pi}{3}, \pi\right]$ radians and $\omega_0 = [0, -0.25, -0.5]$ radians/s. The initial conditions for each response are indicated by a black marker on the phase portrait; this is first seen in Figure 3.9.

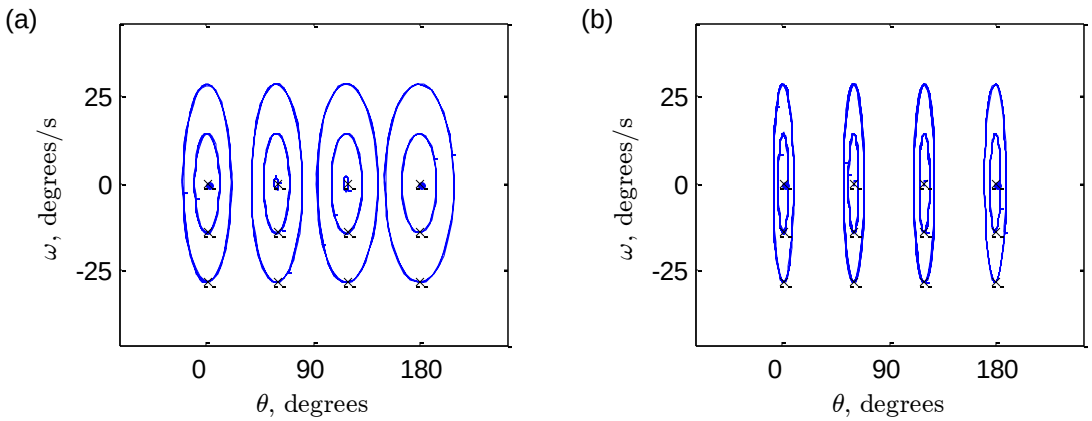

Figure 3.9. Phase portrait response at varying initial conditions: (a) $k_l = 1$ N / m, (b) $k_l = 10$ N / m. All other parameters are one.

In Figure 3.9 the variable k_l is modified from the baseline to the value of 10 (N · m) / rad. As can be seen, the response is oscillatory and has a common response with increasing starting angles. Keeping the starting angle constant, increasing the angular velocity results in a response that oscillates about a larger angle. This is observed in Figure 3.9 (a) and Figure 3.9 (b) as concentric circles. Comparing the phase portrait of $k_l = 1$ to the phase portrait of $k_l = 10$ a reduction in oscillation angle is detected given identical initial conditions. With an increase in spring load the restoring force dominates the system; reducing oscillation angle. It is worth noting that given identical initial conditions there is no reduction in angular velocity. This is on account of the lack of damping in the system.

Increasing the spring constant of the actuator, k_s, shows a comparably different response across different starting angles as seen in Figure 3.10. At the center node, the response shows a markedly different angle of oscillation. The reduced angle of oscillation is caused by the nonlinearity of the mechanism about this operating point. Small changes in angle of the mechanism produce linear changes in length of the load spring and large changes in the length of the actuator; as a result the nonlinear restoring force becomes the dominant effect. Conversely, at $\theta = \pi$ radians, the linear spring becomes the dominant restoring force allowing larger changes in oscillation angle.

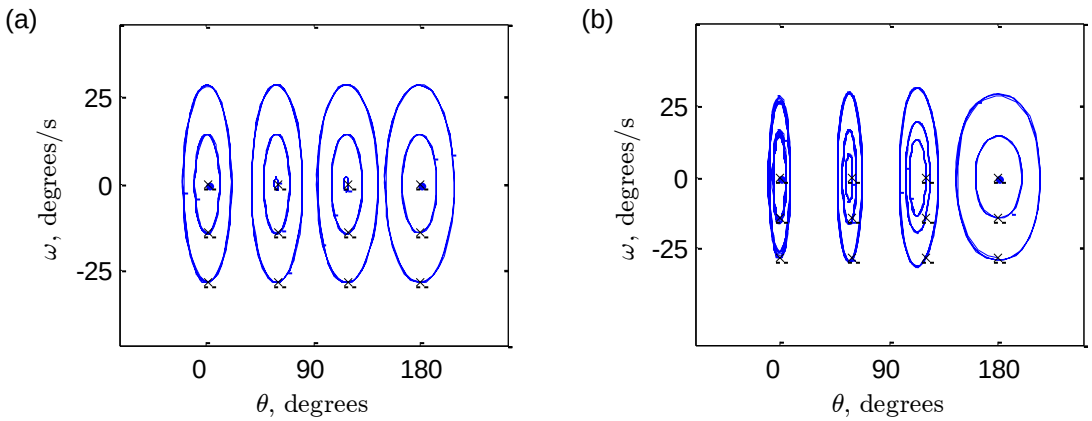

Figure 3.10. Phase portrait response at varying initial conditions: (a) $k_s = 1$ N/m, (b) $k_s = 10$ N/m. All other parameters are one.

When the inertial constant, I, is increased - inertial effects begin to dominate the system as shown in Figure 3.11. The restoring forces are much smaller than the inertial forces and thus act uniformly throughout the motion.

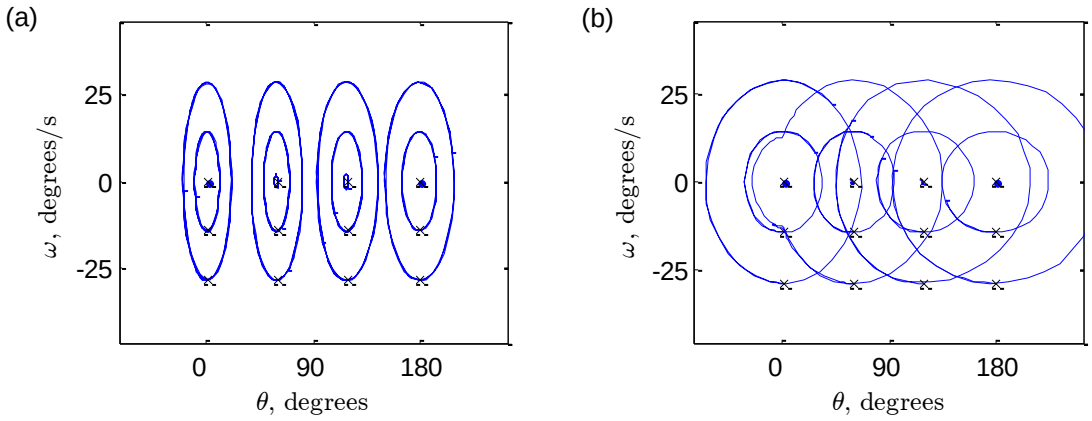

Figure 3.11. Phase portrait response at varying initial conditions: (a) $I = 1\ \mathrm{kg \cdot m^2}$, (b) $I = 10\ \mathrm{kg \cdot m^2}$. All other parameters are one.

The final variable to adjust is the frame length. Increasing frame length has a similar effect as increasing the actuator spring constant. This effect shows larger oscillations at both the center and saddle point. By increasing the frame length the nonlinearity term is amplified. This

can be reasoned by examining the length of the actuator when the frame length is increased. By increasing the frame length, the actuator is scaled by the difference from baseline state. During this condition, the same change in angle produces a larger percent change in the actuator, thus, amplifying the nonlinear effect on the system.

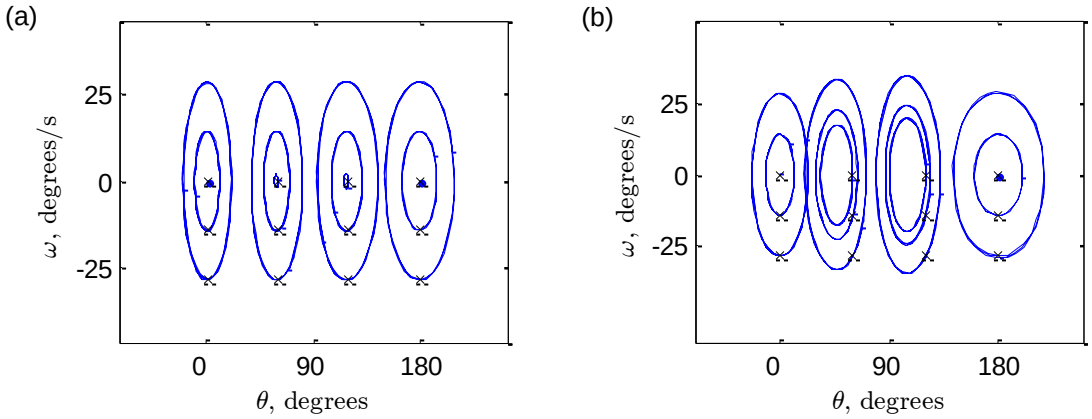

Figure 3.12. Phase portrait response at varying initial conditions: (a) $L_1 = 1$, (b) $L_1 = 10$. All other parameters are one.

Further investigation of the phase portrait as a result of scaling variable values shows very little change at $\theta_0 = 0$ radians. However, increasing the bias load to a very small value or the frame length to a large value, both displayed in Figure 3.13, shows cross-well oscillation at $\theta_0 = \pi$ radians.

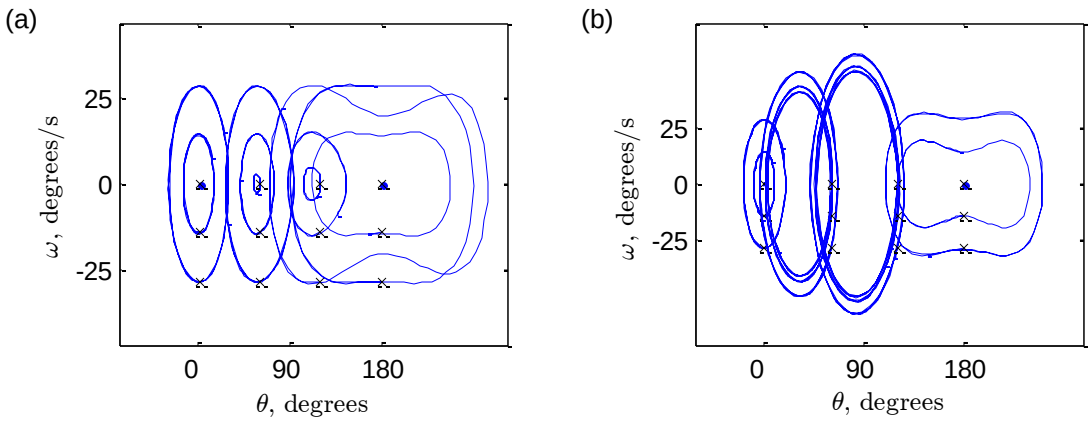

Figure 3.13. Phase portrait response at varying initial condition:. (a) $k_l = 0.01$ N · m/rad, (b) $L_1 = 25$. All other parameters are one.

The eigenvalues for varying the bias spring load and frame length at $\theta_0 = \pi$ radians are shown in Table 3.1. In each instance, around the operating point of $\theta = \pi$ radians the eigenvalues change from being imaginary complex conjugates to real conjugate solutions. This suggests that as the nonlinear term dominates the system the equilibrium point at $\theta = \pi$ radians changes from a center node to a saddle point.

Table 3.1. Eigenvalues and equilibrium points of different parameter mechanisms at $\theta_0 = \pi$ radians.

Variable Value	Eigenvalue	Type	Character
$k_l = 1$ N · m/radians	$0 \pm 0.97j$	Imaginary	Center Node
$k_l = 0.01$ N · m/radians	± 0.2	Real	Saddle Point
$L_1 = 10$	$0 \pm 0.707j$	Imaginary	Center Node
$L_1 = 25$	± 0.5	Real	Saddle Point

Since the transition between a stable node and an unstable node is driven by the real portion of the eigenvalue, zero in the stable case and conjugate real pairs in the unstable, plotting the eigenvalues as the geometric variable changes will show when the equilibrium point shifts from a center node to an unstable node. This is shown in Figure 3.14 for an increasing frame length.

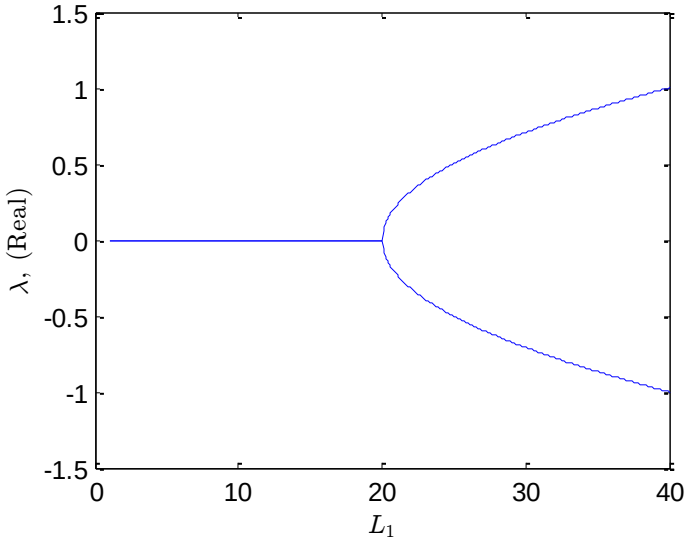

Figure 3.14. Real portion of eigenvalues with increasing frame length at operating point $\theta = \pi$ radians. All other parameters are one.

Since the geometric variables dictate the mechanics of the actuator load and the bias load is isolated from these variables the equilibrium point can be summarized by a stiffness ratio. This is done by taking the coefficients of each portion of the differential equation and examining the real portions as a function of the ratio of the coefficients. The coefficients are chosen as,

$$c_1 = k_l, c_2 = k_s L_1 L_2 \varepsilon \tag{3.18}$$

where ε is the initial percent contraction of the actuator spring. The stiffness ratio (SR) is defined as:

$$SR = \frac{c_2}{c_1} \tag{3.18}$$

It should be noted that the first constant is directly proportional to the load spring constant and inversely proportional to the inertial force. The second term is proportional by the length of the frame and actuator spring constant, inversely proportional to the inertial term, and nonlinearly scaled by frame length. In adjusting the coefficients, the eigenvalues of the differential equation are changed.

Plotting the real portions of the eigenvalues with increasing stiffness ratio produces a similar plot, seen in Figure 3.15. This shows at stiffness ratios greater than one, the actuator

becomes the dominant effect in the dynamics of the system producing a saddle point about $\theta = \pi$ radians.

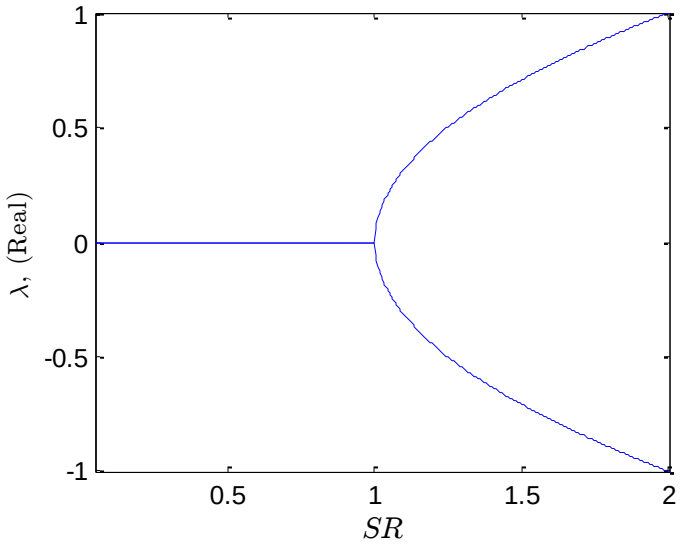

Figure 3.15. Real portion of eigenvalues with respect to stiffness ratio.

Examining the phase portrait response with SR of 0.5 to that of 1.5 shows the differences in response about the same operating point. To note, since stiffness ratio is simply the coefficient of the nonlinear actuator with respect to the linear spring the stiffness ratio can be increased or decreased by any of the independent variables. Therefore, the same geometric mechanism can produce different equilibrium points by simply reducing the bias spring load. The two phase portraits are seen comparatively in Figure 3.16.

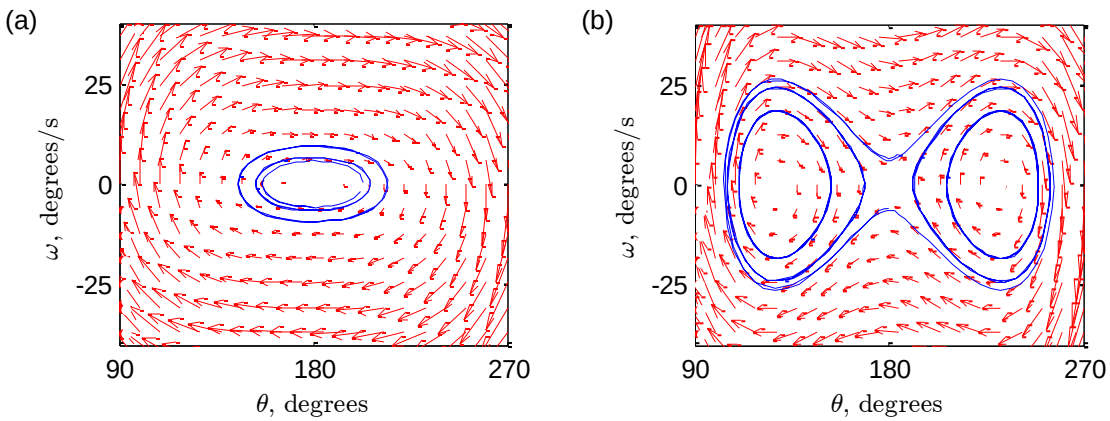

Figure 3.16. Phase portrait response at initial conditions of (a) $SR = 0.5$ and (b) $SR = 1.5$ about operating point of $\theta = \pi$ radians.

It can be seen that for increasing stiffness ratio the equilibrium system oscillates about one node for the center point to two nodes for the saddle point. As the initial conditions move away from the saddle point the response returns to an oscillation about a center node. How these two equilibrium position have effects on damped dynamics will be examined next.

Introducing a viscous damping coefficient, k_d, to the differential equation modifies the state space form to:

$$\dot{\theta}_1 = \theta_2 = \omega \tag{3.27}$$

$$\dot{\theta}_2 = \frac{k_l}{I}(\theta_0 - \theta_1) - k_d\theta_2 - \frac{k_s}{I}L_1L_2\sin\theta_1\left[1 - L_{3_0}/L_3\right] \tag{3.28}$$

Damped free response analysis is of interest to this thesis for a better understanding of the energy dissipation around equilibrium points. Examining the free response around the center node, seen in Figure 3.17 (a), shows the damped free response with an initial angular velocity of $\omega = -0.5$ radians/s. The mechanism is at the baseline state with $L_1 = 2$ and $k_d = 0.5\,\mathrm{N}\cdot\mathrm{m}\cdot\mathrm{s}/\mathrm{radians}$. The plot indicates the initial condition with a "circle" marker and additional markers of maximum kinetic energy, "x", and maximum potential energy, marked by a "diamond". The graph shows maximum kinetic energy occurring at the initial conditions and potential energy maximizing as the mechanism moves passed the x-axis. These two phenomena always occur in a damped system around the center node. As the mechanism is in

motion, energy is lost due to the damping effects on the system. This is easily seen by inspection of the time response as shown in Figure 3.17 (b). As the mechanism oscillate around the equilibrium point the magnitude of the oscillation steadily decreases, thus, decreasing the total energy in the system. The color spectrum indicates maximum potential energy, in red, to minimum potential energy, in blue.

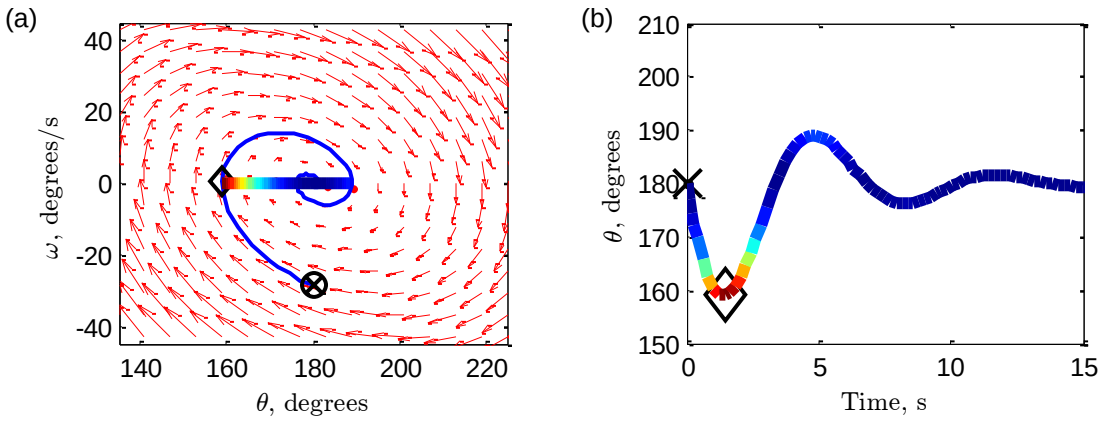

Figure 3.17. (a) Phase portrait plot of the free response of a damped system at the center node with initial condition: $L_1 = 2$. All other parameters are equal to one. (b) The time response of the system position. The triangle marker indicates maximum potential energy and x-marker for maximum kinetic energy.

The phase portrait plot for the free response of a damped system will always have the maximum kinetic energy at positions of highest magnitude on the y-axis and maximum potential energy highest on the x-axis. Around center-nodes, with initial position at equilibrium, the energy will dissipate and the system will "fall" into the potential energy well.

Analysis of the saddle point damped free response, Figure 3.18, shows the existence of two potential energy wells. In both analysis the mechanism has a SR equal to two with a starting angle of $\theta = \pi$ rad. Between the two plots the only difference is the value of the damping coefficient of $k_d = 0.25\ \mathrm{N \cdot m \cdot s/radians}$ in Figure 3.18 (a) and $k_d = 0.5\ \mathrm{N \cdot m \cdot s/}$ radians in Figure 3.18 (b).

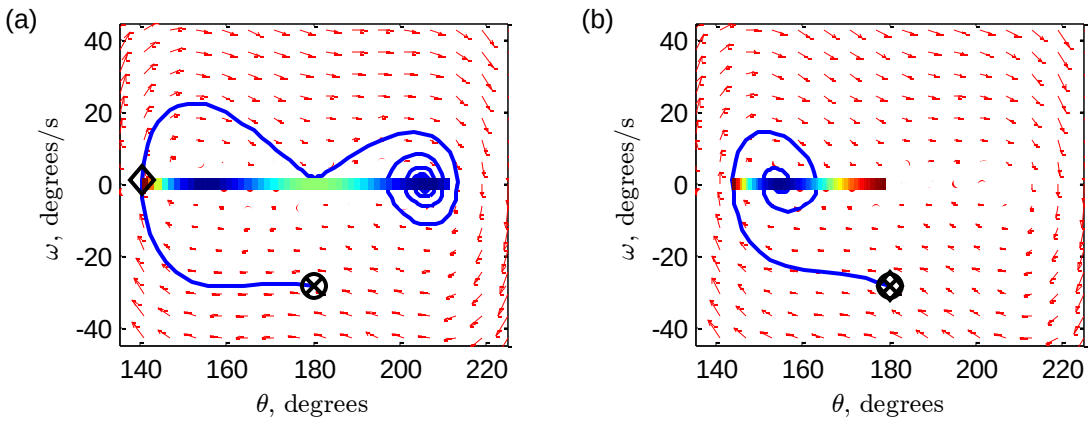

Figure 3.18. Damped free responses around the saddle equilibrium point with $SR = 2$ and $\theta_0 = \pi$ rad. The damping coefficient, k_d, is equal to: (a) 0.25 $\mathrm{N \cdot m \cdot s/rad}$ and (b) 0.5 $\mathrm{N \cdot m \cdot s/rad}$.

This phenomena of the tendency of the mechanism to move into a potential energy well is reasoned through energy analysis. In the lower damping coefficient case, the initial kinetic energy moves the mechanism to its peak potential energy, losing a small amount of energy on the way. Though a small amount of energy loss incurs, there is enough potential energy converted to kinetic to move it passed the unstable equilibrium position. Once passed, the energy loss is too high and it oscillates into the potential energy well. This energy loss phenomenon is confirmed by increasing the damping coefficient, Figure 3.18 (b). By increasing the energy loss in the first pass, the mechanism does not have enough energy to move past the equilibrium position and falls into the potential energy well to the left of the saddle point. This bifurcation behavior is characteristic of a saddle point.

The saddle point bifurcation can be demonstrated by plotting the damped free response with initial conditions of $\theta_0 = \pi$ radians and $\omega_0 = 0$ radians and $SR = 2$. With zero initial starting velocity there is no tendency for the mechanism to move in either direction. The stresses within the actuator cause the mechanism to move to one of the two potential energy wells. This can be seen in Figure 3.19. The maximum potential energy occurs at the equilibrium point, maximum kinetic energy at first pass, then the mechanism moves into the potential energy well.

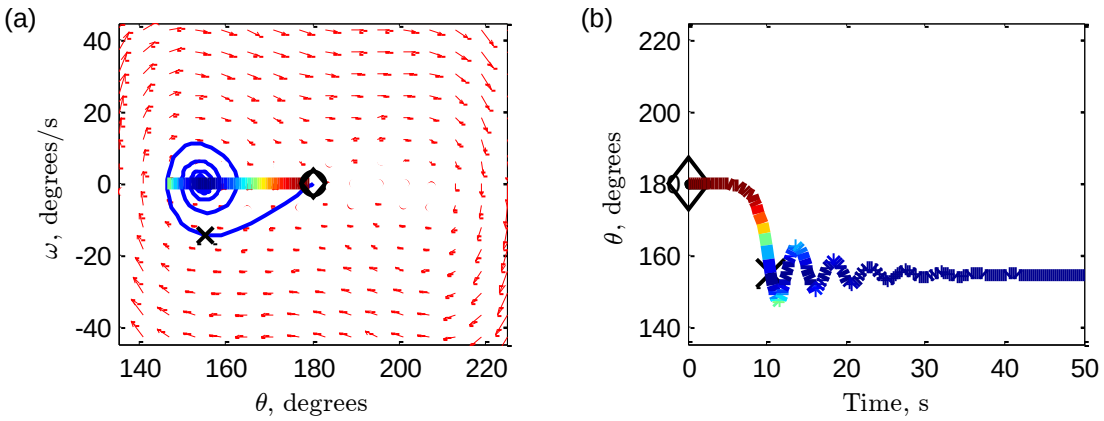

Figure 3.19. Damped free response indicating bifurcation behavior with initial conditions at the saddle point. [$\theta_0 = 0$ radians, $\omega_0 = 0$ radians/s , $SR = 2$]

3.4. Conclusions

The dynamic equations for a crank-slider mechanism given a linear actuator curve are derived using two methods. Both the Lagrangian and Newton's method produce the same equation of motion for the system. Phase portrait analysis is introduced and the effects of the eigenvalues of the differential equation are described. Based on the qualitative analysis of the phase portraits and the eigenvalues a center node and a saddle point are discovered. Phase portrait analysis around these equilibrium points confirms the expected characteristics of these equilibrium points and shows the stable and unstable behavior of both. Introduction of damping effects and energy analysis reveals potential energy wells existing around both equilibrium points. The potential energy well at the center node shows the tendency of the mechanism under any damping to settle at the center node. Adversely, the potential energy wells at the saddle point show bifurcation behavior and the tendency to move to either one is dependent on the energy in the system and the damping coefficient. Bifurcation behavior at the saddle point is verified by showing a zero initial condition response with initial conditions at the saddle point.

CHAPTER 4

HEAT TRANSFER BEHAVIOR

4.1. Introduction

The objective of this chapter is to investigate the stress-strain-temperature diagram of shape memory alloy and examine its effects on actuation. Following this investigation, a heat transfer model is proposed for the SMA wire. A differential equation is developed and modified dependent on temperature of the wire. The solution is examined at each crystallographic phase and examined for dominant heat transfer effects. After the analytical analysis, theoretical identification is done for unknown heat transfer terms for the wire using an experimental test bed.

4.2. Material Behavior

It was introduced in chapter 2 that an SMA wire has two homogenous crystallographic states, martensite and austenite. These two states play an integral role in the thermo-mechanical phenomena of the pseudo-elastic effect and the shape memory effect. Both of these phenomena are responsible for the popularization of this material in various applications. First, the pseudo-elasticity will be examined.

Figure 4.1 is a comparative view of the stress-strain-temperature diagram with the different crystallographic phases for a shape memory alloy wire. The pseudo-elastic effect occurs at the austenite final temperature, T_{A_f}. It is an effect that allows the shape memory alloy to recover from strains of up to 10% of the total length. Assuming the material begins in the detwinned martensite state (1'), the material must be heated to the austenite final temperature, T_{A_f}. This transforms the crystallographic structure from detwinned martensite (1') to austenite (2). The pseudo-elastic effect occurs at this stage with an application of stress through an isothermal process. As stress builds in the wire, the stress converts the austenite structure to

martensite. At maximum stress, the shape memory alloy wire is in a complete martensite phase; known as stress induced martensite (3). Through this loading process strains of up to 10% of overall length have been measured. On removal of stress the martensite returns to austenite and the full strain is recovered. It should be noted that this is a hysteretic process; meaning the removal of stress follows a different path from the application of stress. This difference in stress-strain behavior along the isotherm is due to the additional energy required to convert the austenite to martensite, in this case through stress, where it is unnecessary in the reverse process. This is an important property of a shape memory alloy but is not applicable in actuation; therefore the rest of the thesis will focus on the shape memory effect.

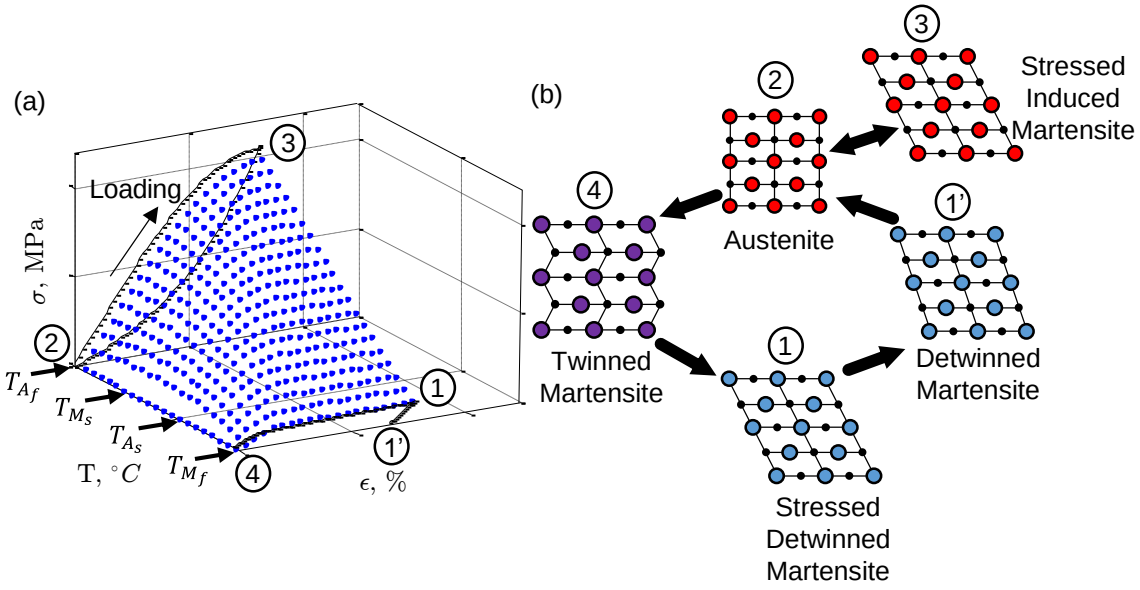

Figure 4.1. (a) Stress-strain-temperature diagram with (b) corresponding crystallographic properties.

The shape memory effect is an effect that, through a thermo-mechanical cycle, the wire can move between two stable states with differing mechanical properties. The first state, arbitrarily chosen as state one, is the detwinned martensite state (1'); stable at the temperature T_{M_f}. This state is characterized by a low modulus of elasticity and low yield strength. It is more elastic than its counterpart and has a longer free length. When heated, in a zero-stress condition, the crystallographic structure is complete martensite until the austenite start temperature, T_{A_s}.

At this point the crystallographic structure begins to convert nonlinearly into austenite until the austenite final temperature, T_{A_f}; where the crystallographic structure is pure austenite (2). These two states are mathematically represented by the martensite fraction, (ξ). At complete martensite phase the martensite fraction is $\xi = 1$ and at austenite phase the martensite fraction is $\xi = 0$. The austenite state is characterized by having a shorter free length, much higher modulus and yield strength, and being more brittle. Due to these differences in mechanical properties, it is possible to convert thermal energy into mechanical work, and thus leading to a practical actuator. On stress-free cooling the process reverses. From the austenite final temperature, the wire cools until the martensite start temperature, T_{M_s}, where austenite converts into martensite nonlinearly until the martensite final temperature, T_{M_f}. At the martensite final temperature the material is in the twinned martensite phase (4). This phase has similar characteristics to the detwinned martensite phase but with a reduction in strain. To recover this strain, stress must be applied. At the martensite yield strength the material is in stressed detwinned martensite phase (1). Upon relaxation, the material finally returns to detwinned martensite (1').

4.3. Heat Transfer Model

The transient heat transfer model makes the following assumptions: the size of the diameter of the cylinder is small compared to the length; therefore the temperature distribution is uniform throughout the cross section of the wire, and the length of the wire is infinitely long. The dominant energy contributions in the heat transfer model are illustrated in Figure 4.2.

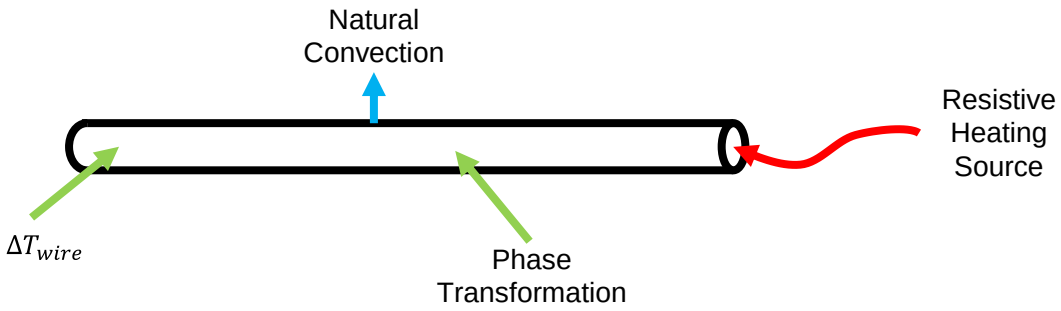

Figure 4.2. Heat transfer effects on an SMA wire undergoing joule heating.

The energy balance of the control volume can be mathematically represented by the differential equation:

$$\frac{dE}{dt} = \frac{dq}{dt} \tag{4.1}$$

which shows the relation of the rate of heat transfer through the control volume (q) to the rate of stored energy of the system (E). The heat transfer contributions are heat generation and heat loss, these are resistive heating and natural convection respectively. The sources for energy storage in the system are internal energy and phase transformation energy. Conservation of energy gives:

$$mc_p \frac{dT}{dt} - m\Delta h \frac{d\xi}{dt} = hA_s(T_\infty - T_s) + I^2R. \tag{4.2}$$

Resistive heating is achieved by the current through the wire and is governed by Ohm's Law. Internal energy of the wire is measured as the change in temperature multiplied by the mass and specific heat of the material. Phase transformation from martensite to austenite is represented similarly but with a heat transformation constant. The negative sign in this term, is due to the change in martensite fraction being negative when changing from martensite to austenite. Finally, the well-known heat convection equation describes heat losses due to the difference between the temperature of the ambient medium and the surface temperature of the wire.

Not all of these effects are always active. To investigate these effects they will be examined over the process of the shape memory effect. To begin the wire is assumed to be in

the martensite detwinned phase at ambient temperature. At the start of heat generation the heat transfer is governed by only convection, internal energy, and generation. This is because no phase transformation occurs until the austenite start temperature. The phase transformation term is present until austenite final temperature where it drops for temperatures above T_{A_f}. On cooling, the generation term is removed with only the transformation term being present between the martensite start and martensite final temperatures.

It is of interest to this thesis to examine the energy during each of these phases to understand the dominant terms. To describe the change in martensite fraction, Shahin et al.[26], empirically based cosine shaped zero stress transformation equation of the form for martensite to austenite transformation,

$$\xi = \frac{1}{2}\left[1 + \cos\pi\left(\frac{T - T_{A_S}}{T_{A_f} - T_{A_S}}\right)\right] \tag{4.3}$$

with a rate equation of

$$\frac{\pi}{2\left(T_{A_f} - T_{A_S}\right)}\left[sin\,\pi\left(\frac{T - T_{A_S}}{T_{A_f} - T_{A_S}}\right)\right]\frac{dT}{dt} \tag{4.4}$$

and for austenite to martensite transformation,

$$\xi = \frac{1}{2}\left[1 + \cos\pi\left(\frac{T - T_{M_f}}{T_{M_S} - T_{M_f}}\right)\right] \tag{4.5}$$

with a rate equation of

$$\frac{\pi}{2\left(T_{M_S} - T_{M_f}\right)}\left[sin\,\pi\left(\frac{T - T_{M_f}}{T_{M_S} - T_{M_f}}\right)\right]\frac{dT}{dt}. \tag{4.6}$$

A summary of all heat transfer governing equations of the shape memory effect with zero stress are shown in Table 4.1.

Table 4.1. Differential equations for different stages of shape memory effect.

Equation	Conditions
$mc_p \frac{dT}{dt} = hA_s(T_\infty - T_s) + I^2R$	Heating: $T_{A_f} < T < T_{A_s}$
$mc_p \frac{dT}{dt} + \frac{\pi m \Delta h}{2\left(T_{A_f} - T_{A_s}\right)}\left[sin\,\pi\left(\frac{T - T_{A_s}}{T_{A_f} - T_{A_s}}\right)\right]\frac{dT}{dt} = hA_s(T_\infty - T_s) + I^2R$	$T_{A_f} > T > T_{A_s}$
$mc_p \frac{dT}{dt} = hA_s(T_\infty - T_s)$	Cooling: $T_{M_s} < T < T_{M_f}$
$mc_p \frac{dT}{dt} + \frac{\pi m \Delta h}{2\left(T_{M_s} - T_{M_f}\right)}\left[\sin\pi\left(\frac{T - T_{M_f}}{T_{M_s} - T_{M_f}}\right)\right]\frac{dT}{dt} = hA_s(T_{amb} - T)$	$T_{M_s} > T > T_{M_f}$

In the evaluation of the heat transfer equations the constants defined in Table 4.2 are used. The resistance value is based on initial measurements of the wire resistance using a multi-meter. The value of specific heat, latent heat of transformation, and phase transformation temperatures are borrowed from Shahin et al. [26].

Table 4.2. List of constants used for heat transfer analysis.

Constant	Value	Source
Diameter	250 µm	[27]
Length	115 mm	Measured
ρ	6.45 g/cm^3	[27]
c_p	250 J/kg · K	[26]
T_∞	23 °C	Measured
Resistance	2.5 Ω	Measured
Δh	30000 J/kg	[26]
T_{A_s}	55 °C	[26]
T_{A_f}	70 °C	[26]
T_{M_s}	50 °C	[26]
T_{M_f}	25 °C	[26]

Using the Runge-Kutta (Dormund-Prince) numerical integration method implemented by MATLAB's ode45 function the differential equation for heat transfer before and after transformation is evaluated. The two cases, chosen for demonstrative purposes, are the $T_0 = T_\infty$ driven at 0.85 A, and $T_0 = T_{A_f}$ with a current of 1.2 A. The results are seen in Figure 4.3 and Figure 4.4. Of interest in Figure 4.3 is the small contribution of energy into temperature change of the material. At temperatures close to ambient, a majority of the Joule heating goes into internal energy. After this is complete, all additional energy is directly converted to losses due to the difference of the ambient and surface temperature. This is further seen in the post-austenite final temperature case. Nearly all of the energy is lost due to the convective heat transfer.

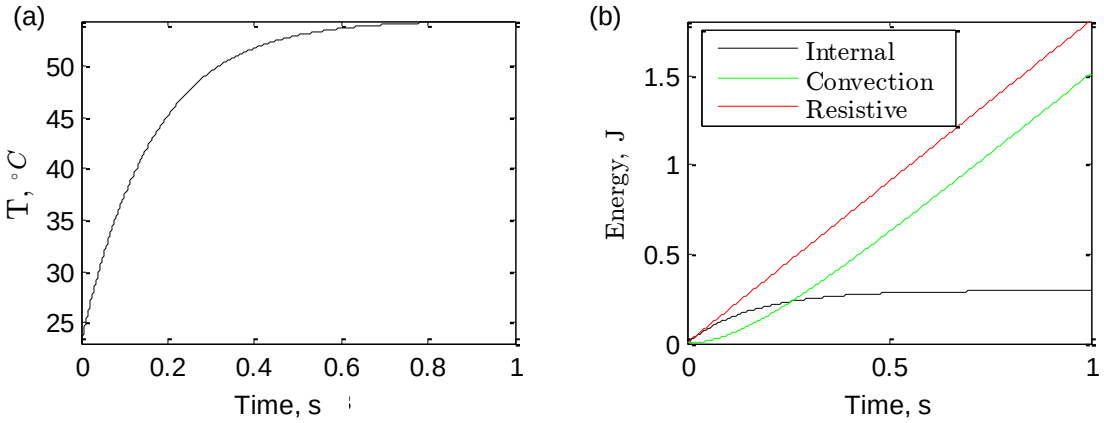

Figure 4.3. (a) Temperature response and (b) energy plot of resistive heating at 0.85 A.

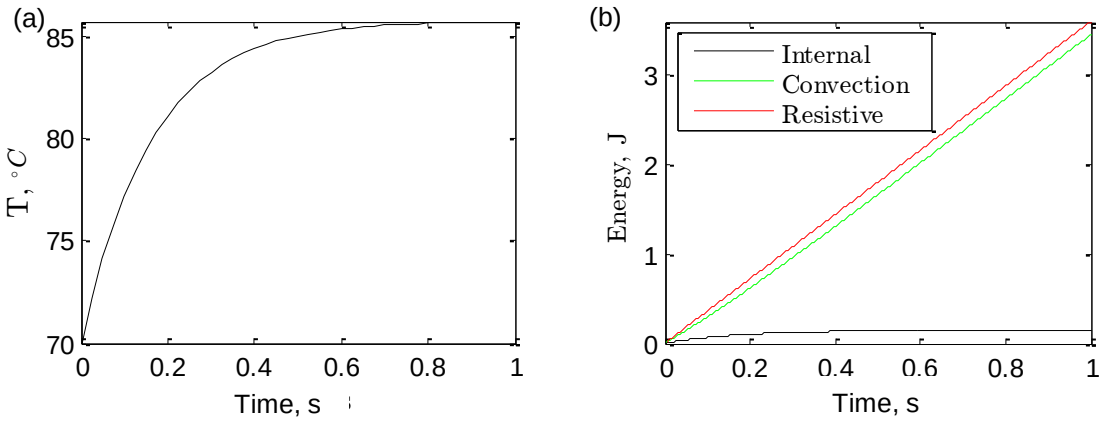

Figure 4.4. (a) Temperature response and (b) energy plot of resistive heating at 1.2 A.

Inspecting the martensite to austenite transient response and energy plots, Figure 4.5, it can be seen that convection is the dominant energy throughout the process with less effect at lower temperatures. The phase transformation kinetic also consumes much more energy than increasing the internal energy.

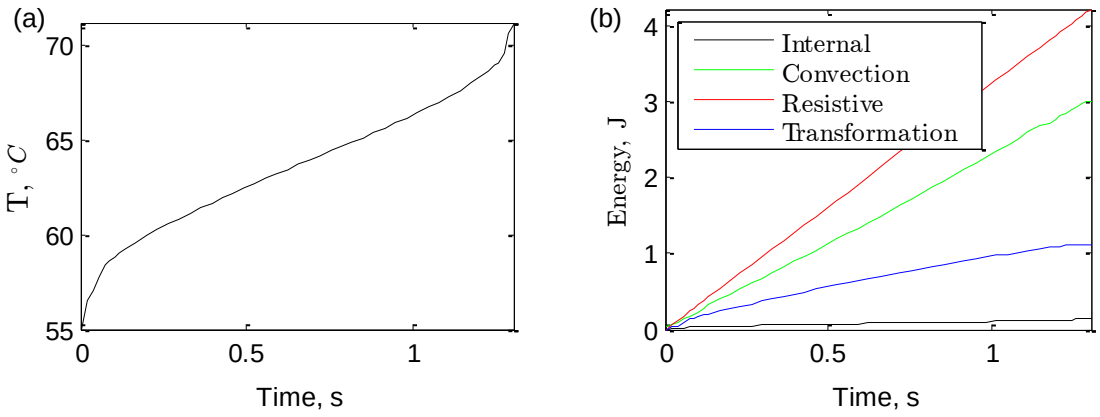

Figure 4.5. (a) Temperature response and (b) energy plot of phase transformation from martensite to austenite with resistive heating of 1.3 A.

On cooling, a simple equal relationship of internal energy loss to convective effects is shown in Figure 4.6.

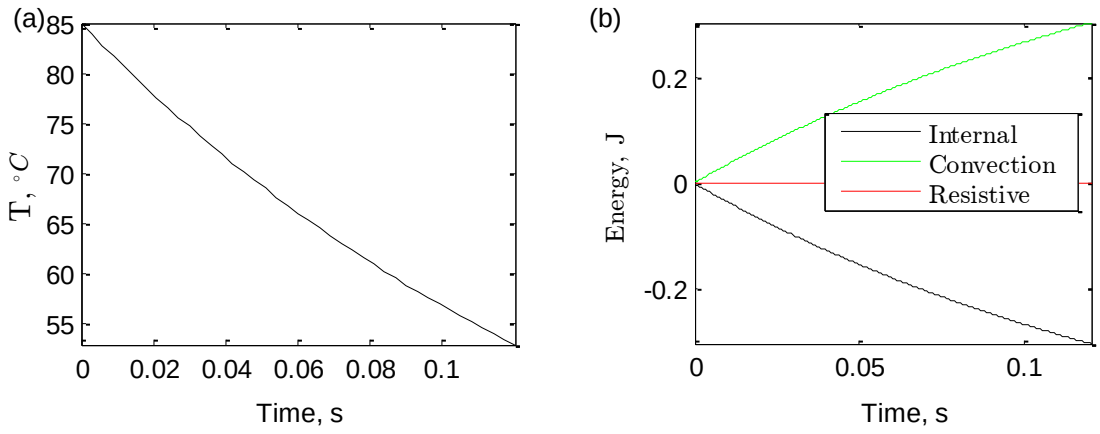

Figure 4.6.(a) Temperature response and (b) energy plot for cooling above martensite start temperature.

Lastly, austenite to martensite cooling plots, Figure 4.7, shows the dominant transformation contribution to convection energy losses.

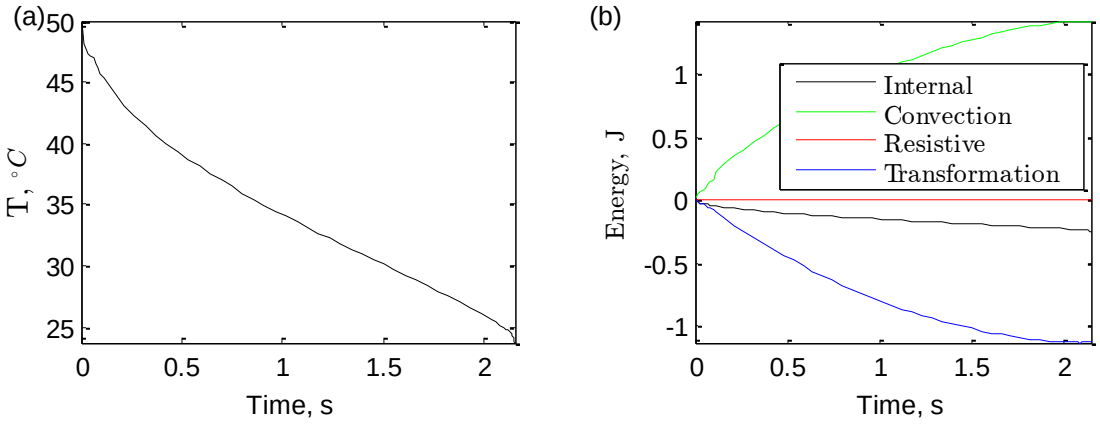

Figure 4.7. (a) Transient response and (b) energy plot for phase transformation for cooling from austenite to martensite.

4.4. System Identification

To fully develop the heat transfer model the model parameters must be experimentally determined. During theoretical analysis, the model parameters of specific heat (c_p), heat transfer coefficient (h), and resistance were estimated based on measurements from Shahin et

al. [26]. SMA wire properties of specific heat and resistance are unique to the manufacturer and the heat convection coefficient is unique to the test bed. By examining the heat transfer model and eliminating terms based on transient and steady state responses it is possible to isolate individual coefficients and conduct experiments to measure for each parameter. The theoretical derivation to experimentally determine these parameters will be described in the first portion of this section.

4.4.1. Resistance, *R*

Resistance in the wire is found by employing Ohm's Law. Ohm's Law governs the relationship of voltage, current, and resistance in a circuit. The well-known equation for Ohm's Law is:

$$V = IR \tag{4.7}$$

Rearranging the equation provides the relationship:

$$R = \frac{I}{V} \tag{4.8}$$

By experimentally applying increasing voltages while measuring current, then plotting current as a function of voltage, will result in a slope of a line. This linear relationship is the resistance of the wire.

4.4.2. Heat Transfer Coefficient, *h*

The heat transfer coefficient is found through examination of the heat transfer differential equation:

$$mc_p \frac{dT}{dt} - m\Delta h \frac{d\xi}{dt} = hA_s(T_\infty - T_s) + I^2R \tag{4.9}$$

At steady state, the transient terms for phase transformation and internal energy reduce to zero. This leaves a simple equation relating the convection coefficient as a function of the current.

$$h = \frac{I^2 R}{A_s(T - T_{amb})} \tag{4.10}$$

4.4.3. Specific Heat, c_p

Recalling from Eq. (4.2), prior to phase transformation only internal energy, resistive heating, and convection govern the differential equation:

$$mc_p \frac{dT}{dt} = hA_s(T_\infty - T_s) + I^2 R. \tag{4.11}$$

When transformation temperatures and the heat transfer coefficients are known the following analysis can determine the specific heat of the wire. Integrating (4.11) over time produces:

$$mc_p \int_{t_0}^{t_f} \frac{dT}{dt} dt = hA_s T_\infty \int_{t_0}^{t_f} dt - hA_s \int_{t_0}^{t_f} T(t)\, dt + \int_{t_0}^{t_f} I^2 R\, dt \tag{4.12}$$

Since the rate of change in temperature cannot be measured directly due to measurement delay in the thermocouples of the experimental test bed, the integral limits are changed to measure the entire energy prior to the beginning of phase transformation,

$$mc_p \int_{T_0}^{T_f} dT = hA_s T_\infty (t_f - t_0) - hA_s \int_{t_0}^{t_f} T(t)\, dt + I^2 R(t_f - t_0) \tag{4.13}$$

finishing the modified definite integrals leads to,

$$mc_p(T_f - T_0) = hA_s T_\infty (t_f - t_0) - hA_s \left[\int T(t) dt\right]_{t_0}^{t_f} + I^2 R(t_f - t_0). \tag{4.14}$$

Now, an assumption is made that the temperature response is an exponential function,

$$T(t) = Ke^{-\frac{1}{a}t} + b;\ \ where, b = T_f, k = T_0 - Tf\ , a = \frac{t_f}{2.2}. \tag{4.15}$$

Integrating the temperature function leads to,

$$-Ka\left[e^{-\frac{t}{a}}\right]_{t_0}^{t_f} + b(t_f - t_0) \tag{4.16}$$

Since initial start time is arbitrary, to simplify, it is chosen to be zero, leading to the simplification:

$$hA_s\left[\int T(t)dt\right]_{t_0}^{t_f} = -Kae^{-\frac{t_f}{a}} + Ka + b\left(t_f - t_0\right). \tag{4.17}$$

Substituting the definite integral from equation Eq. (4.17) into Eq. (4.14) and applying zero start time leads to,

$$mc_p\left(T_f - T_0\right) = hA_s\left[\left(T_\infty - T_f\right) - \frac{1}{2.2}\left(T_0 - T_f\right)\left(1 - e^{-2.2}\right)\right]t_f + I^2Rt_f. \tag{4.18}$$

Knowing the ambient temperature and austenite start temperature an experiment can be designed to step current to a specific value and measure the time between step and mechanical response. This difference in temperature and time can be measured, thus, solving for all unknown values in the definite integral. Solving for the specific heat is simply:

$$c_p = \frac{hA_s}{m\Delta T}\left[\left(T_\infty - T_f\right) - \frac{1}{2.2}\left(T_0 - T_f\right)\left(1 - e^{-2.2}\right)\right]\Delta t + \frac{I^2R\Delta t}{m\Delta T} \tag{4.19}$$

A second method can be used to calculate the specific heat by estimating the time and temperature differential of the governing equation,

$$c_p = \frac{1}{m}\left[hA_s(T_\infty - T_s) + I^2R\right]\frac{\Delta t}{\Delta T} \tag{4.20}$$

Both methods will be used for comparison in calculating the specific heat.

4.4.4. Latent Heat of Transformation, Δh

For latent heat of transformation the total heat transfer equation is examined:

$$mc_p\frac{dT}{dt} - m\Delta h\frac{d\xi}{dt} = hA_s(T_\infty - T_s) + I^2R \tag{4.21}$$

A similar integral method can be used for determining the transformation energy. Integrating equation (4.9) leads to:

$$mc_p\int_{t_0}^{t_f}\frac{dT}{dt}dt - \int_{t_0}^{t_f}m\Delta h\frac{d\xi}{dt}dt = hA_sT_\infty\int_{t_0}^{t_f}dt - hA_s\int_{t_0}^{t_f}T(t)\,dt + \int_{t_0}^{t_f}I^2R\,dt. \tag{4.22}$$

Changing integration variables between beginning and end of phase transformation leads to:

$$mc_p \int_{T_0}^{T_f} dT - m\Delta h \int_{\xi_0}^{\xi_f} d\xi = hA_s T_\infty \int_{t_0}^{t_f} dt - hA_s \int_{t_0}^{t_f} T(t)\, dt + \int_{t_0}^{t_f} I^2 R\, dt \qquad (4.23)$$

Knowing the limits of temperature and phase transformation based on mechanical response leads to:

$$mc_p(T_f - T_0) + m\Delta h = hA_s T_\infty (t_f - t_0) - hA_s \int_{t_0}^{t_f} T(t)\, dt + I^2 R(t_f - t_0). \qquad (4.24)$$

The transformation constant becomes

$$\Delta h = \frac{hA_s}{m}\left[(T_\infty - T_f) - \frac{1}{2.2}(T_0 - T_f)(1 - e^{-2.2})\right] t_f + \frac{I^2 R t_f}{m} - c_p(T_f - T_0). \qquad (4.25)$$

4.5. Experimental Setup

All experiments for the system identification of the heat transfer model of the shape memory alloy wire are performed on the wire test bed shown in Figure 4.8. The wire is held in place by two micro drill-chucks located on the top and bottom frame of the test bed. The test bed is balanced through a shaft and fulcrum assembly with the point of the fulcrum on a parallel plane with the top micro drill-chuck. This is done in an attempt to negate geometric effects due to the frame. The displacement sensor and the load cell were calibrated in LabVIEW and verified using calipers and laboratory weights respectively. A positive and negative lead are used for Joule heating. These leads are attached to the micro drill-chuck and are electrically isolated from the frame.

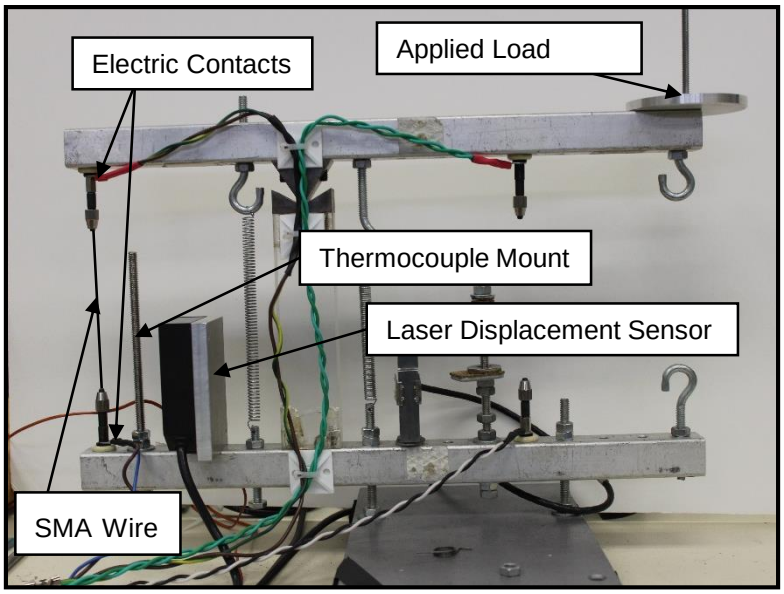

Figure 4.8. Experimental test bed for the system identification of the heat transfer model.

The experiment parameters are defined in LabVIEW and experiment data is recorded using a Nation Instruments data acquisition device (NI cDAQ 9178). For Joule heating, the LabVIEW experiment prescribes a voltage to the analog output card of the data acquisition device. The voltage signal is buffered with a KEPCO Bi-operational amplifier. The amplifier monitors the current and the voltage outputs. Load cell and laser displacement data are also measured through the data acquisition system during testing. The load cell, laser displacement, and current monitoring channels are all recorded at a frequency of 2000 Hz. On a separate channel, two Omega K-type thermocouples are monitored, one for wire surface temperature and one for ambient temperature. The thermocouple is sampled at 2 Hz. All experimental data is recorded in LabVIEW where it is post-processed in MATLAB. This information flow can be seen in Figure 4.9.

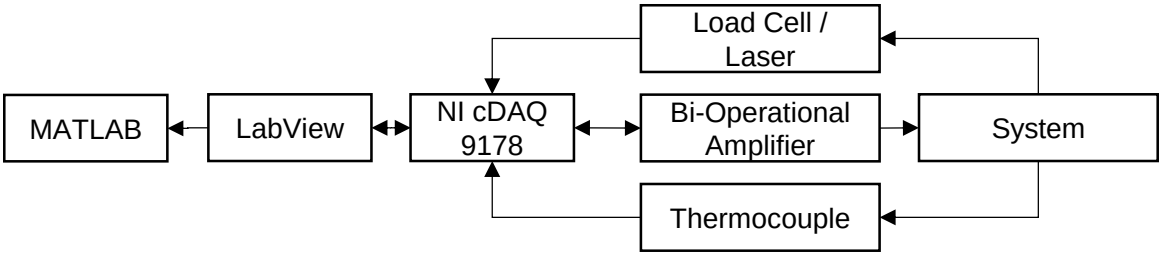

Figure 4.9. Information flow of wire test bed.

4.6. Results

4.6.1. Resistance, *R*

For determination of the resistance, transformation temperatures, and heat transfer coefficient, a 250 μm (0.01″) diameter Nitinol shape memory alloy wire manufactured by Dynalloy is used. A 125 mm length section of wire is placed and secured in the top and bottom micro drill-chucks. The frame is balanced by adding experimental weights to the loading spindle so the wire is in a zero stress condition. The exposed length of the wire is 114 mm. A test is designed with an increasing voltage signal starting from 0 V to a maximum of 2.75 V; the voltage steps were increased by 0.05 V. After each step, the system is allowed to stabilize for 60 seconds and then the steady-state response is recorded over 15 seconds and averaged. At peak voltage the test is reversed, stepping down from 2.75V to 0 V at steps of 0.05 V to look for hysteresis effects in the wire. Examining the slope of the steady state current versus voltage gives the resistance in the wire; results of the experiment for current versus voltage are seen in Figure 4.10.

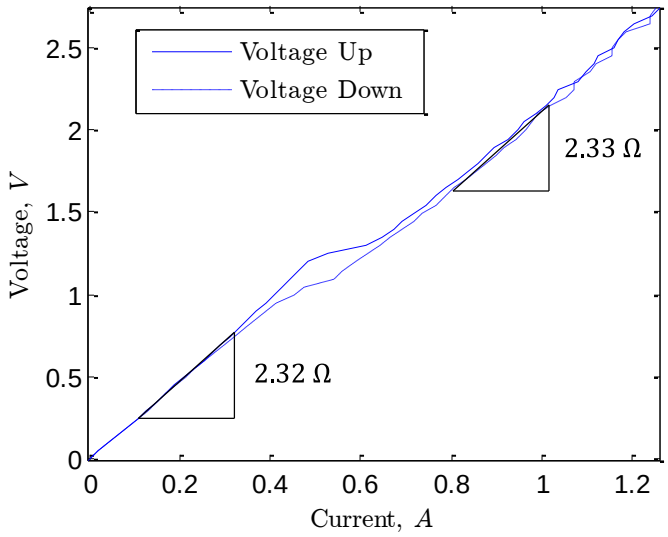

Figure 4.10. Voltage versus current for voltage step from 0 to 2.75 V at steps of 0.05 V.

The increasing and decreasing slopes at low voltages are identical. The resistance at lower voltages was determined to be 2.32 Ω. Calculating the slope at higher voltages, likewise, gives 2.33 Ω. The difference is within tolerances and can be considered a constant resistance throughout the operating temperature range. The apparent resistance experiences hysteresis in the 0.4 A to 0.6 A current range. This is due to transformation in the wire geometry; where length is reduced and diameter slightly increases in the voltage sweep up. This is less prominent on the step down voltages as the length in the wire in the twinned martensite phase must be returned by an application of stress.

4.6.2. Transformation Temperatures: T_{A_s}, T_{A_f}

Examining the temperature versus displacement plot, Figure 4.11, under identical experiment conditions, there are two changes in mechanical length of the wire during voltage increase. The first change is shortly after the start of the experiment. This indicates when the wire first begins changing from martensite to austenite and was found to be 26 °C. When the wire concludes contraction, identifies the austenite final temperature and was found to be 60 °C.

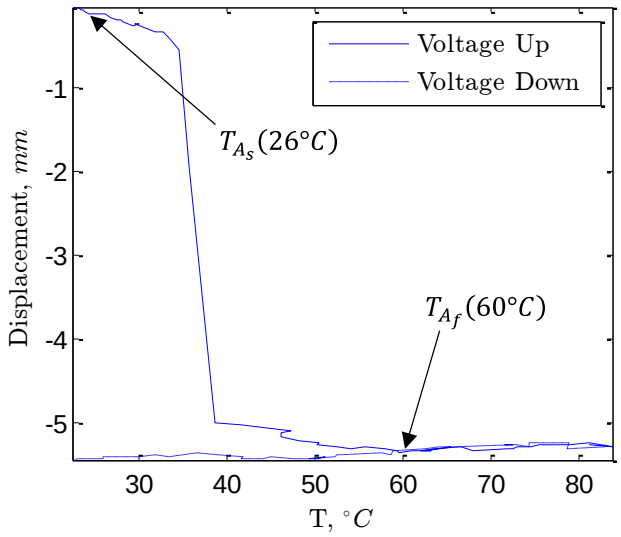

Figure 4.11. Displacement versus temperature for 0 to 2.75 V with steps of 0.05 V.

4.6.3. Convection Coefficient, *h*

To calculate the heat transfer coefficient the steady-state temperature response of current versus temperature is plotted. Recalling the heat transfer coefficient relationship,

$$h = \frac{I^2 R}{A_s(T - T_{amb})} \tag{4.10}$$

and solving for temperature results in

$$T = T_{amb} + \frac{I^2 R}{h A_s}. \tag{4.26}$$

Fitting this function with varying heat transfer coefficients to the experimental data finds the heat transfer coefficient to be $625\ \mathrm{W/m^2 \cdot K}$. It is worth noting that the temperature is a proportional to the current squared. This is also plotted to get a better fit of the data throughout the temperature range. The experimental results combined with the model results are shown in Figure 4.12.

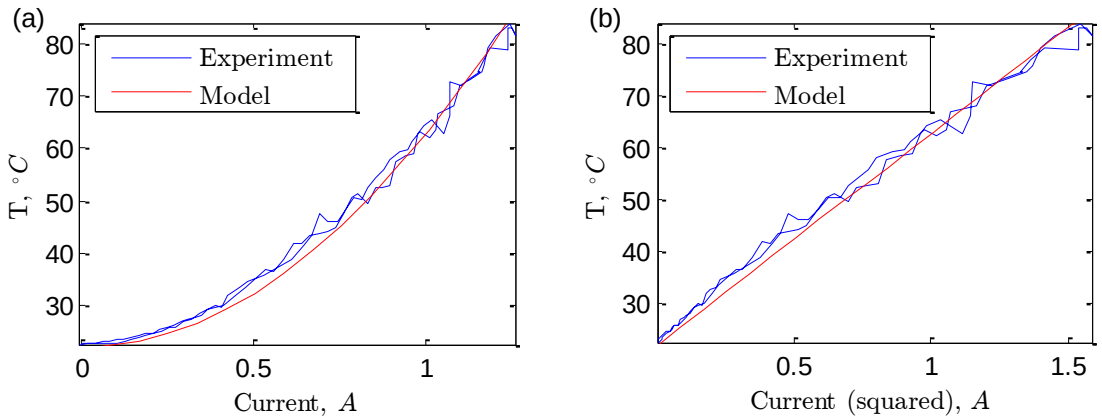

Figure 4.12. (a) Temperature versus current and (b) temperature versus current squared for voltage increasing from 0 to 2.75 V in steps of 0.05 V. The heat transfer coefficient for model is $625\ \mathrm{W/m^2 \cdot K}$.

4.6.4. Specific Heat, c_p

An attempted experimental identification for the specific heat of the Nitinol wire was completed as outlined in section 4.4.3. To note, there are two limitations to the test bed. The first limitation is the resolution in frequency of the thermocouples. The National Instruments 9211 thermocouple input module has a update frequency of only 2 Hz. This does not give adequate resolution for measuring the transient response of the wire temperature mechanics. Secondly, the mass of the thermocouple wire is large compared to the Nitinol wire, therefore, the temperature response has significant delay resulting in a delayed measurement of the transient response. Both of these limitations are not factors during steady-state response. Due to these limitations, an alternative indicator of phase transformation was needed to appropriately calculate the specific heat capacity of the Nitinol wire. This was achieved by measuring the difference in time between a voltage step input and mechanical displacement in the wire. Two methods were used to calculate the specific heat of the sample, integral and derivative methods.

An experiment is designed to measure the specific heat capacity of the Nitinol wire. Based on previous experimental results it was determined that at 1.2 V, phase transformation was the beginning of mechanical response for the austenite phase. Prior to testing, the nitinol wire was heated to the austenite final temperature and allowed to cool to ambient. After ambient temperature was achieved, stress was applied to the wire to return it completely to the detwinned martensite phase. Eleven experiments were conducted to calculate the specific heat.

Each test started at a voltage from 0 to 1 V in steps of 0.1 V and allowed steady state to occur. After 20 seconds, a step voltage of 1.2 V was applied to the wire and the transient response is recorded. In between each test, the wire is re-heated to austenite finish temperature, allowed to cool, and returned to the martensite detwinned phase.

The reason for the increasing steady state voltage inputs before application of 1.2 V is to improve the accuracy of the derivative calculation. As the difference in voltage changes, the difference in temperature changes as well. At an infinitely small change in temperature with infinitely accurate measurement resolution of temperature and austenite start time, the change at the step input should approach the true value of the specific heat as the derivative is an instantaneous slope of temperature over time. Therefore, the derivative calculation would become more and more accurate at small step inputs. Contrarily, the integral method should become less and less accurate as step inputs are decreased due to measurement error. Similarly, given any input and output, if infinitely accurate measurements are hypothesized, the integral method would be equally accurate throughout the step inputs.

To measure the difference in time between the step input and the mechanical response the transient response graph was evaluated over time. As seen in Figure 4.13 (a) the test begins with an initial current applied to the wire. At approximately 21 seconds, a step input of 0.48 A was applied to the wire. This change in current is the trigger to the start of the difference in time calculation. This trigger is indicated by the red marker in Figure 4.13 (b). A linear slope is calculated from the displacement plot, indicated by the red line, to project the time of the phase change onto the black displacement average line. The projected phase change time is indicated by the green marker. This analysis was performed on all tests in the experimental run.

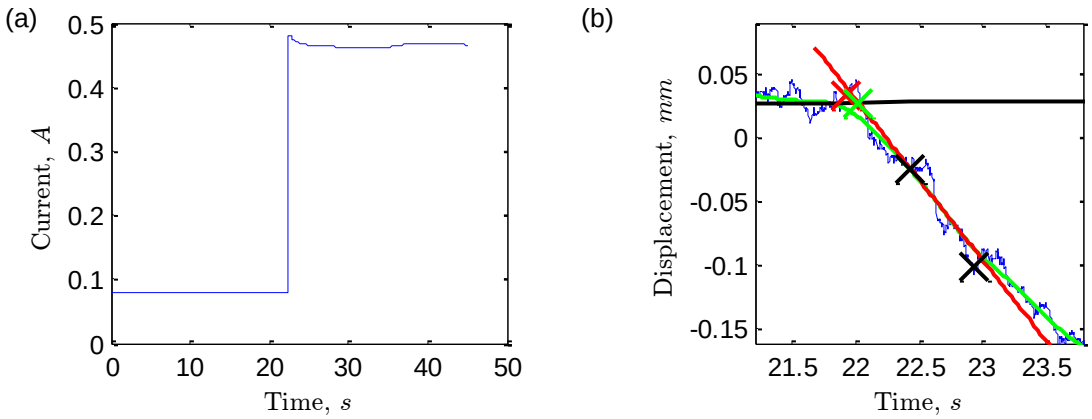

Figure 4.13. Sample plot of (a) current step input and (b) wire displacement for specific heat capacity testing.

Simultaneously the steady state temperature is calculated prior to the step input through post-processing in MATLAB. All of these values are used in calculations for the value of specific heat. A summary of test results can be seen in Table 4.3 and a graphical representation in Figure 4.14.

Table 4.3. Test results for calculation of specific heat. All tests step from V_0 to 1.2 V.

Test	V_0 (V)	ΔV (V)	T_i (°C)	ΔT (°C)	Δt (s)	$c_p \left(\frac{\mathrm{J}}{\mathrm{kg \cdot K}}\right)$ Integral Method	$c_p \left(\frac{\mathrm{J}}{\mathrm{kg \cdot K}}\right)$ Derivate Method
1	0	1.2	22.85	3.15	0.032	93.2	87.2
2	0.1	1.1	23.19	2.81	0.036	115	98.4
3	0.2	1.0	23.40	2.60	0.093	317	262
4	0.3	0.9	23.04	2.96	0.083	256	227
5	0.4	0.8	23.69	2.31	0.048	181	146
6	0.5	0.7	24.47	1.53	0.257	1390	1260
7	0.6	0.6	24.26	1.74	0.032	155	133
8*	0.7	0.5	25.82	0.176*	0.106*	4460*	7600*
9*	0.8	0.4	27.47	-1.47*	0.102*	-447*	-1840*
10*	0.9	0.3	28.40	-2.41*	-0.182*	442*	2870*
11*	1	0.2	28.54	-2.54*	-0.714*	1610*	11200*

*Large uncertainty in measurement leads to non-physical results.

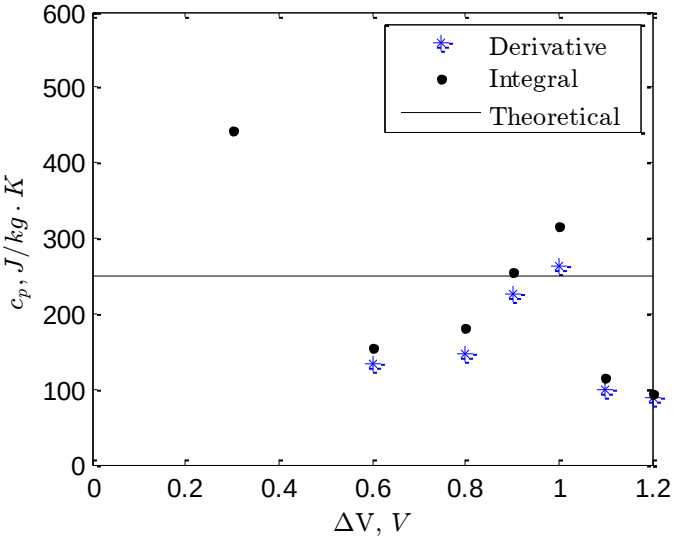

Figure 4.14. Integral and derivative method calculation for specific heat as voltage difference from experimentally determined voltage for austenite start temperature increases. Theoretical specific heat for Nitinol is plotted at a constant 250 J/kg · K [26].

It is seen that the derivative and integral methods track closely at large voltage step inputs and are indeterminable at small step inputs. This is due to the ability of the post-processing algorithm to approximate the change in mechanical response. At smaller voltage differences, and thus, temperature differences the mechanical response is not as pronounced leading to uncertainty. This can be seen in tests 10 and 11 with negative temporal difference values. Another difficulty in properly calculating the temperature change is as the voltage increases, it approaches the austenite start temperature (26 °C). For tests 9-11, all start temperatures are above the austenite start temperature. Therefore, test 8 is the last test that the transient response begins below the austenite start temperature. The variation in the specific heat value does not allow an accurate determination of the specific heat. The tests for which measurements are valid, test 1-5, result in an average specific heat of 178 J/kg · K. Due to the measurement uncertainty and the experimental results at high voltage differences, the literature [26] value of 250 J/kg · K will be used for the model parameter throughout the thesis.

4.6.5. Latent Heat of Transformation, Δh

To determine the value for the latent heat of transformation, Δh, an experiment is conducted to measure the time between full transformation from austenite start temperature to austenite final temperature. The experiment starts at 0 V and the data acquisition system records the steady state response of the unexcited wire. After recording the steady state response, a step voltage of 1.75 V is sent to the system. The displacement, temperature, and current are measured simultaneously for the remainder of the test. The 1.75 V value is equal to the step input required for the wire to meet austenite final temperature. This allows for the previous derivation of the latent heat of transformation to be used to calculate the correct value.

As can be seen in the displacement versus time plot in Figure 4.15 the two changes in length of the wire, to some degree, are subjectively placed. The austenite start temperature is less influenced by subjectivity as the start of contraction is sharp and distinct.

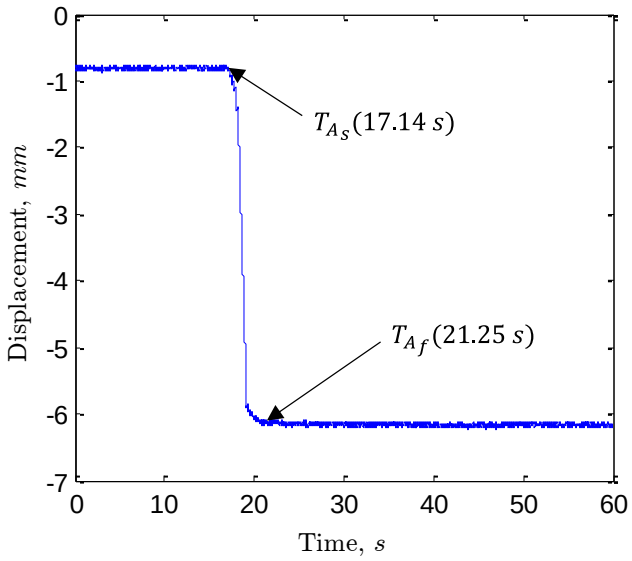

Figure 4.15. Displacement versus time for a 1.75 V step input on the shape memory alloy wire.

As can be seen from the temperature versus time graph for the experiment in Figure 4.16 the austenite finish temperature is not reached until nearly 50 seconds into the experiment. This is not possible due to the contraction of the wire being complete at 21 seconds. This temperature

response delay is due to the size of the thermocouple wire compared to the size of the nitinol wire. The current versus time verifies the current flow in the wire is 0.9 A.

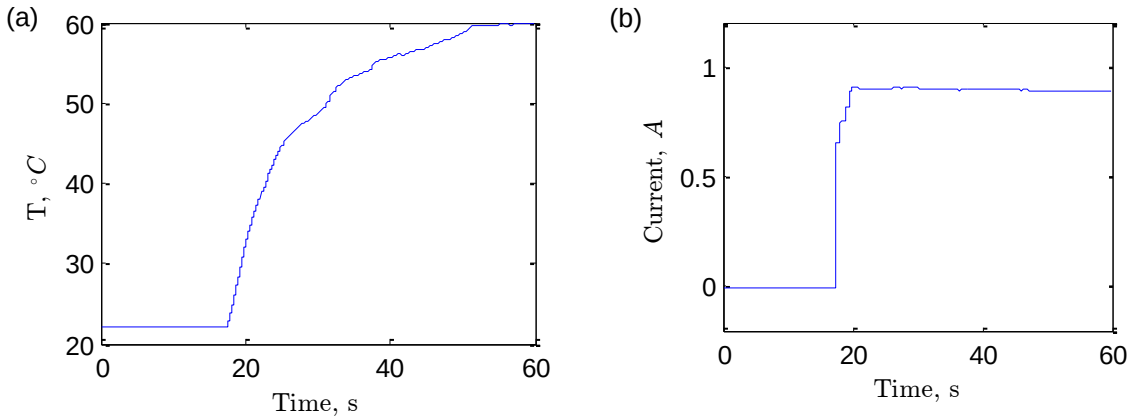

Figure 4.16. (a) Temperature versus time and (b) current versus time for a 1.75 V step input on the shape memory alloy wire.

Using the values for current, austenite start, and finish temperature combined with the mechanical indicators for actuation time the calculation for latent heat of transformation can be made from Equation (4.18) as

$$\Delta h = 45800 \text{ J}. \tag{4.27}$$

A literature review finds the latent heat of transformation to be approximately 30000 J [26]. The derived value is approximately 50% more than the nominal value. There could be several factors influencing the calculation found. The first possible factor is the mechanical inertia of the system. The lever and fulcrum assembly, combined with the springs, have an angular inertial value that could delay the response of the system. Additional stresses on the wire change the austenite final temperature and delay the time required to reach the final temperature. Another factor is the inability to objectively define the austenite final temperature through mechanical contraction. Though this is a possibility, based on this analysis, complete contraction needed to occur a full second earlier, at 19 seconds, for the calculation to produce the nominal value. The final factor is the dominant behavior of convection at austenite final temperature. Combined with the other factors previously described, identification of the

austenite final time at this temperature range can vary the calculated latent heat value dramatically. With these effects in mind, the nominal value will be used for the heat transfer model for the remainder of the thesis.

The updated coefficients based on both experimental and nominal values are shown in **Error! Reference source not found.**.

Table 4.4. Final heat transfer model parameters.

Parameter	Measured Value	Nominal Value
R	2.3* Ω	2.02 Ω [27]
h	625* $\mathrm{W/m^2 \cdot K}$	80-120 $\mathrm{W/m^2 \cdot K}$ [26, 28]
c_p	178 $\mathrm{J/kg \cdot K}$	250* $\mathrm{J/kg \cdot K}$ [26]
Δh	45800 J	30000* J [26]

*Indicates model parameter used for this thesis.

4.7. Conclusions

A heat transfer model for a shape memory alloy wire is proposed containing internal heat of the wire, phase transformation energy, convection, and resistive heating. This model is examined for dominant effects throughout the shape memory effect of the SMA wire. It is found that near ambient temperatures that the internal energy of the wire is the dominant sink of energy in the system. At large temperature differences, convection becomes a near dominant term for all energy, leading to most source energy being converted directly into energy loss. Using the heat transfer model and a wire test bed, unknown coefficients are solved for based on electrical properties, steady-state response, and mechanical responses of the test bed. The resistance in the wire was found to be 2.3 Ω, while the heat transfer coefficient, h, is determined to be 625 $\mathrm{W/m^2 \cdot K}$; both values are found with relative certainty. The specific heat capacity, c_p, experiment showed large variation in the calculation ranging from half the proposed value to magnitudes higher dependent on the voltage step identified by the experiment. Due to uncertainty in the measurement, the literature value of 250 $\mathrm{J/kg \cdot K}$ is accepted as the correct value. Likewise, experimental analysis for the latent heat of transformation found inertial

effects, convection dominance, and measurement uncertainty as likely sources for error in deviation from the literature value of 30000 J. Due to these sources of uncertainty, the literature value for latent heat is accepted as well.

CHAPTER 5

DEMONSTRATION OF AN ANTAGONISTIC SMA MECHANISM

5.1. Introduction

In chapter two an antagonistic kinematic mechanism was proposed to replicate the motion of the human arm with rigid body assumptions. This two-way actuation was reduced to one-way actuation and a parametric analysis was completed on the mechanism. It is now the intent of this chapter to return to the antagonistic mechanism and demonstrate a proof of concept for antagonistic actuation.

An antagonistic mechanism is designed for the kinematic test bed based on the antagonistic kinematic mechanism presented in chapter 2. This mechanism is presented as a rigid body crank-slider mechanism; however, for the kinematic test bed the mechanism in Figure 5.1 is proposed. This modified mechanism replaces the rigid body assumptions for each slider arm as contractible spring elements.

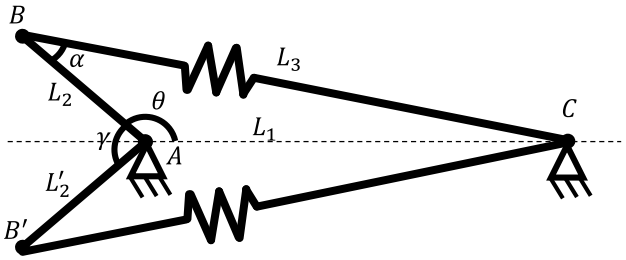

Figure 5.1. Modified kinematic mechanism with double spring elements in place for the SMA wires.

5.2. Prototype Design

A proof of concept is designed based on the antagonistic mechanism presented in chapter 2 and heat transfer model from chapter 4. There are several items to note from the prototype antagonistic mechanism shown in Figure 5.2 (a). The device is designed to host two

antagonistic wires, requiring two separately isolated terminal blocks on each component of the device; the electrical contacts are called out in Figure 5.2 (a). For ease of instruction the discussion will begin at the positive electrical contacts. At each of the electrical contacts is a two washer stack, where the SMA wire is placed between the pair of washers, and capped with a socket head cap screw. The electrical lead is placed between the top washer and the socket head cap screw. This stack is compressed together securing the SMA wire on each end. When the washer compresses the SMA wire a stress concentration occurs at the pinch point. To relocate the stress concentration, the wire is looped around a ceramic rod located at point B. The position of the washer stack where the SMA wire is secured is tangent to the outer diameter of the rod. This minimizes stress at the pinch point. The schematic of the wire clamping mechanism is shown in Figure 5.2 (b).

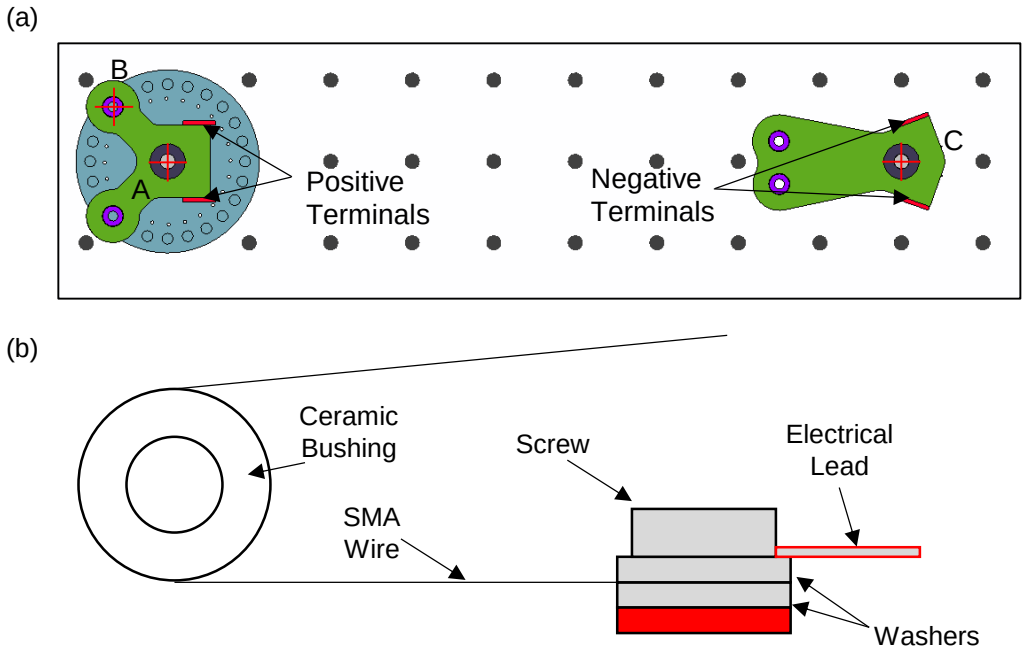

Figure 5.2. (a) Model of antagonistic shape memory alloy actuated mechanism. (b) Illustration of wire clamping mechanism.

The SMA wire continues from point B leading to point C where it is fastened by a second washer and screw stack. This mechanism component also contains a ceramic rod used

for stress relief purposes and is tangent to the terminal at point C. The mechanism geometries are symmetric with respect to the A-C axis and a replicate SMA wire is placed on the mirroring side. At points A and C a shaft is fastened to the kinematic test bed allowing the mechanism to rotate with negligible friction by way of ball bearings. The mechanism is held in place vertically by bushings and shaft collars. An image of the device captured by the Point Grey camera is seen in Figure 5.3.

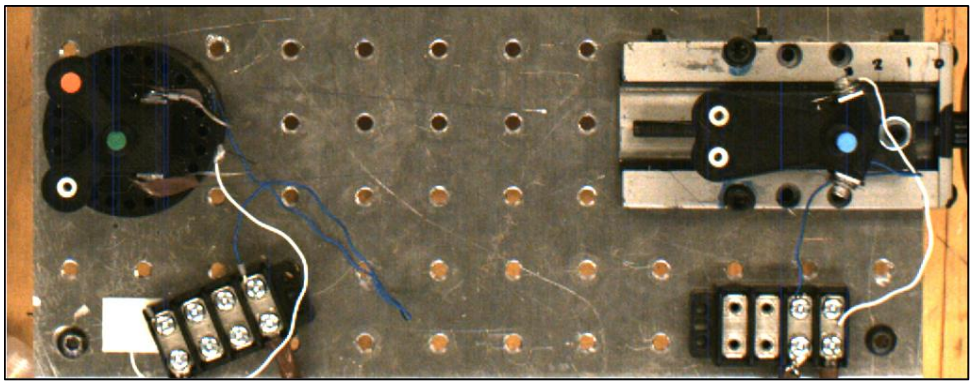

Figure 5.3. Image of the prototype antagonistic mechanism.

The shape memory alloy wires are fastened by hand to the mechanism. This process leaves little to no tension in the wire, preventing the full actuation strain from being applied to the mechanism. For this reason, the point C shaft is secured to a slide table. After fastening the wires to each end of the mechanism, the slide table is extended to remove any slack that may remain.

5.3. Experiments

5.3.1. Setup

The experiment is performed on the kinematic test bed seen in Figure 5.4. Two SMA wires are fastened at the positive nodes of the mechanism and looped around the ceramic stress-relief bushings to the negative node. A voltage control signal is sent from the NI data acquisition device (NI cDAQ 9178) to one of two KEPCO BOP 36-6D bi-operational amplifiers.

Each amplifier is isolated and is used to actuate the agonistic or antagonistic shape memory alloy wire. The current and voltage are monitored by the amplifier.

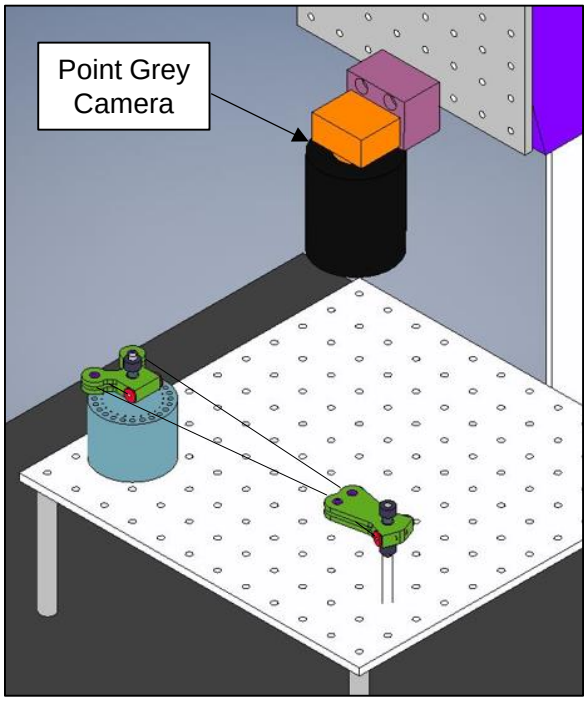

Figure 5.4. Isometric view of antagonistic mechanism on kinematic test bed.

The Point Grey camera is placed overhead of the mechanism and records the motion by way of visual markers. The device is a one degree of freedom device, therefore, only one angle needs to be known to define its position. The position of points A, B, and C are identified by green, red, and blue indicators and are tracked by the point grey camera through OpenCV software. These three positions are used to calculate the rocking angle of the mechanism. An information flow diagram of the kinematic test bed can is shown in Figure 5.5.

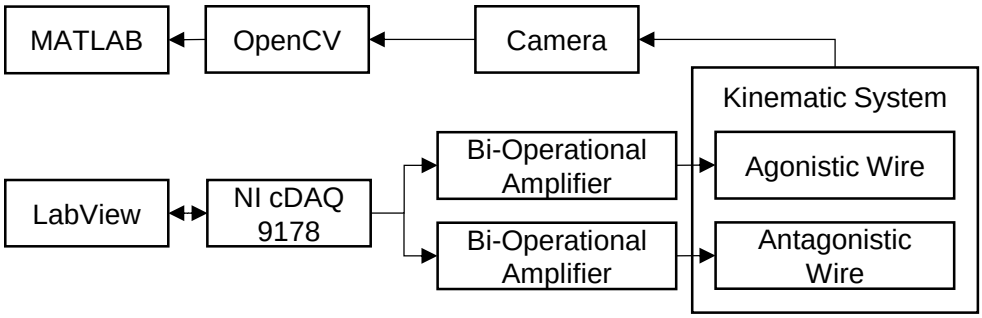

Figure 5.5. Information flow of kinematic test bed.

5.3.2. Procedure

There are two results of interest in this proof of concept demonstration. The first being, a functioning demonstration of the antagonistic mechanism. The second being, an analysis on the effects of wire pre-stress on rocking angle. The SMA wire used in this testing is a 230 μm (0.009″) diameter nickel-titanium wire manufactured by Dynalloy, Inc.

The test procedure begins with fastening of the SMA wires in a detwinned martensite state. Once fastened, the slide table is extended until limited tension is present in both wires simultaneously. If one wire experiences tension before the other, the wire is disconnected, repositioned, and re-fastened until the desired state is met. Next, the detwinned strain position is measured with a micrometer and recorded at the zero position. The slide table is then retracted completely where the wires are completely slack. The wires are then subjected to 0.8 A of current, changing the crystallographic structure to pure austenite. The voltage is removed after five seconds and allowed to cool. The slide table position is returned to the detwinned martensite position. This heating and cooling cycle is necessary to clear out any previous hysteresis loops trained in the wire.

This experiment tests for effects of wire pre-stress on rocking angle. For each step in the experiment the wire pre-stress is increased by extending the slide table in increments of 2.5 mm. The memory wiping cycle is performed between each incremental step in the experiment. Once in the pre-stress initial condition, the 0.8 A current is driven through the agonistic wire and allowed to heat to contraction. One contraction is complete, the current is removed and applied to the opposing wire. The pre-stress positions are 0 mm to 12.5 mm in 2.5 mm step increments.

5.3.3. Results

The mechanism actuation angular displacement in each direction is shown in Figure 5.6. The mechanism begins at near 131 degrees and actuates completely in the agonistic direction then fully in the antagonistic direction. Figure 5.6 shows hints of an actuation angle decrease as pre-stress in the wire increases.

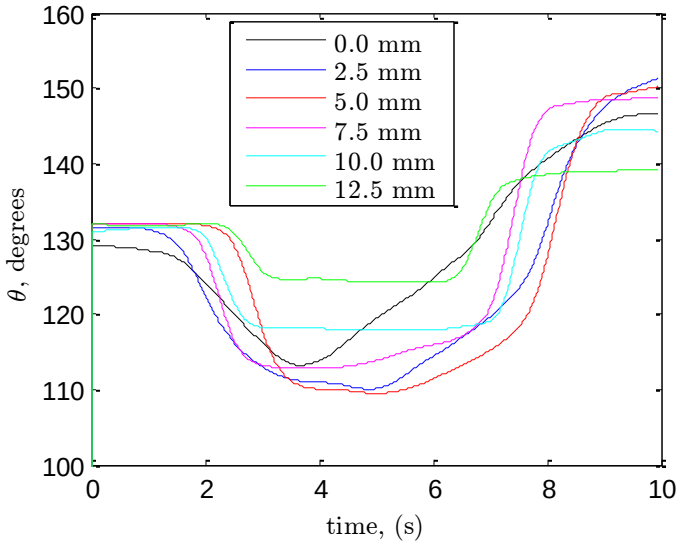

Figure 5.6. Measured angle of rocker over time as a function of displacement of the slider.

Calculating the total difference in rocking angle as pre-stress is increased in the wire shows an initial increase in rocking angle followed by a declination until near blocking force is reached. The maximum rocking angle by initial strain is seen in Figure 5.7. The initial increase in actuation angle can be attributed to the setup of the wire. If the wire is not appropriately pre-tensioned some of the contraction will go into removing the slack in the wire and thus cannot be used for actuation.

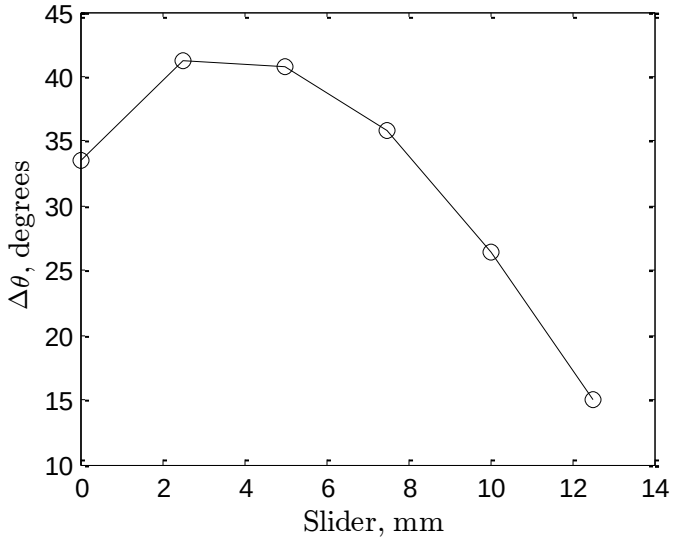

Figure 5.7. Measured maximum rocking angle versus initial displacement of the slider.

This hypothesis is confirmed by comparing two sets of data. First, by examining Figure 5.6 for the lowest pre-stress, or the 0 mm data set, it shows an initial position difference compared to other test runs. This suggests that the slack caused the mechanism to not be completely constrained on initial conditions. This is further confirmed by examining the actuation by wire; seen in Figure 5.8. The agonistic wire has a smaller rocking angle on the initial actuation, with it being much larger than the agonistic wire on all others. This shows that the mechanism had a bias in the closed position before the first actuation; causing the measurement system to correctly measure a smaller rocking angle.

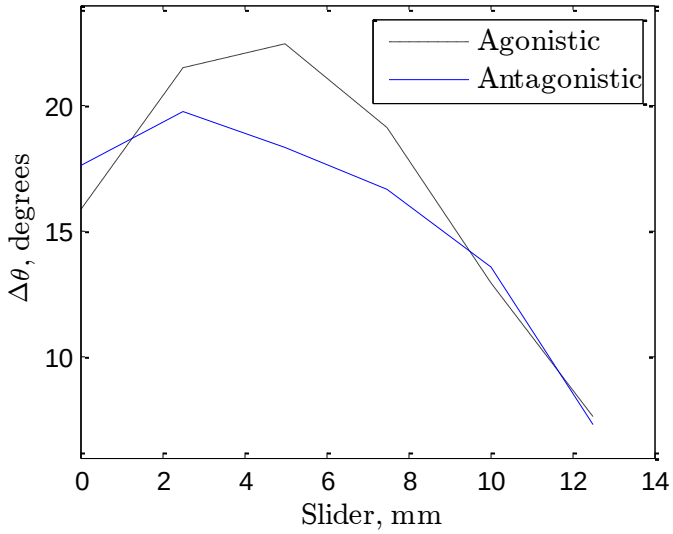

Figure 5.8. Comparison of rocking angle by wire pair.

5.4. Conclusions

It has been shown, in this proof of concept that an antagonistic mechanism can be designed to actuate in both directions by the use of Joule heating in shape memory alloy wires. Pre-stressing the antagonistic pair has a significant effect on rocking angle at large stresses. This suggests that rocking angle can be controlled by Joule heating and stress management in each wire. It was seen that pre-stressing the wires slightly improves actuation response, as any slack in the wire can bias and reduce actuation angle. Also, it shows in the initial pre-stress region there is little decrease in rocking angle as a function of the pre-stress.

CHAPTER 6

CONCLUSIONS AND FUTURE WORK

This research presents the proposal and analysis of a shape memory alloy actuated kinematic mechanism as a prosthetic device. An antagonistic mechanism is proposed and reduced to one-way actuation for analysis purposes. A parametric analysis is performed on the shape memory alloy actuated mechanism and compared to one actuated by human muscle.

A dynamics model is developed for the mechanism and phase portrait analysis is performed to examine the mechanism at different operating points. It is found that the mechanism has two operating points at which equilibria exist; a stable and an unstable equilibria. This dynamics model is to be used in a future thermo-mechanically coupled model.

A heat transfer model is then proposed and energy analysis at different shape memory effect phases are performed. After, parameters are analytically derived for system identification purposes. These parameters are experimentally tested and identified based on analytical calculations.

Finally, a proof of concept is designed based on the preceding analysis. The mechanism is tested for functionality and pre-stress conditions.

6.1. Summary

Chapter 2 introduces an antagonistic kinematic mechanism to replicate the motion of a human arm. This antagonistic mechanism is reduced to a single actuation mechanism and parametric analysis is performed by adjusting the starting angle and the frame length while calculating torque, rocking angle, and work. The results of the parametric analysis show peak torque across the band where blocking force and transmission angle are maximized simultaneously. Maximum work and maximum rocking angle occur at large frame lengths and large rocking angles. Nonlinear actuator results are compared with linear actuator results and trends in the data are equivalent in each case; however, by assuming a linear actuator, work and

torque are under-represented as frame length increases. A literature review is performed on the human arm musculoskeletal link-lengths and muscle properties. These results are substituted into the kinematic mechanism and a parametric analysis is performed on the human muscle actuated mechanism. The results show that human skeletal link-lengths and starting angle coincide with areas of maximum work and maximum rocking angle.

Chapter 3 examines the structurally dynamic properties of the kinematic mechanism. The force-balance and energy-balance derivations are completed to produce an identical second order differential equation. A phase portrait analysis is performed on the differential equation adjusting parameter values. Two unique equilibrium points for the mechanism are determined at starting angles of $\theta = 0$ rad and $\theta = \pi$ rad. The differential equation is linearized and the type of the equilibrium points are evaluated by examining eigenvalues of the state equations for the differential equation. A stiffness ratio is proposed and a relation between equilibrium type and stiffness ratio is shown. At stiffness ratios greater than one the equilibrium shifts from stable to unstable. It is noted that with the shift in stability a bifurcation behavior is exhibited. Lastly, a damping term is introduced to the differential equation and the response of the system is observed. It is seen during this analysis that the response of the system is drawn into potential energy wells located at the center node for the stable equilibrium point and at opposing potential energy wells on each side of the bifurcation. The energy of the response as it oscillates around the saddle equilibrium point determines the potential energy well the response will "fall" into.

Chapter 4 proposes a heat transfer model for the joule heating of a shape memory alloy wire at a zero stress condition. The differential equation is composed of four terms: energy generation, internal energy storage, phase transformation, and energy loss. Energy contributions of these four components are analyzed as a function of phase and time. At temperatures close to ambient temperature the internal energy and phase transformation dominate the energy contribution to the system. At elevated temperatures potential energy loss due to convection dominates. The parameters of the differential equation are determined analytically and experiments are proposed to verify parameter values. It is shown that resistance and convection coefficient match with certainty to industry and literature results.

Experimental latent energy of transformation and specific heat are close to literature results; however, due to the limitations of the measurement system, results show large variation and literature results are used for the heat transfer model.

Chapter 5 proposes a design for a proof of concept for antagonistic actuation. The proof of concept shows successful antagonistic actuation. Rocking angle is measured as pre-stress is increased in the wire.

6.2. Related Publications

In the development of this thesis, a related paper was presented at the 2016 SPIE Smart Structures Bioinspiration, Biomimetics, and Bioreplication conference. Another paper is accepted and will be presented at the ASME 2016 SMASIS Conference on Smart Materials, Adaptive Structures and Intelligent Systems. These works are referenced below.

1. Wright, Cody, and Onur Bilgen. "Parametric analysis of a shape memory alloy actuated arm." *SPIE Smart Structures and Materials+ Nondestructive Evaluation and Health Monitoring*. International Society for Optics and Photonics, 2016.
2. Wright, Cody, and Onur Bilgen. "Analysis and Design of a Shape Memory Alloy Actuated Arm to Replicate Human Biomechanics", ASME Conference on Smart Materials, Adaptive Structures and Intelligent Systems, 2016

6.3. Future Work

Future research will focus on coupling the heat transfer equation with the dynamics equation and developing an accurate model to perform parametric analysis for heat transfer and dynamic performance metrics.

REFERENCES

[1] I. Mihálcz, "Fundamental characteristics and design method for nickel-titanium shape memory alloy," *Periodica Polytechnica. Engineering. Mechanical Engineering,* vol. 45, p. 75, 2001.

[2] A. Ölander, "An electrochemical investigation of solid cadmium-gold alloys," *Journal of the American Chemical Society,* vol. 54, pp. 3819-3833, 1932.

[3] L. Chang and T. Read, "Plastic deformation and diffusionless phase changes in metals-the gold-cadmium beta-phase," *Transactions of the American Institute of Mining and Metallurgical Engineers,* vol. 191, pp. 47-52, 1951.

[4] W. J. Buehler and F. E. Wang, "A summary of recent research on the Nitinol alloys and their potential application in ocean engineering," *Ocean Engineering,* vol. 1, pp. 105IN7109-108IN10120, 1968.

[5] Y. H. Teh, *Fast, accurate force and position control of shape memory alloy actuators*: Australian National University, 2008.

[6] J. N. Kudva, C. A. Martin, L. B. Scherer, A. P. Jardine, A. R. McGowan, R. C. Lake, *et al.*, "Overview of the DARPA/AFRL/NASA smart wing program," in *Proc of 6th Ann Int Symp Smart Struct Mat, Newport Beach, USA, 1*, 1999.

[7] D. Reynaerts, J. Peirs, and H. Van Brussel, "Shape memory micro-actuation for a gastro-intestinal intervention system," *Sensors and Actuators A: physical,* vol. 77, pp. 157-166, 1999.

[8] K. Ho, J. Gill, G. Carman, and P. Jardine, "Fabrication and characterization of thin film NiTi for use as a microbubble for active flow control," in *Proc of 6th Ann Int Symp Smart Struct Mat*, 1999, pp. 1-5.

[9] E. A. Biddiss and T. T. Chau, "Upper limb prosthesis use and abandonment: a survey of the last 25 years," *Prosthetics and orthotics international,* vol. 31, pp. 236-257, 2007.

[10] K. Kuribayashi, "A new actuator of a joint mechanism using TiNi alloy wire," *the International journal of Robotics Research,* vol. 4, pp. 47-58, 1986.

[11] M. Bergamasco, F. Salsedo, and P. Dario, "Shape memory alloy micromotors for direct-drive actuation of dexterous artificial hands," *Sensors and Actuators,* vol. 17, pp. 115-119, 1989.

[12] M. A. Gharaybeh and G. C. Burdea, "Investigation of a shape memory alloy actuator for dextrous force-feedback masters," *Advanced robotics,* vol. 9, pp. 317-329, 1994.

[13] A. Price, A. Jnifene, and H. Naguib, "Design and control of a shape memory alloy based dexterous robot hand," *Smart Materials and Structures,* vol. 16, p. 1401, 2007.

[14] V. Bundhoo and E. J. Park, "Design of an artificial muscle actuated finger towards biomimetic prosthetic hands," in *Advanced Robotics, 2005. ICAR'05. Proceedings., 12th International Conference on*, 2005, pp. 368-375.

[15] C. Pfeiffer, K. DeLaurentis, and C. Mavroidis, "Shape memory alloy actuated robot prostheses: initial experiments," in *Robotics and Automation, 1999. Proceedings. 1999 IEEE International Conference on*, 1999, pp. 2385-2391.

[16] K. J. D. Laurentis and C. Mavroidis, "Mechanical design of a shape memory alloy actuated prosthetic hand," *Technology and Health Care,* vol. 10, pp. 91-106, 2002.

[17] L. C. Brinson, "One-dimensional constitutive behavior of shape memory alloys: thermomechanical derivation with non-constant material functions and redefined martensite internal variable," *Journal of intelligent material systems and structures,* vol. 4, pp. 229-242, 1993.

[18] Y.-W. Chang, F.-C. Su, H.-W. Wu, and K.-N. An, "Optimum length of muscle contraction," *Clinical Biomechanics,* vol. 14, pp. 537-542, 1999.

[19] W. M. Murray, T. S. Buchanan, and S. L. Delp, "The isometric functional capacity of muscles that cross the elbow," *Journal of biomechanics,* vol. 33, pp. 943-952, 2000.

[20] T. J. Kovack, J. D. Idoine, and P. B. Jacob, "Proximal Biceps Tenodesis An Anatomic Study and Comparison of the Accuracy of Arthroscopic and Open Techniques Using Interference Screws," *Orthopaedic journal of sports medicine,* vol. 2, p. 2325967114522198, 2014.

[21] B. A. Garner and M. G. Pandy, "Estimation of musculotendon properties in the human upper limb," *Annals of biomedical engineering,* vol. 31, pp. 207-220, 2003.

[22] C. Walton, Z. Li, A. Pennings, A. Agur, and A. Elmaraghy, "A 3-Dimensional Anatomic Study of the Distal Biceps Tendon Implications for Surgical Repair and Reconstruction," *Orthopaedic Journal of Sports Medicine,* vol. 3, p. 2325967115585113, 2015.

[23] A. D. Mazzocca, M. Cohen, E. Berkson, G. Nicholson, B. C. Carofino, R. Arciero, *et al.*, "The anatomy of the bicipital tuberosity and distal biceps tendon," *Journal of Shoulder and Elbow Surgery,* vol. 16, pp. 122-127, 2007.

[24] M. R. Dayal, M. Steyn, and K. L. Kuykendall, "Stature estimation from bones of South African whites," *South African Journal of Science,* vol. 104, pp. 124-128, 2008.

[25] E. Van Zuylen, A. Van Velzen, and J. D. van der Gon, "A biomechanical model for flexion torques of human arm muscles as a function of elbow angle," *Journal of biomechanics,* vol. 21, pp. 183-190, 1988.

[26] A. R. Shahin, P. H. Meckl, J. D. Jones, and M. A. Thrasher, "Enhanced cooling of shape memory alloy wires using semiconductor" heat pump" modules," *Journal of Intelligent Material Systems and Structures,* vol. 5, pp. 95-104, 1994.

[27] Dynalloy, "Technical Characteristics of FLEXINOL Actuator Wires," ed. Irvine, CA: Dynalloy, Inc., 2016.

[28] A. Lara-Quintanilla and H. E. Bersee, "A study on the contraction and cooling times of actively cooled shape memory alloy wires," *Journal of Intelligent Material Systems and Structures*, p. 1045389X15595124, 2015.

VITA

Cody Alexander Wright

Department of Mechanical & Aerospace Engineering, 238 Kaufman Hall, Norfolk, VA 23529
Phone: 757-679-4404 Email: cwrig018@odu.edu

Education:

Masters of Science December 2016
Old Dominion University, Norfolk, VA
Major: Mechanical Engineering *GPA: 3.85*
Thesis Title: Thermo-mechanical System Identification of a Shape Memory Alloy Actuated Mechanism

Bachelor of Science May 2011
Old Dominion University, Norfolk, VA
Major: Mechanical Engineering *GPA: 3.86*
Minor: Engineering Management

Professional Experience:

Continental Automotive Systems August 2011 – August 2016
Manufacturing Engineer

- Process owner for a dozen automated production lines responsible for generating over 6,000,000 units per year.
- Improve production processes to reduce scrap and increase productivity using six sigma and lean manufacturing principles.
- Redesigning and implementation of tooling to improve product integrity, product quality, process capability, and OEE.
- Collaborate with manufacturing cell operators to implement procedures and guidelines.
- Work with product and quality engineers to standardize work instruction, create control plans, and PFMEAs for newly introduced production lines.
- Carry out root-cause analysis on non-conforming production parts implementing corrective action to ensure product quality.
- Interact with customers and vendors to resolve quality concerns.

Jefferson Lab - Applied Research Center May 2011 – January 2012
Research Assistant

- Performed and analyzed hardness and modulus testing on Escherichia coli; ex vivo and in vivo.
- Developed processes and tooling for bacteria surface detection in vivo.

Selected Publications:

Wright, Cody, and Onur Bilgen. "Parametric analysis of a shape memory alloy actuated arm." SPIE Smart Structures and Materials+ Nondestructive Evaluation and Health Monitoring. International Society for Optics and Photonics, 2016.